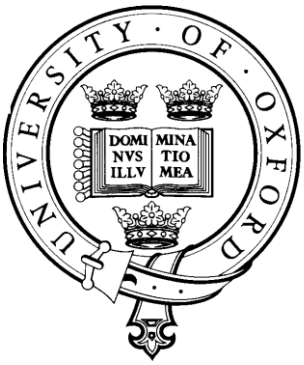
The Mechanical Response of Low to High Density Rohacell Foams

Sara Poxon

(née Sara Arezoo)

Department of Engineering Science

University of Oxford



Michaelmas Term 2012

The Mechanical Response of Low to High Density Rohacell Foams

Sara Poxon, St Catherine's College, University of Oxford
For the degree of D.Phil. in Engineering Science, Michaelmas Term 2012

Abstract

The main aim of this thesis is to generate a deeper understanding of the mechanical behaviour of cellular materials, specifically for their use in aerospace applications. A closed-cell polymer foam material (Rohacell) of various foam densities was chosen for this investigation, and a comprehensive experimental study was conducted which generated significant findings that hitherto have not been reported in the literature.

The research presented in this study revealed the following:

The quasistatic response of Rohacell foam displays a compression/tension asymmetry in moduli and strength. In-situ experiments revealed that different macroscopic collapse mechanisms at different foam densities drove this behaviour.

Improved experimental methods were developed to characterise the material response at various loading rates. Under compressive loading, as the relative density and loading rate increased, a transition in material behaviour from a ductile to brittle response at very high rates (~$5x10^3$ s^{-1}) was found, and tests conducted at different temperatures were used to validate and provide a better understanding of the causes for the observed rate dependency.

The compression and tension properties of pre-crushed Rohacell foam loaded in different directions were measured, and with the use of three-point-bend tests it was shown that when the foams' tension/compression asymmetry, or the changes in stiffness and strength due to pre-crushing (i.e. strain-induced anisotropy), are neglected, this leads to incorrect predictions of the foams' structural response. Finally, a review of some existing Finite Element foam material models was conducted, and their ability to predict the foam response under complex loading was identified.

The new data and understanding generated from this thesis will allow engineers and researchers, who are developing constitutive models for predicting the response of foam materials, specifically in aerospace applications, to account for more aspects of the mechanical behaviours in their Finite Element models.

Acknowledgements

My deepest thanks go to my three supervisors who contributed towards the completion of this thesis, each in their own individual way. Dr Vito Tagarielli, whose technical expertise, wisdom and encouragement, combined with his humour, bluntness and constant inspiration to write journal papers, helped me to work harder, faster and better. Dr Clive Siviour, whose valuable advice during my research, and especially in the final stages of write-up, is much appreciated. Dr Nik Petrinic for agreeing to take me on as a part-time student and for his help and encouragement throughout the project.

Rolls-Royce Plc has funded the research for this project, and I would especially like to thank Dr Julian Reed and Dr Andy Moore for allowing me to embark on this journey. The task of pursuing a part-time DPhil course whilst fulfilling my industrial obligations in the limited time provided, has been challenging, fraught with difficulties, yet fully rewarding, and I would like to thank all parties who have helped me throughout this journey.

During my time at Oxford, the many members of the Solid Mechanics group never failed to provide help and friendship when required. In particular, I would like to thank Olga Barrera for her friendship and constant encouragement towards maintaining a balance between work and exercise, by persuading me to join her in her regular “body attack” gym classes. I would also like to thank Matt Arthington, Michael Okereka, Petros Siegkas, Jon Gregory, Antonio Pallegrino, Jens Wiegand and Robert Gerlach for their friendship and banter during my time at Oxford.

My special thanks go to the workshop team, in particular Richard Duffin, Stuart Carter and Dick Froud, who have always accommodated my unexpected drop-ins and my pleas to machine more specimens at short notice. They were always supportive, and I would not have completed all my experiments on time if it were not for their help. Special thanks also go to Dr Kalin Dragnevski and Dr Igor Dyson, whose advice and training on the use of their lab equipment was greatly appreciated.

Finally, and most importantly I would like to thank my family. My husband, Scott, who has supported me in every decision I have made, and has encouraged me to follow my dreams and aspirations. My mother who throughout my life has been a constant source of strength and support, and who taught me that I can achieve whatever I set my mind to. My father who has aspired me to pursue knowledge and have an open mind, and Ali, Leyla, Christine and David who have always wished me success.

Contents

Abstract i
Acknowledgements ii
Contents iii
List of Figures vi
List of Tables xiv
Notations xv
1. Introduction 1
1.1 Background and Motivation 1
1.2 Main Research Objectives 8
2. Literature Review 10
2.1 An Overview of Foam Materials 11
2.2 Rohacell Foam 13
2.3 Deformation Mechanisms in Foam Material 16
2.3.1 Compressive Deformation 16
2.3.2 Tensile Deformation 18
2.4 Microscopic Foam Models and Scaling Laws 20
2.5 Strain Rate Sensitivity in Polymer Foam Material 24
2.6 Temperature Effects in Polymer Foam Materials 33
2.7 Residual Properties of Pre-crushed Foam 36
2.8 Research Strategy 38
3. Experimental Study 41
3.1 Specimen Preparation and Choice of Geometry 43
3.1.1 Compression Specimens 43
3.1.2 Tensile Specimens 47
3.1.3 Shear Specimens 48
3.2 Experimental Apparatus 50
3.2.1 Quasistatic Tests 50
3.2.2 Medium Rate Experiments 52
3.2.3 High Rate Experiments 53
3.3 Strain Measurements using Photography Based Methods 59
3.4 Compression Tests at Different Temperatures 62
3.5 Environmental Scanning Electron Microscopy 64
3.5.1 In-situ Mechanical Testing 65
4. Quasistatic Response at Different Length Scales 67

4.1 Experimental Results 68
4.1.1 Foam Isotropy 68
4.1.2 Quasistatic Compression Test Results 69
4.1.3 Quasistatic Tensile Test Results 71
4.1.4 Quasistatic Shear Test Results 73
4.1.5 Indentation Experiments 76
4.2 In-situ Compression and Tension Experiments 79
4.3 Concluding Discussion 86
5. Compressive Deformation of Rohacell Foams: Effects of Strain Rate and Temperature 89
5.1 Experimental Methods 91
5.1.1 Specimen Size and Preparation 91
5.1.2 Quasistatic and Medium Rate Experiments 91
5.1.3 Split Hopkinson Pressure Bar (SHPB) Experiments 92
5.2 Experimental Results and Discussion 96
5.2.1 Strain Rate Sensitivity of the Response at Room Temperature 96
5.3 Compression Tests at Different Temperatures 104
5.3.1 Experimental Methods 104
5.3.2 Sensitivity of the Quasistatic Response to Temperature 104
5.4 Time-Temperature Superposition 111
5.4.1 Time Temperature Superposition Results 112
5.5 Foam Stiffness 114
5.6 Conclusions 116
6. Strain-Induced Anisotropy Effects 117
6.1 Experimental Investigation 119
6.1.1 Specimen Preparation 119
6.2 Experimental Results 121
6.2.1 Tensile Response, Parallel and Perpendicular to Crush 121
6.2.2 Compressive Response, Perpendicular to Crush 123
6.2.3 Normalised Specific Residual Strength and Stiffness 124
6.2.4 Discussion 127
6.3 Three-Point-Bend Experiments 130
6.3.1 Experimental Apparatus and Specimen Preparation 130
6.3.2 Three-Point-Bend Test Results 131
6.3.3 Three-Point-Bend Test Predictions 132

6.3.4 Stiffness and Strength Predictions of Pre-crushed Material ... 139
6.4 Conclusions ... 142
7. Macroscopic Numerical Modelling ... 144
7.1 Experiments ... 146
7.1.1 Indentation Experiment ... 146
7.2 Finite Element Simulations & Results ... 148
7.2.1 ABAQUS (Mat Crushable Foam) ... 148
7.2.2 LS-DYNA (Mat Crushable Foam) ... 150
7.3 Discussion ... 156
8. Conclusions, Improvements and Future Work ... 158

List of Figures

Figure 1-1: A typical Turboprop engine (Toffsworld.com, 2012) 2

Figure 1-2: GE and NASA's UnDucted Fan design in the late 1980's (www.aerospaceweb.org, 2012) 2

Figure 1-3: Composite fan case system (www.gkn.com, 2012) 4

Figure 1-4: Typical symmetric sandwich construction, as used in the open rotor concept design (Gundberg, 2012) 5

Figure 2-1: Various core materials used in sandwich constructions (Stewart, 2010) 11

Figure 2-2: Chemical formation of PMI foam (left), and the key manufacturing steps (right), courtesy of (clarasonic.com, 2010) 13

Figure 2-3: A typical compressive stress-strain curve for cellular materials, courtesy of (ERG Aerospace Corp., 2009)..... 16

Figure 2-4: A typical compressive stress-strain plot (T=23°C, $\dot{\varepsilon} = 10^{-2}\,\mathrm{s}^{-1}$) demonstrating loading and unloading curves, courtesy of (Arezoo et al., 2011). 17

Figure 2-5: A tetrakaidecahedral unit cell (left) and a microscopic image (right) of the low density Rohacell foam (51 kg m^{-3}), illustrating the cell shapes and sizes. 22

Figure 2-6: Effect of strain rate (T~23°C, $\dot{\varepsilon} = 10^{-4}\ \mathrm{to}\ 10^{3}\,\mathrm{s}^{-1}$) on plateau strength of Balsa wood and different densities of PVC foam specimens (Tagarielli et al. 2008). 26

Figure 2-7: Strain rate dependency of the peak and plateau stress (T~23°C, $\dot{\varepsilon} = 10^{-3}\ \mathrm{to}\ 10^{4}\,\mathrm{s}^{-1}$) for an epoxy syntactic foam (left) and the

resulting stress-strain curves at different loading rates (right), courtesy of (Li et al., 2009)..... 27

Figure 2-8: Stress-strain curves of an epoxy foam at various strain rates (left) and strain rate effects (T~23°C, $\dot{\varepsilon} = 0.05 \text{ to } 2700\ s^{-1}$) on the modulus of elasticity and cell-collapse stress (right), courtesy of (Song et al. 2007) 28

Figure 2-9: Effect of strain rate on elastic modulus and collapse stress of polystyrene foam (T~23°C, $\dot{\varepsilon} = 10^{-4} \text{ to } 10^{4}\ s^{-1}$), courtesy of (Song 2005) 29

Figure 2-10: Typical stress-strain curve of a polymer material showing the effect of strain rate and temperature (Meyers & Chawla, 2009)..... 33

Figure 3-1: Compression specimen 2D geometry 44

Figure 3-2: Compressive stress-strain curves of R200 (T=23°C, $\dot{\varepsilon} = 10^{-2}\ s^{-1}$), 4 mm vs. 10 mm thick specimens..... 46

Figure 3-3: Tensile specimen geometry..... 47

Figure 3-4: Shear specimen geometry..... 48

Figure 3-5: Schematic of the quasistatic compression (left) and tension (right) test set-up, with the laser extensometer recording the positions of painted stripes. 51

Figure 3-6: A simple schematic of the SHPB apparatus used in this study..... 55

Figure 3-7: SHPB for high strain rate testing 56

Figure 3-8: The use of photography-based methods to measure specimen strain in the x and y directions, respectively. 60

Figure 3-9: Schematic diagram of the ESEM column identifying differerent pressure zones. Taken with permission from (Dragnevski, 2012). 65

Figure 3-10: Illustrating a tensile/compression miniature stage of an ESEM machine. Taken with permission from (Dragnevski, 2012) 66

Figure 4-1: Comparison of the compressive behaviour of R71 and R110 (T=23°C, $\dot{\varepsilon} = 10^{-3}\,s^{-1}$), when tested in three mutually perpendicular directions. 69

Figure 4-2: Compressive loading and unloading behaviour of Rohacell foam (T=23°C, $\dot{\varepsilon} = 10^{-3}\,s^{-1}$), in four foam densities..... 70

Figure 4-3: Tensile test stress-strain results (T=23°C, $\dot{\varepsilon} = 10^{-3}\,s^{-1}$), and strain rate dependency of tensile strength. 71

Figure 4-4: Tension/compression asymmetry of measured yield stress vs. relative foam density (T=23°C, $\dot{\varepsilon} = 10^{-3}\,s^{-1}$). 73

Figure 4-5: Shear stress-strain plots (T=23°C, $\dot{\varepsilon} = 10^{-3}\,s^{-1}$) of all four Rohacell foam densities investigated (shown on right), and an example of R51 failing under shear load (shown on left). 74

Figure 4-6: Indentation test apparatus, using laser extensometer and white stripes positioned close to the ball indenter to measure displacement, and load-cell readings to measure indentation force. 77

Figure 4-7: Measured indentation force versus displacement response for the four foam densities. An illustration of the indentation test is shown on the right..... 78

Figure 4-8: Scaling of elastic and plastic properties with the relative density of the foam (the scales of both axes are logarithmic, T=23°C and $\dot{\varepsilon} = 10^{-3}$ s^{-1}). Average values are reported; the data scatter was less than 5% on all properties. 79

Figure 4-9: ESEM micrographs of the four foams investigated in this study, showing the variation of material microstructure with relative density. 81

Figure 4-10: An example of a single R200 cell and the level of detail of the cell wall geometry shown on the right. 81

Figure 4-11: ESEM scans from an in-situ compression test on the R200 foam; uniform plastic deformation is followed by strain localisation initiated by plastic bending of the cell walls. 83

Figure 4-12 Left: ESEM scans from an in-situ compression test on the R51 foam, showing cell wall buckling followed by elastic unloading. Right: similar ESEM scans for foam R200, showing cell wall plastic bending, with permanent deformation upon unloading. 84

Figure 5-1: Experimental data gathered from the SHPB test, showing the incident and reflected voltage readings (a) at a strain rate of 1500 s^{-1} (b). The axial force histories on the two ends of the specimen indicate stress equilibrium (c). The processed data is used to obtain the dynamic compressive stress-strain curve (d). 94

Figure 5-2: Compressive stress-strain response of Rohacell foam, tested at room temperature and different strain rates (T=23°C, $\dot{\varepsilon} = 10^{-3}$ to 10^{4} s-^{1}); (a) R51; (b) R71; (c) R110; (d) R200. 97

Figure 5-3: A sequence of photographs taken during compression testing of R200, (a) at quasistatic (T=23°C, $\dot{\varepsilon} = 10^{-3}\,s^{-1}$) and (b) at high strain rate (T=23°C, $\dot{\varepsilon} = 10^{3}\,s^{-1}$) loading conditions. 98

Figure 5-4: Summary of the sensitivity of the compressive collapse stress to the imposed strain rate (T=23°C, $\dot{\varepsilon} = 10^{-3}\ \text{to}\ 10^{4}\,s^{-1}$), for all the foams tested in this study. 99

Figure 5-5: R200 and R51 test samples post SHPB experiment 102

Figure 5-6: Compressive stress-strain response of Rohacell foams at a strain rate of $\dot{\varepsilon} = 10^{-2}\,s^{-1}$ and different temperatures in the range 203-473 K ; (a) R51; (b) R71; (c) R110; (d) R200. 105

Figure 5-7: Photographs of foam specimens after quasi-static compression (up to densification strain) at temperatures of 203 and 473 K. 106

Figure 5-8: Summary of the sensitivity of (a) the foams' Young's modulus E and (b) the collapse stress to temperature (T=203-473 K, $\dot{\varepsilon} = 10^{-2}\,s^{-1}$), for all foams tested in this study. 107

Figure 5-9: (a) Comparison of two stress/strain responses of R200 at $\dot{\varepsilon}$=10^{3} s^{-1}, T =298 K and $\dot{\varepsilon}$=10^{-3}, T =203 K; (b) comparison of three stress/strain responses of R51: $\dot{\varepsilon}$=10^{3} s^{-1}, T =298 K and $\dot{\varepsilon}$=10^{-3} s^{-1}, T =203 K and $\dot{\varepsilon}$=10^{2} s^{-1}, T =298 K. 109

Figure 5-10: Similarity of the high strain rate response of R200 and R51 at room temperature and the quasi-static response of the same foam at 203 K. 109

Figure 5-11: Measured collapse stress as a function of temperature; data obtained at different strain rates was mapped to the temperature axis by using equation [5-3]; (a) R51; (b) R71; (c) R110; (d) R200..... 113

Figure 5-12: Normalised apparent foam stiffness versus temperature. Predictions from Eq. [5-5] are compared to experimental data for all foams tested 115

Figure 6-1: Block of Rohacell foam pre-crushed to 50% strain, and resulting stress-strain curve calculated from force-displacement readings off the Hounsfield machine 120

Figure 6-2 Schematic of specimen samples cut out of pre-crushed Rohacell foam..... 120

Figure 6-3: Tensile stress-strain curves for virgin & pre-crushed Rohacell foam (R51 & R200), conducted parallel (axial) and perpendicular (transverse) to initial crush (T=23°C, $\dot{\varepsilon} = 10^{-3}$ s^{-1})..... 121

Figure 6-4: Compressive stress-strain results of virgin and pre-crushed transversely loaded R51 and R200 (T=23°C, $\dot{\varepsilon} = 10^{-3}$ s^{-1}). 124

Figure 6-5: Specific residual foam stiffness at 50% pre-crushed strain, for foams R51 (left) and R200 (right), relative to the virgin material, in axial and transverse directions (T=23°C, $\dot{\varepsilon} = 10^{-3}$ s^{-1}). 125

Figure 6-6: Specific residual foam strength at 50% pre-crushed strain, for foams R51 (left) and R200 (right), relative to the virgin material, in axial and transverse directions (T=23°C, $\dot{\varepsilon} = 10^{-3}$ s^{-1}). 126

Figure 6-7: Deformation behaviour of pre-crushed R200 (top) and R51 (bottom) under transverse tensile loading..... 128

Figure 6-8: Three-point-beam bending apparatus, R51 pre-crushed specimen shown prior to failure (left image) & post failure (right image) 130
Figure 6-9: Force versus displacement 3-point-bend test results of R51 and R200, in their virgin (left) and pre-crushed (right) state..... 131
Figure 6-10: Schematic of geometry of three-point-bend test specimen from material with unequal tensile and compressive properties. 133
Figure 6-11: Measured versus predicted stiffness (slope), using equation [6-11] (assumes unequal moduli) and equation [6-12] (assumes equal moduli)..... 135
Figure 6-12: A graphical representation of the predicted slope and yield load, showing how values can be over or under-estimated if unequal moduli or anisotropic properties are not taken into account..... 136
Figure 6-13: Measured versus predicted yield load, using equation [6-14], for pre-crushed R51 and R200, where virgin and strain-induced anisotropic properties are considered..... 138
Figure 6-14: Normalised specific tensile residual foam stiffness (left) and strength (right) with respect to that of the virgin material, at 0 and 50% pre-crushed strain for R51 and R200..... 140
Figure 6-15: Three-point-bend force-displacement results of R51 and R200 pre-crushed to 25% strain. The predicted slope AB using unequal moduli and anisotropic properties lies between the slope predictions using equal and virgin properties..... 141

Figure 7-1: Measured indentation force versus displacement response for the four foam densities. An illustration of the indentation test is shown on the right..... 146

Figure 7-2: Indentation experiment vs. numerical modelling (Abaqus) simulation 149

Figure 7-3: ABAQUS simulation vs. experimental indentation response ……..150

Figure 7-4: Uniaxial compression experimental results (T=23°C, $\dot{\varepsilon} = 10^{-2}\,\mathrm{s}^{-1}$) for R51 (shown on left) and R200 (shown on right), and the corresponding curve fit using Equation [7-5]..... 153

Figure 7-5: Cross-section of an indentation experiment in LS-DYNA . 154

Figure 7-6 Indentation test results vs. numerical modelling (in both ABAQUS and LS-DYNA) using the Deshpande and Fleck Material model, for all four foam densities. 155

List of Tables

Table 2-1: Rohacell foam material data provided by Evonik Röhm (Evonik Industries AG, 2011) 15

Table 4-1: Measured uniaxial quasistatic mechanical properties of Rohacell foam. 71

Table 4-2: Pre-factors (A) and exponents (b) for power-law fits of the experimental data shown in Figure 4-8 80

Table 4-3: Measured average micro-structural paramters for the four foams under investigation, and predicted relative density according to Gibson and Ashby 82

Table 6-1: Average tensile material properties measured from the resulting stress-strain curves of Figure 6-3 122

Table 6-2: Average material properties measured from the resulting stress-strain curves of Figure 6-4 124

Table 6-3: Measured average 3-point-bend properties 132

Table 6-4: Specimen geometry and material properties derived from the equations provided above 139

Table 7-1: Input parameters for *MAT_154, measured from fitting equation [7-5] to the uniaxial compressive stress-strain curves of R51 and R200 153

Notations

Abbreviations

ESEM	Environmental Scanning Electron Microscope
FBO	Fan Blade off
FE	Finite Element
FEA	Finite Element Analysis
FOD	Foreign Object Damage
GE	General Electric
CFRP	Carbon Fibre Reinforced plastic
LVDT	Linear Voltage displacement Transducer
NASA	National Aeronautics & Space Administration
OR	Open Rotor
PMMA	Polymethylmethacrylate
PTFE	Polytetrafluoroethylene
SHPB	Split Hopkinson Pressure Bar
UDFs	Unducted Fans

Symbols

Roman letters

A	area
A_b	cross sectional area of bar
A_s	cross sectional area of specimen
b	beam width

$C_{1,2,3}$	numerical constant
c_s	longitudinal wave propagation speed
D	bending stiffness
E	elastic modulus
E_0	initial elastic modulus
G	shear modulus
h	height (or depth)
l	length
M	moment
P	load
t	thickness
T	temperature
T_g	glass transition temperature
T_0	room temperature
u_c	cross-head displacement
$u(t)$	axial displacement at a given time
V	volume
υ^p	plastic coefficient of contraction
w	flexural deflection
Y	yield stress

Greek letters

β	material parameter
ε	strain

ε_i	incident strain
ε_t	transmitted strain
ε_r	reflected strain
ε^{Pl}	plastic strain
$\dot{\varepsilon}$	strain rate
$\hat{\varepsilon}$	equivalent strain
ε_F	failure strain
ε_D	densification strain
γ	material parameter
σ	stress
σ_D	dynamic plateau stress
σ_{pl}	plateau stress
σ_{Yc}	compressive yield stress
σ_{Yt}	tensile yield stress
σ_{Ft}	tensile failure stress
σ_m	mean stress
$\hat{\sigma}$	equivalent stress
τ_Y	shear yield stress
τ_F	shear failure stress
ρ	density
$\bar{\rho}$	relative density

ϕ	yield function
$R(\hat{\varepsilon})$	strain hardening

Indices

c	compression
f	foam
pl	plateau
t	time or index for tension
y	yield

Chapter 1

Introduction

1.1 Background and Motivation

Soaring fuel prices and environmental pressures are forcing the aviation industry to design new engine technologies that provide more fuel-efficient flights and produce less carbon dioxide. Clean Sky, one of the largest European research projects, has brought together most of Europe's aerospace companies in an effort to reduce CO_2 and NO_x emissions, reduce aircraft noise and establish a green design by 2020 (Nathan, 2008). The Clean Sky consortium includes companies such as Rolls-Royce, Safran, Airbus, Dassault and Agusta Westland. As part of the Clean Sky project, Rolls Royce is currently developing a new engine, termed the Open Rotor (OR) engine, which will target the narrow-bodied, single-aisle aircrafts that are used on the medium-haul routes. The new engine is based on the turboprop concept. The turboprop, which was first developed in the 1930s, is a geared engine which drives a single propeller and is currently used to power smaller, low-speed aircrafts (see Figure 1-1).

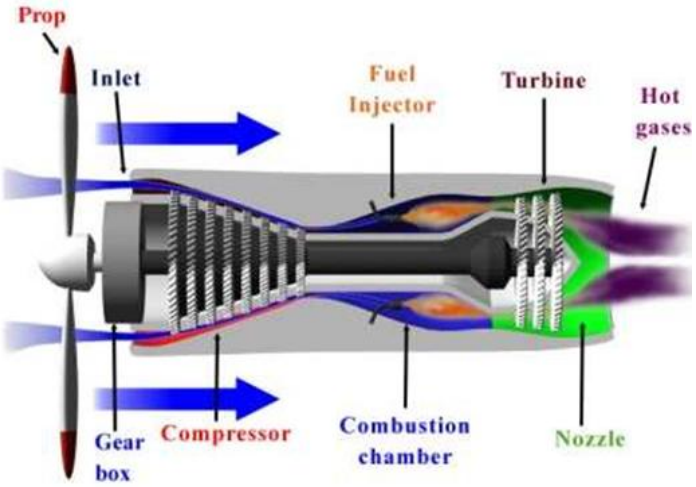


Figure 1-1: A typical Turboprop engine (Toffsworld.com, 2012)

In the late 1980s, General Electric Plc. (GE) and the National Aeronautics and Space Administration (NASA) designed and tested a new engine which made use of contra-rotating blades to boost efficiency (see Figure 1-2). These engines, which were a hybrid between a turboprop and a turbofan engine, were termed propfans or UnDucted Fans (UDFs) and were never produced commercially because fuel prices decreased and the high level of noise associated with the rotation of the contra-rotating blades reduced their commercial advantage.



Figure 1-2: GE and NASA's UnDucted Fan design in the late 1980's (www.aerospaceweb.org, 2012)

The open rotor concept currently being investigated by Rolls Royce is very similar to GE and NASA's UnDucted fan design of the late 1980s. However, it makes use of new and novel technologies, composite materials and innovative design and manufacturing techniques to produce light-weight structures and reduce fuel burn. It consists of two propellers on the same turbine rotating in opposite directions, and is expected to reduce specific fuel consumption and CO_2 emissions by 25-30% relative to current equivalent turbofan engines.

In addition to the open rotor design, Rolls Royce is also working on a new generation of engine which comprises composite fan blades enclosed within a containment casing made up of a hybrid of composite materials (see Figure 1-3). In 2008, a joint venture between Rolls Royce and GKN Aerospace was started to bring this new technology, which promises much lighter and more efficient engines, to the market. The use of light-weight composite materials at the front of the engine allows the centre of gravity to shift rearwards thus permitting the use of a lighter pylon. This in turn leads to a lighter wing, which ultimately reduces the amount of fuel required to power the engine. This new lightweight technology is aimed at developing a new engine which is likely to appear by the end of the decade. Rolls Royce is aiming to develop its composite technology and potentially displace its rival GE (which, since 1995, has carved its own niche within composite blade technology) by securing a deal to power Boeing's next generation 777x engines (Robinson, 2012).



Figure 1-3: Composite fan case system (www.gkn.com, 2012)

In conventional engine designs, the containment casing is the heaviest component in an aero engine and performs the invaluable task of protecting the aircraft and passengers from a potentially hazardous situation, should a fan blade be released during flight. In a Fan Blade off (FBO) event, the use of composite fan blades has a certain advantage over their titanium counterparts, in that the relatively brittle response of Carbon Fibre Reinforced Plastic (CFRP) material used for the blades means that, upon release, the blade shatters into much smaller pieces. This means that although the same energy is retained, the smaller fragments distribute the kinetic energy around the casing. This leads to the potential use of a hybrid of lighter composite materials to form the containment casing system.

Cellular materials are increasingly being exploited for use in such applications. The design philosophy behind their use is to absorb the kinetic energy of the release blade in an FBO event and distribute the load, hence, minimising the peak stresses in the casing. In addition, the hybrid construction must also retain sufficient integrity and strength to protect the casing barrel from

any further direct contact with debris. The conceptual design of the composite fan containment casing is much more complex than typical sandwich structures. This design is “non-symmetric” in that it is composed of various layers of cellular and composite materials which are laid up with different compositions and thicknesses, all of which are intricately chosen to meet certain design intents over the entire life of the engine.

The open rotor blade also exploits the unique combination of properties offered by cellular solids. The conceptual design for the open rotor blade follows the more conventional “symmetric sandwich structure” design, consisting of two composite face sheets of similar material and thickness, separated by a lightweight foam core (see Figure 1-4). The core primarily resists the transverse shear loads and increases the bending stiffness of the structure by holding the faces apart.

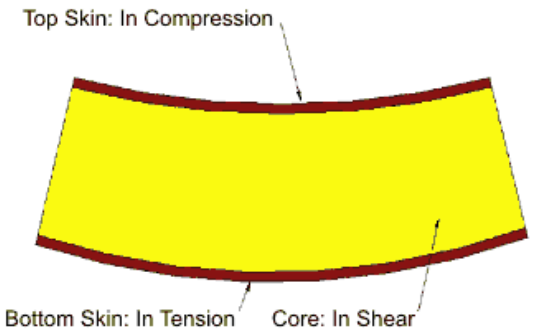


Figure 1-4: Typical symmetric sandwich construction, as used in the open rotor concept design (Gundberg, 2012)

One of the main challenges designers face with the open rotor design is the need to compensate for the possibility of a blade release. This is an extremely challenging task as a competing requirement of the design is that the propeller blades are much lighter and thinner than conventional propeller

blades. Hence, in order to evaluate and validate engine safety, expensive testing programs are required.

The possible cause of an incident which may lead to blade release is normally due to environmental effects such as birds or ice impacting the blades, and is often referred to as soft body impact. Other impact events can include objects such as tyre debris, engine parts, stones or gravel etc., and are often referred to as hard body impact or Foreign Object Damage (FOD). In most cases, such impacts do not lead to the release of a fan blade. However, by virtue of low bending stiffness of thin composite faces, and the relatively low strength of light-weight foam cores, local crushing may occur, affecting the residual strength of the structure.

Since designers are under constant pressure to design thinner, lighter structures, it has become ever more important that environmental effects are fully understood, evaluated and considered as part of engineering design calculations. The use of light-weight cellular materials also requires an understanding of strain rate and temperature effects, as these materials can be used in harsh environmental conditions as critical engine components. A typical fan blade upon release may have a tangential velocity of up to 400 m/s. The resulting impact loads imparted on the composite casing components may well exceed strain rates of 100 s^{-1}, with the typical temperature range varying from -50 to 100°C depending on the flight path etc.

Engineers must therefore fully understand how various engine parts will behave under complex impact loading. Due to the increased cost of engine testing, engineers are turning to analytical techniques such as Finite Element

Analysis (FEA) to analyse most of their problems. These predictive techniques have been used to model material behaviour and the accuracy of the results has led to an increased confidence in the components' predicted performance. Consequently, as FE simulations improve, there is less need to perform expensive tests on model prototypes. However, engineers need to have a good understanding of the constitutive behaviour of the materials being tested in order to produce an FE material model that can accurately predict the deformation behaviour.

Aero engine designers need to demonstrate the capability of these concept designs prior to incorporation into production aircrafts. Hence, a considerable amount of research and development is currently underway to generate damage tolerant solutions for these new structural designs.

1.2 Main Research Objectives

The mechanical behaviour of foam materials is quite complex due to the cellular structure of the material, and the literature on these materials, especially at high loading rates and different temperatures, is limited. The foam material under investigation is a closed-cell rigid Polymethacrylimide (trade name Rohacell) foam, manufactured by Röhm GmbH Ltd. in Germany, and exists in different grades and densities. Rohacell WF (grade with increased heat distortion resistance) serves as a core material for advanced composites in aircrafts and is available in four foam densities. The use of this material as a core material in an open-rotor blade or as part of a lightweight composite casing system is of great interest to designers who are under constant pressure to create thinner, lighter structures. Due to a lack of data and understanding of most foam materials at various loading rates, especially at high rates that occur during severe impacts, designers tend to over-design, resulting in non-optimised, heavy and costly solutions. The availability of better knowledge of these foam materials, in particular of adequate data on their mechanical properties, and more confidence in the ability of FE models to predict their behaviour under impact loading, would allow designers to adopt a much bolder approach in creating an optimised blade and casing system which took advantage of the unique high specific bending stiffness and load-spreading capability of the foam and its exceptional light-weight.

In this thesis, a novel comprehensive study into understanding the mechanical behaviour of Rohacell foam at different densities, loading rates and temperatures is carried out. Improved experimental techniques are employed to

obtain key mechanical properties, such as stiffness, plateau and yield strength, and densification strain. Environmental Scanning Electron Microscope (ESEM) observations combined with in-situ experiments are used to gain vital information regarding the deformation mechanisms of the foam microstructure. The examination of strain rate and temperature effects increases our knowledge of the underlying mechanism of deformation of the chosen cellular foam material at different foam densities. To help assure an accurate damage tolerance analysis, residual foam properties are also measured and used to inform designers of the potential detrimental effect of accidental or impact damage on the residual strength and stiffness of the material.

The strategy deployed to meet the objectives set out in this thesis will be further justified in the literature review. To facilitate this comprehensive study, Röhm GmbH Ltd. in Germany have supplied four blocks of aerospace grade Rohacell foam in four foam densities. The knowledge gained from this study will provide designers with an extensive material data-set and will fill in some of the gaps in the current understanding of cellular materials.

Chapter 2

Literature Review

In this section, a brief overview of the “state-of-the-art” published work on the theories and ideas relevant to the research project is provided. An overview of foam materials is first given with a brief description of the manufacturing processes involved. The material under consideration is then introduced and a summary of some early seminal work on the deformation behaviour of foam materials is presented. This section draws on the invaluable experience and work of Gibson and Ashby (1999) who provide a solid foundation of knowledge towards understanding cellular structures. More advanced publications, where strain rate and temperature effects, and the pre-crushed behaviour of the material being investigated is discussed, are then reviewed. The final section discusses the gaps in the current “state-of-the-art” and highlights our research strategy towards addressing these gaps.

2.1 An Overview of Foam Materials

Foam materials are cellular structures with a random three-dimensional array of cells. Their use as a core material in structural sandwich components for providing high specific strength and stiffness, and the ability to absorb and mitigate the load under impact loading is widespread. These include military applications, sports and leisure products, packaging and transportation, the automotive and aerospace industry and many consumer products. Foamed materials are generally found in the form of polymer foams, metallic foams or ceramic and glass foams (see Figure 2-1).

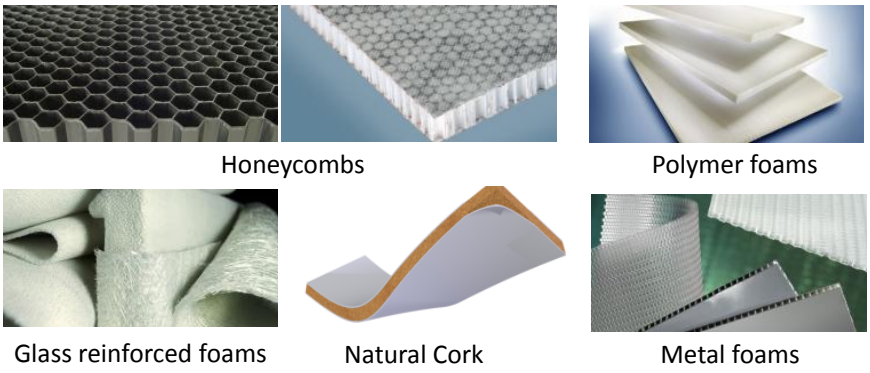


Figure 2-1: Various core materials used in sandwich constructions (Stewart, 2010)

With the increasing need for lightweight structures in today's aerospace and automotive industries, the body of literature on metallic, ceramic and glass foams is growing at a substantial rate *(Wang et al., 2006; Tan et al., 2005; Li et al.*, 2009). Polymer foams have been around for many years, especially in their natural occurring state e.g. wood, bone, corks, sponges, etc. Synthetic polymer foams, on the other hand, were introduced to the market approximately 50 years ago (Eaves, 2004) and their commercial use is increasing.

Foamed polymers are generally produced by introducing gas bubbles into the polymer matrix. The gas is introduced either by mechanical stirring or by mixing a substance that produces a cellular structure in the polymer mass, referred to as a blowing agent. The blowing agent can be in the form of a gas that expands when pressure is released or even a chemical agent that reacts to heat/catalyst to produce a gas (Eaves, 2004). Alternatively, liquids with a low boiling point are mixed with the polymer and the whole substance is boiled. The evaporation of the liquid leads to gas bubbles being created which expand the polymer. Blowing agents are an important part of foam creation as they control the foam density and affect the cellular microstructure of the foam. In some cases, during the formation of the foam the blowing agent is retained in the cellular structure and the cell walls remain solid such that each cell is sealed off from its neighbour, forming what is known as closed-cell foams. These foams can serve as excellent thermal insulators, especially when suitable blowing agents of low thermal conductivity are used. In other cases, these closed-cell foams may undergo another process called reticulation (Gibson & Ashby 1999), where the faces of the cell walls rupture and the blowing agent escapes, hence forming an open-cell foam. In these foams, the solid of which the foam is made is contained in the cell edges and the cells connect through open faces.

2.2 Rohacell Foam

Polymethacrylimide or “Rohacell” foam (PMI), as marketed by Röhm in Germany (Evonik Industries AG, 2011), is a copolymer, which, in its usual definition, is a polymer derived from two or more monomeric species, in this case methacrylonitrile (C_4H_5N) and methacrylic acid ($C_4H_6O_2$), with a few key additives, including a foaming agent (see Figure 2-2).

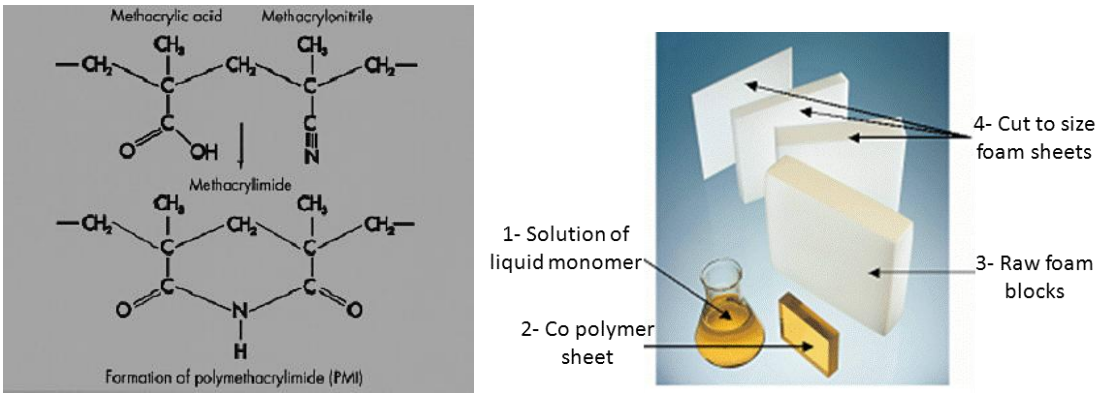


Figure 2-2: Chemical formation of PMI foam (left), and the key manufacturing steps (right), courtesy of (clarasonic.com, 2010)

During the foaming process, the liquid copolymer is solidified and Rohacell is produced by thermal expansion of the copolymer sheet in large ovens at high temperatures (temperatures above the glass transition temperature, ~140°C, but below the decomposition temperature, ~240°C (Brydson, 1999), with alcohol used as a blowing agent; consequently, Rohacell contains no fluorinated carbon hydrates and is halogen free. As soon as the foam block is ready, it is separated into panels and cut to the desired sheet size.

This material is commonly used as a core material in sandwich constructions such as helicopter rotor blades. In the early 20th century, when

helicopters were first invented, the rotor blades were made from metal, canvas or wood. However, the idea of using more flexible material for these structural parts became widespread in the late 1960s, and soon after, carbon fibre composite materials were considered for rotor blades. Eurocopter UK, for example, has relied on Rohacell as the core of a sandwich structure for their helicopter rotor blades since 1996. One of the main advantages of using Rohacell foam, as opposed to metallic structures, is the outstanding fatigue life of the material. The useful life of Rohacell foam is four to five times longer than aluminium-titanium metal structures (Siebert, 2010). This excellent fatigue behaviour enables the foams to endure the range of vibration loads to which the rotor blades are exposed.

One of the main manufacturing advantages of Rohacell foam is its thermoformability, which means it can be formed to any shape when heated to a certain temperature. Rohacell requires a temperature of 180 to 200°C to be formed and upon cooling will keep that form. Another advantage is that Rohacell has a good resistance to compressive creep and can be used under high temperatures and high pressures; thus, it can be autoclaved at 120°C as part of a conventional co-cure operation (Evonik Industries AG, 2011). It is easily machinable and does not react aggressively with most commercial solvents (e.g. acetone, styrene etc.). A weakness of Rohacell is that it is hygroscopic; it absorbs moisture and tends to expand with increasing relative humidity. However, investigations carried out by Röhm suggest the effect of moisture on the mechanical behaviour of the foam is almost negligible if Rohacell is used as a sandwich core material.

Table 2-1 provides the basic Rohacell material data supplied by Röhm. It should be noted that these values are claimed to be nominal data values with no indication of the loading rates applied.

Manufacturers Material Data (Nominal Values)	Rohacell 51wf	Rohacell 71wf	Rohacell 110wf	Rohacell 200wf
Density (kg m^{-3})	52	75	110	205
Tensile Strength at Break (MPa)	1.6	2.2	3.70	6.80
Elongation at Break (%)	3	3	3	3.5
Modulus of Elasticity (MPa)	75	105	180	350
Compressive Strength (MPa)	0.8	1.70	3.6	9
Shear Modulus (MPa)	24	42	70	150
Shear Strength (MPa)	0.8	1.30	2.4	5

Table 2-1: Rohacell foam material data provided by Evonik Röhm (Evonik Industries AG, 2011)

2.3 Deformation Mechanisms in Foam Material

2.3.1 Compressive Deformation

Figure 2-3 shows a typical compressive stress-strain curve for foam materials exhibiting elastic-plastic behaviour. In compression, at low stresses, an almost linear-elastic region is seen, followed by a long stress plateau region where the stress is generally constant, and finally a “densification” region where the stress is seen to rise rapidly.

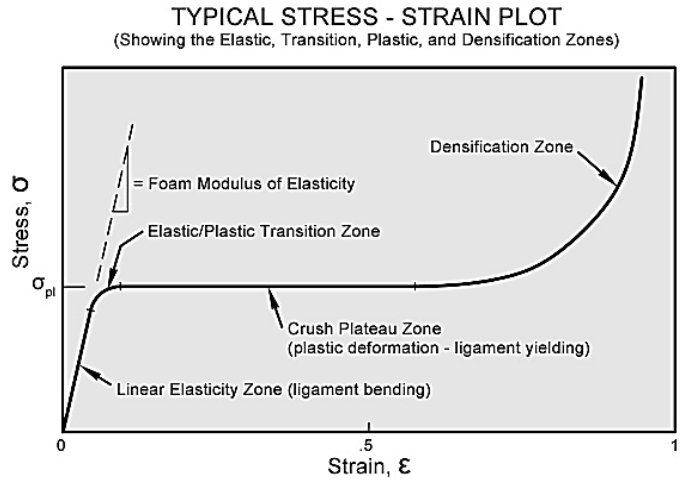


Figure 2-3: A typical compressive stress-strain curve for cellular materials, courtesy of (ERG Aerospace Corp., 2009)

Each region identified is associated with a certain deformation mechanism which can usually be observed using microscopic tools, e.g. the use of an SEM machine or high speed photography (Dragnevski, 2012; Balzer et al., 2004). In the initial region of loading, cell walls, which act as beams or ligaments of the structure, start to bend in a linear elastic manner. If the cells are closed, linear elasticity is also controlled by cell face stretching. In general, the literature shows that the Young’s Modulus, E, can be determined by

measuring the initial slope of the stress-strain curve. However, Ashby (Ashby et al. 2000) note that localised plasticity in the specimen at stresses well below the compressive strength of the foam reduces the slope of the loading curve. As a result, they recommend taking measurements of the Young's modulus from the slope of the unloading curve, a typical example is shown in Figure 2-4.

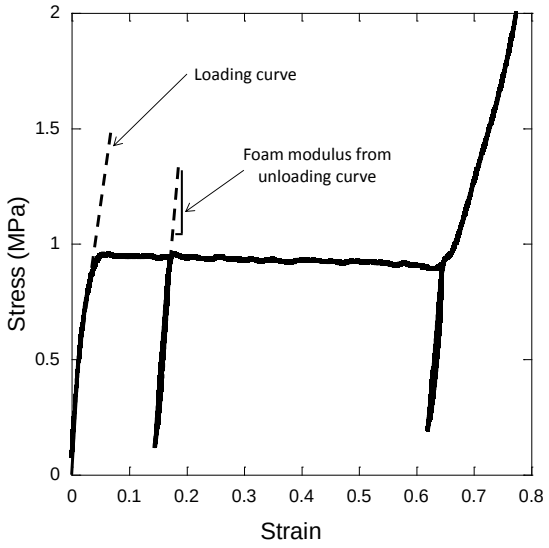


Figure 2-4: A typical compressive stress-strain plot (T=23°C, $\dot{\varepsilon} = 10^{-2}\ s^{-1}$) demonstrating loading and unloading curves, courtesy of (Arezoo *et al.*, 2011).

In the linear elastic region the cell bending continues until a critical stress is reached and the cell walls start to collapse. The foam material then starts to crush by buckling and plastically bending the cell walls. In elastic materials (such as rubber), the buckling of the cell walls occurs in an elastic manner and can be recoverable. However, in brittle materials (such as ceramics), the cell walls collapse in a non-recoverable brittle fracture manner, and where materials yield in a plastic manner (such as metals or polymers), the cell walls collapse from plastic hinges forming at the section of maximum moment in the bent members (Gibson & Ashby 1999). With increased strain,

the cell walls continue to collapse until opposing walls start to meet. At this point, further deformation involves compressing the solid material of the cell wall, which in turn leads to a steep stress rise in the final region, defined as the "densification" region.

In general, raising the relative density of foam material increases the Elastic Young's modulus and raises the stress plateau region whilst reducing the strain where densification occurs (Mills 2007; Gibson & Ashby 1999; Arezoo *et al.* 2011; Eaves 2004; Subhash *et al.* 2006).

2.3.2 Tensile Deformation

Tensile deformation occurs in a manner different from that seen in compression. In elastic materials, at larger strains, the cell walls no longer buckle, rather, they rotate and stretch towards the tensile axis giving rise to structure stiffness (Gibson & Ashby 1999). The cell walls of foams under plastic deformation also rotate toward the tensile axis; however, they also behave in a manner similar to that in compression, with plastic hinges forming to allow for large deformations. Further strain requires the plastic extension of the cell walls themselves, which leads to a rising stress load, ultimately truncated by fracture. The changes in geometry during tensile deformation usually allow the material to be stronger in tension than in compression.

Zenkert *et al.* (2009) reported uniaxial compression and tension experiments on three densities of Rohacell WF foams ($\rho = 51, 110, 200\ \mathrm{kg\,m^{-3}}$). Their results showed that for foams of low density, the compressive strength was lower than the tensile strength. The opposite was found for foams of higher density. They argued that this was due to the occurrence of elastic

buckling of the cell walls for the low-density foams, but provided no supporting evidence for this. Gibson & Ashby claim that brittle foams fail at lower strengths in tension than they do in brittle compression crushing. This is due to their abrupt brittle fracture. This is usually brought about by a crack initiating at a weak cell wall or a pre-existing flaw which propagates in a catastrophic manner. Some foams (such as rigid polymer foams) behave in a plastic manner in compression, but are observed to be brittle in tension. This is due to the effect of stress concentration surrounding cracks initiated on the cell walls in tension, which in turn leads to failure occurring early on, due to cell wall failure. The findings of Zenkert *et al*. (2009) combined with Gibson's discussion on deformation of foam materials would suggest the lower Rohacell foam density behaves as an elastic-plastic foam, whereas with increase in foam density the behaviour transitions to a brittle foam. Unfortunately, this has not been investigated in the literature, and it is intended that the existing gap in the literature is filled by conducting in-situ compression and tensile tests using Scanning Electron Microscope (SEM) observations to fully understand the microscopic deformation mechanisms of the low and high-density foam.

It must be noted that although the mechanical behaviours discussed above generally apply to both open-cell and closed-cell foams, a more complete description for closed-cell foams must include the deformation of the cell faces, as well as the edges, and the response of the gas contained within the cell.

2.4 Microscopic Foam Models and Scaling Laws

Several researchers have developed models for the mechanical behaviour of foams for a variety of loading paths. An excellent piece of work is that of Gibson and Ashby (1999), who investigated the structure of cellular materials such as honeycombs, metallic and polymer foams and developed relationships between the macroscopic behaviour of these foam materials and the solid (parent) material of the cell walls. By modelling these structures as simple cubic array of members, and with the simple use of beam theory, scaling laws were developed to predict the mechanical response of these materials under various loading conditions. For example, in its most simple form, Gibson & Ashby used the geometric properties of the cell to show a relation between the cell shape and dimensions and the relative density (i.e. the density of the cellular material divided by the density of the raw solid material from which the cell walls are made). By using the cell edge-length (*l*) and the cell wall thickness (*t*), where *t*<<*l* (i.e. the relative density of the foam is small), they developed the following equation for all closed-cell foams with faces of side *l* and uniform thickness *t*:

$$\frac{\rho_f}{\rho_s} = C\frac{t}{l}, \qquad [2\text{-}1]$$

where ρ_f and ρ_s are the densities of the foam and cell-wall material, respectively, and C is a numerical constant that depends on the details of the cell shape. Once the properties are calculated in terms of t and l and converted to the relative density using equation [2-1], a single numerical

constant C remains which is determined by making a single experimental measurement and calibrating the results for all densities.

The development of these scaling laws goes as far back as 1959 (Gent & Thomas, 1959) when researchers first began idealising unit cell geometries to resemble the cellular microstructure. The macroscopic behaviour of the material as a whole was then explained by extrapolating the deformation of the unit cell and developing theoretical equations which relate the mechanical behaviours, such as strength and stiffness, to the relative foam density (Gent & Thomas, 1959; Lederman, 1971; Ko, 1965). An example of such equations is a simple power law model for Young's modulus of foam materials, described in [2-2], where E_f and E_s are the stiffness of the foam and cell wall material respectively, and n is a numerical constant which differs depending on whether the foam is open or closed-cell.

$$\frac{E_f}{E_s} = \left(\frac{\rho_f}{\rho_s}\right)^n \qquad [2\text{-}2]$$

Gibson & Ashby have further developed these models through Finite Element (FE) modelling and from empirical curve fits to experimental data, and their use for predicting the mechanical properties of open and closed-cell foams and honeycombs proves to be a useful tool in the early stages of concept design when designers require an approximate idea of the mechanical properties of the chosen foam.

Chen and Lakes (1995) developed a micro-mechanical model for Polymethacrylimide (Rohacell) foam based on the tetrakaidecahedral unit cell

shape. These unit cell shapes are based on examination of microscopic images of the material (Figure 2-5).

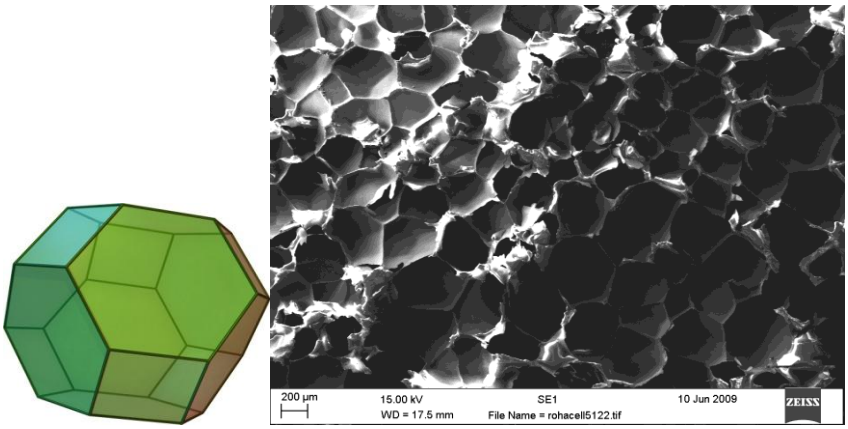


Figure 2-5: A tetrakaidecahedral unit cell (left) and a microscopic image (right) of the low density Rohacell foam (51 kg m^{-3}), illustrating the cell shapes and sizes.

The main role of the micro-mechanical model was to understand the relations between mechanical properties (such as stiffness and strength) and the structure of the cells. The authors took an analytical approach (based on shell theory) and made use of FE methods to define equations similar to that developed by Gibson and Ashby to predict the relative stiffness and strength of Rohacell foam. Examples of such equations are given below:

$$\frac{E_f}{E_s} = \frac{0.343 + 0.823\dfrac{\rho_f}{\rho_s}}{0.684 + \dfrac{\rho_f}{\rho_s}} \times \frac{\rho_f}{\rho_s}, \qquad [2\text{-}3]$$

and

$$\frac{\sigma_{pl}}{\sigma_{ys}} = 0.454(0.417 + \frac{\rho_f}{\rho_s}) \times \frac{\rho_f}{\rho_s}, \qquad [2\text{-}4]$$

where E_f and E_s are the Young's modulus of the foam and cell-wall material, respectively, and σ_{pl} and σ_{ys} are the compressive plateau stress of the foam and the yield stress of the cell-wall material, respectively.

Li *et al.* (2000) studied the uniaxial compressive behaviour of Rohacell 51WF (foam density of 51 kg m^{-3}) and compared the micro-mechanics predictions proposed by Chen and Lakes with their experimental results. The experimental results were seen to compare well with the predictions from Equations [2-3] and [2-4]. It should be noted, however, that Li *et al.* (2000) only studied the compressive behaviour of the low density Rohacell foam (51 kg m^{-3}) and Chen and Lakes (1995) have shown that, although their model compares well with experimental results for low-density Rohacell foam, it is less accurate for the higher densities. This again reiterates the need for investigating the effect of density on the mechanical properties of cellular materials, as the literature appears to show that the complexity of these structures is such that simple scaling laws are not valid for all foam densities.

Gibson and Ashby caution against the use of scaling laws for too wide a range of foam densities, as the simple beam bending concept may not apply at large or very low relative densities. They state that at large relative densities (>0.3), there is a transition from a cellular structure to one that is better described as a solid with isolated voids, where the short and squat cell walls now yield axially (in compression and tension) before they bend. On the other hand, at very low densities (<0.04), it is possible for elastic collapse to precede plastic collapse, hence, invalidating the use of plastic beam bending theory.

2.5 Strain Rate Sensitivity in Polymer Foam Material

A number of studies have found that cellular materials subjected to high velocity impacts (or high strain rate deformation) exhibit an increase in strength, stiffness and energy absorption capability (Mills 2007; Richeton *et al*. 2006; Song *et al.* 2007; Chen *et al.* 2004; Song *et al.* 2008; Subhash *et al.* 2006; Tagarielli *et al.* 2008; Thomas *et al.* 2004; Walley and Field 1994; Gibson and Ashby 1999).

The cause of this apparent "increase in strength" with increasing impact velocity is often identified as a strain rate effect. A number of factors contributing to strain rate effects in polymer foam materials can be identified:

- The inherent viscoelastic behaviour and strain rate sensitivity of the raw polymer of the solid cell wall (e.g. McCrum *et al.* 1997; Mills 2007; Siviour 2005; Gibson and Ashby 1999).
- At high strain rates, the gas enclosed within closed-cell foams is unable to escape on the timescale of the experiment, and an adiabatic increase in gas pressure under dynamic loading is likely to contribute to an increase in the energy required to compress the foam.
- Some researchers argue that the significant stress enhancement seen in foam materials under dynamic loading is not due to material strain rate effects, rather to micro-inertia effects; in particular, more force is required to accelerate the cell walls under impact loading (Reid & Peng, 1997; Harrigan & Reid, 1999).

- Gibson and Ashby (1999) also refer to “localisation” and “densification” as features which influence the overall strength of material under dynamic crushing. They state that at a given instant, the deformation is concentrated into a thin layer or band, often adjacent to the loading face. This localised effect can lead to local strain rates which are much larger than the apparent, nominal, strain rate. In addition, under dynamic loading, cell collapse can be overdriven during densification, causing the stress to rise steeply, commonly referred to as “shock” enhancement.

The uniaxial compressive behaviour of polymer foams has been studied by a large number of researchers. Examples include PVC foam (Thomas *et al.* 2002; Thomas *et al.* 2004; Tagarielli *et al.* 2008), polystyrene foam (B Song 2005), epoxy-based and syntactic foams (Song *et al.* 2007; Chen *et al.* 2004; Li *et al.* 2009). It is generally understood that the stiffness, failure strength, plateau stress and energy absorption of polymer foams show mild strain rate dependency in the quasi-static regime (i.e. for strain rates from 10^{-4} to 1 s^{-1}) and a greater rate sensitivity at strain rates above 100 s^{-1}. A brief review of the most recent work of these authors is described below.

Tagarielli *et al*. (2008) investigated the uniaxial compressive behaviour of two PVC foams (Divinycell H100 and H250) and an end-grain balsa wood (Probalsa LD7) over a wide range of strain rates ranging from 10^{-4} – 10^{3} s^{-1}, at room temperature (T~23°C). The foams are identified by their trade names which comprise a letter followed by the density of the foam in kg m^{-3}. The experiments revealed mild strain rate sensitivity in the quasistatic region. At

higher strain rates, however, the H250 PVC foam and the LD7 balsa wood showed an increase in the plateau strength by a factor of two, compared to the static strength. The plateau strength in this study was defined as the flow stress at a strain of 15%. The compressive response of the lower density PVC foam (H100) was only mildly affected by the high strain rates, displaying only a 30% increase in compressive strength compared to its static strength. These results were compared to other PVC foams of different densities which had been investigated by other researchers and a summary of the measured data is shown in Figure 2-6.

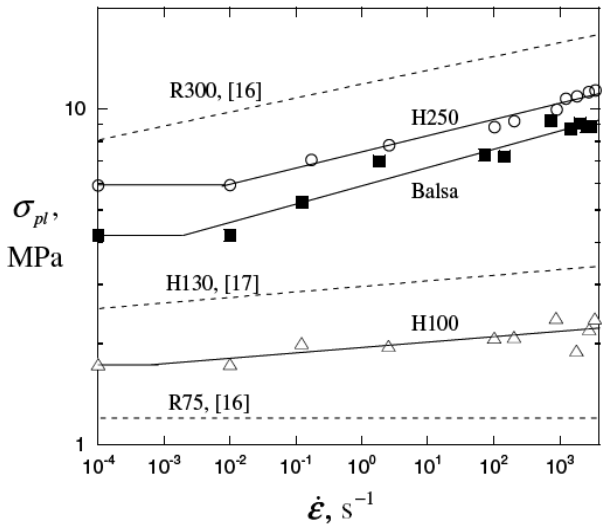


Figure 2-6: Effect of strain rate (T~23°C, $\dot{\varepsilon} = 10^{-4}$ to 10^{3} s^{-1}) on plateau strength of Balsa wood and different densities of PVC foam specimens (Tagarielli et al. 2008).

The figure clearly demonstrates that the strain rate sensitivity of the foam material increases with increased relative density. Subhash *et al.* (2006) also reported this trend when investigating the compressive behaviour of four epoxy-based polymer foams of different foam densities. Li *et al.* (2009) investigated the compressive properties of glass-microballoon epoxy syntactic

foams over a wide range of strain rates (0.001 to 4000 s^{-1}) at room temperature (T~23°C). The results show the compressive peak and plateau stresses are both highly strain rate dependent, increasing in an almost linear manner with the logarithm of the strain rate. The strain rate dependency of the syntactic foam is significantly dominated by the inherent rate sensitivity of the matrix materials. It must be noted that the behaviour of the foam in the densification region was not captured in this study (see Figure 2-7).

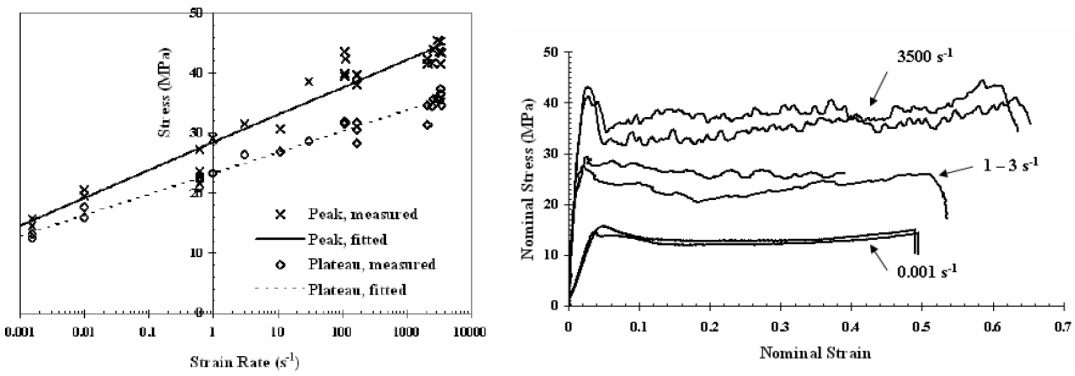


Figure 2-7: Strain rate dependency of the peak and plateau stress (T~23°C, $\dot{\varepsilon} = 10^{-3}$ to $10^{4}\, s^{-1}$) for an epoxy syntactic foam (left) and the resulting stress-strain curves at different loading rates (right), courtesy of (Li *et al*., 2009)

Song and Chen *et al.* (2007) experimentally obtained compressive stress-strain behaviours of an epoxy foam of density 120 kg m^{-3} at low, intermediate and high strain rates. The high strain rate tests were carried out using a Split Hopkinson Pressure Bar (SHPB) system with aluminium alloy bars. Thin cylindrical specimens were used to ensure uniform stress and deformation state in the dynamic experiment. A pulse shaper was situated between the striker and input bar to increase the rise time of the input pulse, this can also help achieve dynamic stress equilibrium and constant strain rate deformation, as recommended by authors, including Chen *et al.* (2002). The resulting stress

strain curves for the epoxy foam at strain rates varying from 0.05 s^{-1} to 2700 s^{-1} are summarised in Figure 2-8 (shown on left) and exhibit the typical stress strain response expected from foam materials as discussed in section 2.3. Figure 2-8 also shows the strain-rate dependency of the modulus of elasticity and plateau stress. The modulus of elasticity is seen to vary between 10 and 30 MPa, the cell wall collapse stress (the point of transition from elastic to plastic zone, also referred to as the yield point) varies from 0.88 MPa to 1.17 MPa, and the plateau stress varies from 0.84 MPa to 1.14 MPa.

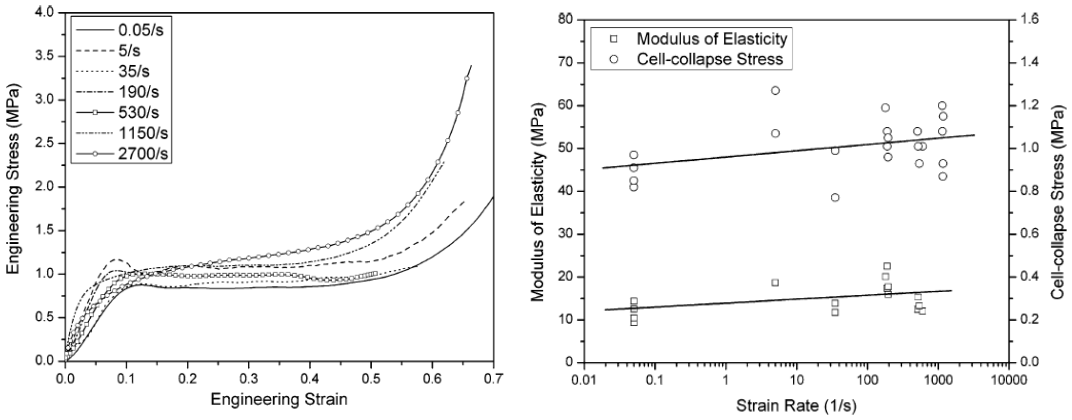


Figure 2-8: Stress-strain curves of an epoxy foam at various strain rates (left) and strain rate effects (T~23°C, $\dot{\varepsilon} = 0.05 \text{ to } 2700\ s^{-1}$) on the modulus of elasticity and cell-collapse stress (right), courtesy of (Song et al. 2007)

Researchers often adopt the criterion of a 20% elevation in strength to define strain rate sensitivity, as this is consistent with the fact that many metallic and non-metallic types of foam can be imperfect materials with dispersion strengths of the order of 20% (Deshpande & Fleck 2000; Wang *et al.* 2006). The results from Figure 2-8 show an enhancement of approximately 30% in stress values; however, the data scatter suggests the strain rate dependency proposed by the authors is not reliable.

Song *et al.* (2005) also investigated the stress-strain behaviour of polystyrene foam over a strain rate range of 0.001-950 s^{-1}. Their results show the elastic modulus (measured as the gradient of the slope upon loading) and the plateau stresses are strain rate sensitive. The elastic modulus is shown to be only slightly strain rate sensitive in the quasistatic range; however, it is much more sensitive at high strain rates. The authors fit the elastic modulus E to the logarithm of the strain rate $\dot{\varepsilon}$ using a piece-wise relationship (see Equation [2-5] and Figure 2-9). An empirical relationship is also defined for the cell-collapse stress, which is seen to vary nearly linearly to the logarithm of the strain rate (see Equation [2-6]).

$$E = E_0 + A\log(\frac{\dot{\varepsilon}}{\dot{\varepsilon}_0}), \qquad [2\text{-}5]$$

$$\sigma_y = \sigma_0 + B\log(\frac{\dot{\varepsilon}}{\dot{\varepsilon}_0}), \qquad [2\text{-}6]$$

where E_0 and A are fitted from experimental results, $\dot{\varepsilon}_0$ is the reference strain rate and σ_0 and B are fitted from experimental results.

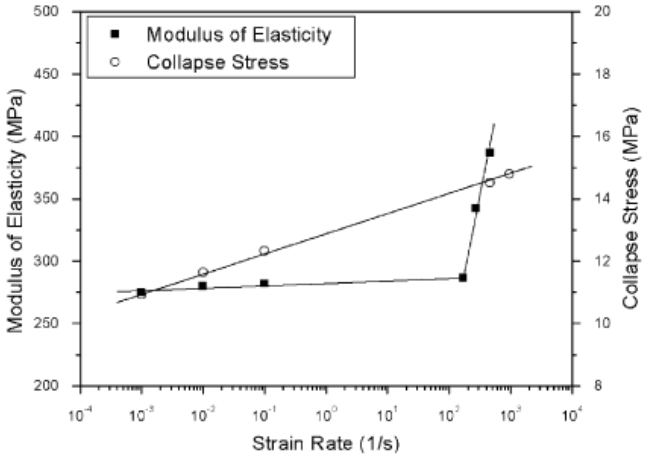


Figure 2-9: Effect of strain rate on elastic modulus and collapse stress of polystyrene foam (T~23°C, $\dot{\varepsilon} = 10^{-4}$ to 10^{4} s^{-1}), courtesy of (Song 2005)

Although two phenomenological models have been presented that describe the strain rate dependency of the elastic modulus and the plateau stress of the polystyrene foam, respectively, it must be noted that the authors have not investigated the response of the foam material at intermediate strain rates (10^0-10^2 s^{-1}). A linear connection is assumed between the quasistatic data and the high strain rate data, due to the lack of medium strain rate data. This assumption should be validated by completing medium rate tests for the polystyrene foam.

Some researchers have studied one-dimensional shock wave propagation in foam materials and state that the apparent increase in stress with increasing impact velocity, which is often identified as strain rate effects, is, in fact, micro-inertia effects due to shock wave loading (Harrigan & Reid 1999). Reid and Peng (1997) investigated the micro-inertia effects of individual cell walls in different types of woods (oak, balsa, pine and redwood) under high-velocity impact loading. Experiments were carried out by impacting the specimens on the end of a Hopkinson bar load cell and measuring the force pulses generated. The results showed that a significant enhancement of the initial crushing strength of the specimens occurs under dynamic loading conditions. They claim micro-inertia effects, which "*relate to the resistance to motion of the cells in the direction of the impact force"* are the reason behind this observed stress enhancement under dynamic loading. They argue cellular materials are prone to respond to impact loading by forming a shock wave, providing the impact velocity is high enough. The authors propose a simple one-dimensional shock model which assumes the foam has a rigid, perfectly-plastic response up to the densification strain ε_D. This model captures two important

features of the non-linear foam: the plateau stress and the densification or lock-up strain. The model (Reid & Peng, 1997) is successful in predicting the enhanced dynamic plateau stress σ_D upstream from the shock wave, and is given by:

$$\sigma_D = \sigma_{pl} + \frac{\rho_f V^2}{\varepsilon_D}, \qquad [2\text{-}7]$$

where ρ_f, σ_{pl} and V are the foam density, plateau stress and impact velocity, respectively. Therefore, an elevation of $\frac{\rho_f V^2}{\varepsilon_D}$ is expected in the compressive strength of the material.

The literature so far suggests a high strain rate dependency of the mechanical properties of polymer foams, where the general trend demonstrates an increase in strength and stiffness with increased strain rate. However, this is not always the case. Song *et al.* (2004) investigated the dynamic compressive behaviour of an epoxy syntactic foam of density 770 kg m^{-3} using a SHPB machine with aluminium alloy bars. To identify the rate effects of the foam, they also performed quasistatic tests and their results showed that the compressive strength of the syntactic foam increased with strain rate up to a transition strain rate of between 550 and 1030 s^{-1}. The dynamic experiments conducted at strain rates above the transition range showed a decrease in the compressive strength of the foam. The authors claim strain-rate-induced damage caused the compressive strength of the foam to decrease, as they observed damage occurring along the direction of 45° to the loading axis. Similarly, Saha *et al.* (2005) also reported a drop in foam strength, when testing in compression at a strain rate of 1300 s^{-1}. They claim the brittle nature of the cell wall material led

to the material disintegrating at high strain rates, resulting in a sudden decrease in energy absorption and peak stress. These results may be better understood in the light of data presented by Walley and Field (1994) who conducted a comprehensive study studying the strain rate effects of solid polymers. Five out of the seventeen polymers they studied showed a decrease in rate sensitivity at strain rates in the region of 10^3 s^{-1}. At the time the authors suggested that this may be a real material rate effect or, alternatively, may be due to the specimens not being in an equilibrium state of stress during the tests. Similar results were also reported by Al-Maliky and Fernandez (1998) who noted drops in yield stress for various polymers at high strain rates.

Some researchers have investigated the strain rate sensitivity of Rohacell foams up to rates of the order of 100 s^{-1} (Li *et al.* 2000; Mines 2007). Their research is focused on the lowest foam density (density = 51 kg m^{-3}) and concludes that the response is scarcely sensitive to strain rate in the region of 10^{-3}-10^2 s^{-1}. The literature however, lacks a comprehensive review of the dynamic mechanical properties of this particular material at different foam densities, when deformed at high strain rates. Consequently, the current study employs a Split-Hopkinson Pressure Bar (SHPB) to establish the stress-strain response of Rohacell foam under high strain rate loading conditions (over seven decades of strain). The strain rate effects are systematically examined and discussed in Chapter 5 of this thesis.

2.6 Temperature Effects in Polymer Foam Materials

It is generally accepted that for polymers, temperature and strain rate dependency are directly linked (see Figure 2-10), where decreasing the temperature has a similar effect as increasing the strain-rate (McCrum *et al.* 1997; Mills 2007; Siviour 2005; Meyers & Chawla 2009).

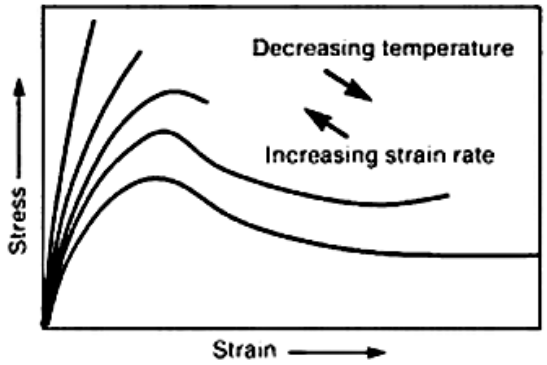


Figure 2-10: Typical stress-strain curve of a polymer material showing the effect of strain rate and temperature (Meyers & Chawla, 2009).

The underlying physical process behind this phenomenon is well described in Williamson *et al*. (2008) and is based on molecular motions exhibited by polymers. The time associated with large scale motion in the structure of a polymer is the relaxation time, which is temperature dependent and decreases with increasing temperature. At high temperatures, there is sufficient thermal energy to overcome the potential energy barriers required for molecular movement, and hence the material can flow. Similarly, given there is sufficient thermal energy available, loads applied over low strain rates (i.e. time-scales greater than the relaxation time) allow the molecules to move in response, resulting in lower stiffness and strength. However, when loads are applied at high strain rates (i.e. time scales lower than the relaxation time), the

molecules do not have sufficient time to respond and remain essentially frozen in place, generally resulting in higher stiffness and strength. Thus, it is clear that decreasing the loading time-scale (increasing strain rate) is analogous to reducing the temperature.

The most well-known equation to describe this time-temperature equivalence is the Williams, Landel and Ferry (WLF) relation (Williams et al., 1955) which relates changes in strain-rate to changes in temperature, for equal stress-strain response, for viscoelastic polymers (see equation [2-8]) .

$$\Delta \log(\dot{\varepsilon}) = \frac{C_1(T - T_g)}{C_2 + (T - T_g)}, \qquad \textit{[2-8]}$$

where C_1 and C_2 are constants. This relation applies over a temperature range T_g to T_g + 50K, and describes the equivalent isothermal difference in strain rate between two experiments performed at the same strain rate, one at the glass transition temperature T_g and another at an elevated temperature T. The potential benefit of the use of this equation is that the number of experiments required to map out the materials response can be limited to one single test machine. Measuring the stress-strain response of a material over low, medium and high loading rates can be time-consuming, complex, and generally requires three sets of test equipment. However, as a first attempt at understanding the material response over different loading rates, the benefit of the time-temperature equation is that experiments can be limited to one test equipment with a limited strain rate range on which the temperature of testing is controllable.

In general, polymer foams inherit the temperature dependency behaviour of the raw polymer of the cell walls. If the temperature is sufficiently decreased, the mode of failure can change from a ductile to an extremely brittle event. This is often referred as the ductile-to-brittle transition temperature. It must be noted that in the case of closed-cell foams, the compressibility of the gas is also dependent on temperature.

While some authors have investigated the response of Rohacell at high temperatures of around 450 K (Evonik Industries 2011), no studies have explored the mechanical response of these foams at low temperatures. In this thesis an experimental study exploring the sensitivity of the compressive elasto-plastic response of all commercially available Rohacell-WF foams to both imposed strain rate (in the range 10^{-3} to 5000 s^{-1}, at temperature 296 K) and operating temperatures (in the range 203 to 473 K, at a strain rate of 10^{-2} s^{-1}) will be presented. The effects of increasing strain rate and decreasing temperature on the foam response will be demonstrated, and a quantitative correspondence between these effects will be established by the time-temperature superposition method. The outcome of this work is presented in Chapter 5 of this thesis.

2.7 Residual Properties of Pre-Crushed Foam

Cellular materials are generally used to their best potential under compressive loading, by absorbing and spreading the load through a combination of buckling and cell wall bending. In aerospace applications, however, these cellular materials are used in more complex and unconventional design conditions, intended on resisting more complex stress states. These materials are generally low in density and, upon handling, assembly or repair, may be subject to accidental loading. This in turn could lead to significant crushing within the material, even before it is subjected to the intended load it has been designed to withstand, thus hindering the design intend and lowering its damage tolerance. Engineers must ensure they account for this in their design calculations. However, research in this area has been limited.

Current literature surrounding the mechanical properties of pre-crushed polymer foams is very limited, and, particularly in the case of Rohacell foam, the literature is generally limited to the lowest foam density. Koissin and Shipsha (2009) investigated the compressive, tensile and shear properties of Rohacell 51wf and various densities of Divinycel foam, in the direction transverse to the initial crush. Their results showed that the Young's modulus of the pre-crushed material remained relatively unchanged to that of the virgin material in compression. In tension, however, an increase in stiffness and strength was observed, albeit with an accompanying decrease in specific stiffness and strength.

Li *et al.* (2000) investigated the tensile behaviour of pre-crushed Rohacell 51wf in the direction parallel to the initial crush. They found that the

tensile stress-strain curve showed similar behaviour to that of the compressive curve, although with a much lower plateau stress. In addition, the tensile strength was significantly lower than that of the virgin material and a significant material ductility was observed. Similar findings were reported in a separate study by Shipsha *et al.* (2003) where shear and tensile tests were conducted on pre-crushed Rohacell 51wf foam.

In this thesis, the residual mechanical properties of pre-crushed Rohacell foam at different foam densities, when loaded parallel and perpendicular to crush will be explored. It will be shown that upon application of strain, Rohacell foams exhibit strain-induced anisotropic properties, where the mechanical response of the material in different loading directions, change, following uniaxial compression. The data obtained from this study will supplement the limited data currently found in the literature and will assist engineers in their design calculations, and will also prove beneficial in Finite Element (FE) simulations for predictive modelling.

2.8 Research Strategy

In the above literature review it has been shown that a significant number of researchers have spent many years trying to understand the complex mechanical behaviours of cellular materials. At the same time, many engineering questions remain unanswered, or the answer is ambiguous. The aim of this work is to fill in some of the gaps and generate scientific and deeper understanding on the behaviours of cellular materials. This study will involve the following:

- The macroscopic mechanical response of Rohacell foam in four foam densities (ranging from 50 to 200 kg m^{-3}) will be investigated using quasistatic compression, tension and shear experiments. The effect of foam density on the measured material response will be analysed, and in-situ SEM observations during quasi-static tensile and compression tests will be used to further understand the microscopic deformation mechanisms dominating the collapse of the foam, and its effect on the macroscopic foam response. The experimental findings from this study will be reported in Chapter 4 of this thesis.
- In Chapter 5, improved experimental techniques will be developed to assess the strain rate dependent mechanical properties of Rohacell foam. This work will entail a broad study which will explore the sensitivity of the foam response to an imposed strain rate over seven decades of strain (in the range $10^{-3} – 10^{4}$ s^{-1}). The findings from this study will be invaluable, as the current “state-of-the-art” has shown no reported high strain rate properties for the chosen foam material, specifically at

different foam densities. The strain rate tests will extend to very high rates (~ $5x10^3$ s^{-1}) to cover the range at which anomalies, such as transition behaviours in strain rate effects, have been reported in literature for polymer-based materials.

- The literature has shown that no studies have explored the mechanical response of Rohacell foam at low temperatures. In Chapter 5 we will explore the sensitivity of the foam response to temperature over a temperature range of 203 to 473 Kelvin. A novel time-temperature superposition will be used to map the sensitivity to temperature of the collapse stress to the strain rate sensitivity of the foam. From the gathered data simple design equations will be formulated, which can be used to predict mechanical behaviours, such as strength or stiffness, as functions of temperature and relative density.
- To understand and quantify the material property changes occurring in cellular materials due to applied strain, in Chapter 6 the mechanical response of the pre-crushed foam material at low and high-foam densities, in different loading directions will be investigated. The focus of this study is to supplement the limited data currently found in the literature to help designers account for the effect of pre-crushing in their design calculations. It will be shown that neglecting these effects will lead to incorrect predictions of the foams structural response.
- In Chapter 7 of this thesis, the new experimental data and novel understanding generated from the previous chapters will be used to inspire and validate numerical constitutive models for the response of

polymer foams, as potential core materials in aerospace sandwich constructions.

- The final chapter of the thesis will provide concluding remarks from the present dissertation and advise on improvements and future work. A list of studies published during this DPhil course will also be provided.

Chapter 3

Experimental Study

In the aerospace industry, conventional metallic components are increasingly being replaced by composite sandwich structures in an attempt to increase specific stiffness and strength, as well as durability; polymer foams are often used as the core of these sandwich structures. Considering the wide range of temperatures at which structural components in an aircraft operate, and as many components are exposed to the risk of impact loading, it is necessary to develop a thorough understanding of the mechanical response of cellular polymers and their sensitivity to both temperature and applied strain rates. The strain rates and temperatures that aerospace components are generally exposed to can vary from 10^{-5} s^{-1} to 10^{4} s^{-1} and 203 – 473 K, respectively. Taking into account both the physical processes that occur and experimental techniques used at different loading rates, strain rates may be classified into three approximate domains. Rates up to 1 s^{-1} are classified as quasi static, up to 100 s^{-1} as medium rate, and between 100 s^{-1} and 10^{4} s^{-1} as high rate.

In the following chapter the relevant experimental methods and techniques employed to characterise the chosen foam material at different loading rates and temperatures are described. Each subsequent chapter will still briefly remind the reader of the experimental techniques employed, however, this chapter will focus on providing a more comprehensive and in-depth discussion of the theory and background behind each experimental technique and the motivation behind the choice of specimen.

3.1 Specimen Preparation and Choice of Geometry

The Rohacell foam material was provided by Röhm Ltd. in Germany (Evonik Industries AG, 2011) as sheet panels of thickness 70mm, in four foam densities: 51, 71, 110 and 200 kg m^{-3}. From here on in, these four materials will be denoted by R51, R71, R100 and R200, respectively. The relative density of each foam was calculated as the ratio of the measured foam density to the density of the parent polymer (obtained from the manufacturer's data sheets as 1416 kg m^{-3}).

3.1.1 Compression Specimens

For *compression testing*, right cylindrical specimens were used. To reduce friction effects between the specimen surface and the loading anvils, lubrication was used (Kuhn, 2000). If the specimen's aspect ratio is too short then the friction between the anvils and the specimen may become too large to obtain meaningful results under uniaxial loading. Without adequate lubrication the specimen is constrained by the friction between the specimen end face and the anvil, which can result in non-uniformity of radial strain, often manifested as barrelling. The use of very long, thin geometry can lower friction effects; however, if the specimen is too slender then buckling may occur. To overcome buckling effects, a low length-to-diameter (L/D) ratio is recommended, where L/D=1 is often used (Deshpande & Fleck, 2000; Holt, 1999). However, in order to perform comparisons between strain rates, a single specimen size is usually used. Specimen thickness is an important parameter to be considered at high strain rates (Dioh et al., 1993). At high rates the stress waves attenuate when

travelling through soft specimens and a thick specimen can often act as a shock absorber instead of a representative volume for material properties (Chen et al. 2002). Furthermore, at high strain rates, the low speed of sound in these materials requires relatively short specimens in order to allow stress equilibrium to be achieved rapidly during the experiments.

Kuhn (2000) performed high rate experiments with several thicknesses of a low impedance material and by measuring the axial forces at both ends of the specimen during the experiment they found that dynamic equilibrium was only achieved during later stages of the experiments for thinner samples. It is therefore desirable that a thin specimen thickness is used to minimise the time required to achieve force equilibrium along the axis of the specimen (Kolsky, 1949). Hence, the specimen design is governed by the requirements of the high rate experiments, and is not optimised for low strain rate experiments.

In this thesis, the Rohacell sheet panels were machined to a thickness of 4mm using the milling machine. Specimens were then cut using a thin walled cylindrical punch of diameter 9mm (see Figure 3-1). With this choice of specimen size approximately six to nine cells were included in all directions.

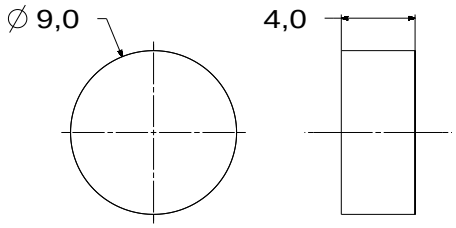


Figure 3-1: Compression specimen 2D geometry

The chosen specimen size agrees with the recommendation given by Ashby *et al.* (2000), who recommend that the smallest linear dimension of the

specimen should be at least seven times the cell size to assume homogeneity and avoid size effects. This recommendation comes from a study conducted by Andrews *et al.* (2001) where specimen size effects on the Young's modulus and the plastic collapse stress of a closed-cell Alporas and an open-cell Duocel foam were investigated. The outcome of their investigation shows that the strength and modulus measurements are independent of size when the sample dimensions exceed about seven cell diameters. This requirement is not confined to foam materials and several authors quote similar measurements when calculating the minimum number of grains required across the diameter of a specimen, for specimen homogeneity in polymer or composite materials (Siviour 2005; Drodge 2011)

In order to ensure the compressive mechanical behaviour of the 4 mm thick specimens were independent of the foam thickness, experiments were also conducted using 10 mm thick specimens and the stress-strain results were compared. Figure 3-2 compares the compressive stress-strain results of R200, measured at a strain rate of 10^{-2} s^{-1} at room temperature (T=23°C), using specimens of thickness 4 and 10 mm (three test results are shown in each case). The curves clearly show the typical nearly linear elastic region, followed by the stress plateau and the steep rise during densification. There are no obvious differences in the compressive behaviours between the 4 and 10 mm thickness foams, thus, it is assumed the measured response is independent of specimen size over this range.

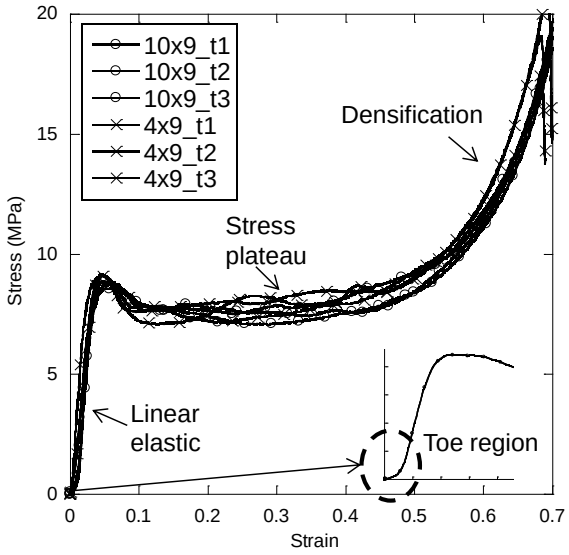


Figure 3-2: Compressive stress-strain curves of R200 (T=23°C, $\dot{\varepsilon} = 10^{-2}$ s^{-1}), 4 mm vs. 10 mm thick specimens

In the early stage of loading, an initial non-linear feature was observed. This non-linear region is often referred to as the “toe” region and does not represent a property of the material (Kuhn, 2000), it is an artefact caused by the take-up of slack and alignment or seating of the specimen. In addition, the loading platens in contact with the specimen were lubricated with Vaseline to reduce frictional effects (Kuhn, 2000). If the lubricant layer is too thick it can contribute to the “toeing-in” on the stress-strain curve, where initial strain is taken up by squeezing the lubricant out of the way. In order to obtain a correct compressive modulus value, this artefact is compensated for to give the corrected zero point on the strain axis by continuing the linear portion of the elastic region of the curve through the zero-force axis. This intersection is the corrected zero displacement point, from which all displacements are measured.

3.1.2 Tensile Specimens

The uniaxial *tensile tests* were performed on samples of material using flat dogbone specimens, with a large length/diameter aspect ratio in the gauge section, in accordance to ASTM D1623-78 (Holt, 1999). Standard dogbone specimens are commonly used to obtain mechanical properties of materials in tension (Zhao, 1996). These specimens have a long parallel gauge section, within which the stress is assumed uniaxial and constant over the gauge width. The smooth transition to the wider shoulders allows the testing machine to apply loads without causing stress concentrations in the gauge section. The tensile test specimen details are given in Figure 3-3.

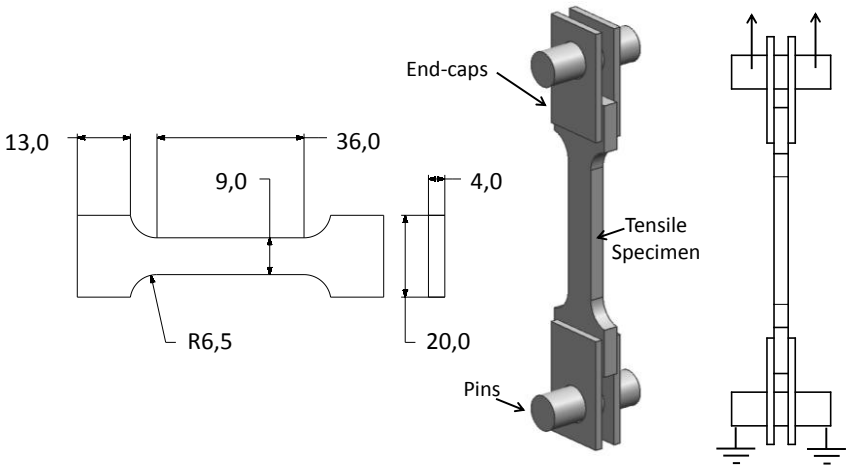


Figure 3-3: Tensile specimen geometry

The uniaxial tensile force was applied to the dogbone specimens through end caps adhesively bonded to both ends of the specimens, using a two-component epoxy-based adhesive (3M Scotch-weld DP490). A pin joining the two end caps allows for axial alignment. An acceptable failure mode occurs within the gauge length, i.e. it is not acceptable if the specimen fails at the bond between the foam and the end caps.

3.1.3 Shear Specimens

Single-lap shear experiments were conducted in accordance to ASTM-C273 (Kuhn, 2000), where the only difference was that the prismatic beam of rectangular cross-section was substituted with an I-shaped cross-section, with shear deformation occurring in the web of the I-beam. This specimen geometry was preferred, as an I-shaped cross-section allows reduction of stresses at the interface between the foam and the metallic fixture used to load it, reducing the risk of premature specimen failure by delamination. The web of the I-shaped cross-section, representing the gauge section of the specimen, had a height of 10 mm and a width of 6 mm, whereas the depth was 120 mm to ensure a high depth to height ratio, in order to minimise edge effects. The thickness and width of the I-beam flanges was of 6 mm and 38 mm, respectively (see Figure 3-4).

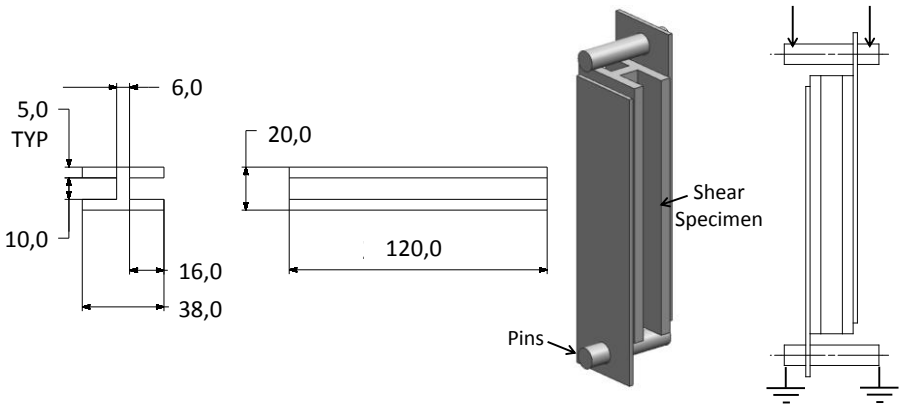


Figure 3-4: Shear specimen geometry

The web was connected to foam flanges by fillets of radius 2 mm. The I-beam was sandwiched between two steel plates and bonded to these by a structural adhesive; the plates were connected to a screw-driven test machine by pin-joints. During the experiment the test machine reduced the spacing between the pin-joints, therefore applying a compressive force on the steel

fixture, resulting in a shear action on the I-shaped foam core. A non-contact laser extensometer of resolution 1µm and gauge length 10 mm was employed to record the relative displacement between the two flanges of the I-beam, thereby determining the engineering shear strain. This test does not produce pure shear, however, a specimen length to thickness ratio of 12 (as recommended by ASTM-C273) has been used in order to minimise the effect of secondary stresses.

3.2 Experimental Apparatus

3.2.1 Quasistatic Tests

In this research, a screw-driven Hounsfield testing machine was used to deform specimens in compression and tension at nominal strain rates of approximately $\pm\dot{\varepsilon}$=10^{-3}-10^{-1} s^{-1}. 500 N, 10 kN and 100 kN load cells were used to test the specimens at different loading conditions. The compression tests were performed at nominal strain rates of 10^{-3}, 10^{-2} and 10^{-1} s^{-1} and the tensile and shear tests were done at a nominal strain rate of 10^{-3} and 10^{-2} s^{-1}. The screw-driven Hounsfield machine consists of a drive mechanism which is capable of imparting a controlled velocity to a movable crosshead with respect to a stationary head. The testing was carried out at standard laboratory temperature (23$\pm$3°C). The force in the specimen was measured using a load-cell that output a voltage proportional to the load by means of strain gauges that respond to the linear elastic deformation of the crosshead. In its most simple form, the strain in the specimen, ε, is calculated as the ratio of the displacement of the moving cross-head, u_c, to the initial length of the gauge section, l_0. However, where possible, crosshead displacement was not used for strain calculations and local displacements were measured directly off or as close to the specimen as possible, to avoid inaccuracies introduced by machine compliance. This method of measurement was carried out using a Laser Extensometer machine (FIEDLER Optoelektronik, model P-50, resolution 0.1μm). Figure 3-5 shows the experimental setup of a quasistatic test on the Hounsfield machine. For the compression tests, white stripes were painted on

the loading platens as close as possible to the gauge surface (measuring 9mm in diameter and 4mm thickness) of the specimen. For the tensile tests, white stripes were placed directly on the specimen gauge area (measuring 9mm in width and 36 mm in length), and for the shear tests white stripes were placed on the loading plates, on either side of the core.

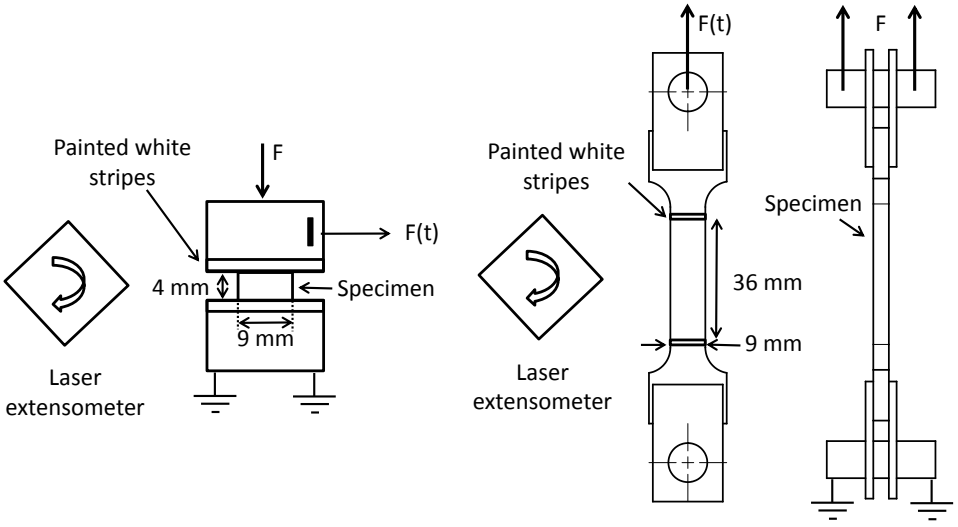


Figure 3-5: Schematic of the quasistatic compression (left) and tension (right) test set-up, with the laser extensometer recording the positions of painted stripes.

The laser, which deflects a laser beam onto the surface of the specimen using a rotating prism, illuminates the specimen surface, receives and tracks the reflections from these stripes, and eventually converts it to an electrical signal. A time history of the distance between the two stripes relative to an arbitrary datum point and the change in this distance throughout the duration of the test was recorded by the laser. These measurements allow for the calculation of a single strain value for the whole gauge length. The force readings from the Hounsfield machine, combined with the laser extensometer recordings were used to calculate the resulting uniaxial stresses and strains within the chosen gauge section. In order to observe the collapse of the cell

walls during the compression tests, and as a supplement to the laser extensometer for strain measurements, a camera (model teli-CMOS, resolution 4 mega pixels, 1 frame per second) was used. The use of photography based methods allows for a full field displacement analysis by measuring the strain very close, or directly on the specimen gauge section. Illumination was provided by LED lights surrounding the camera, which was fitted with blue filters to ensure the laser detector did not suffer any interference from the white camera light.

3.2.2 Medium Rate Experiments

The medium rate tests were carried out using an in-house servo-hydraulic machine, fitted with a resistive load cell. In this test rig, specimens that sit between the piston and a fixed cross-head can be loaded in compression or tension. The nominal strain rates achieved are generally in the approximate region of $\pm\dot{\varepsilon}=10^{-1}$–$10^{2}$ s^{-1}, although repeatable strain rates above 10 s^{-1} are difficult to obtain due to the limitations of the valve to consistently control the high speed flow required.

Similar to the quasistatic tests, the load was measured via a load cell attached to the test machine, which output a voltage proportional to the load by means of strain gauges. Prior to each series of testing the load cells were calibrated to ensure accurate calibration factors were used to convert voltage readings to force measurements. Linear Voltage Displacement Transducers (LVDT) are one of the most basic displacement measurement devices used for medium rate testing. However, this method does not directly measure the strain at the specimen gauge section, but includes compliance of all additional

systems (specimen shoulders, end caps et.), often resulting in strain measurements being over predicted. As the foam material investigated in this study is relatively weak and deformation is high, the compliance effect was measured and deemed negligible. However, for more accurate strain measurements the specimen displacement was also captured via a high speed camera (model PHANTOM VII, resolution dependent on frame rate, up to 100,000 frames per second), capable of directly monitoring the displacement by tracking the loading platens on either side of the specimen, which allowed for the calculation of a single strain value for the whole gauge length. Further information regarding the basic method applied in this research to evaluate strain from pictures is discussed in section 3.3.

3.2.3 High Rate Experiments

The conventional method of measuring the mechanical properties of materials over a range of strain rates between 10^2 and 10^5 s^{-1} is the Split-Hopkinson Pressure Bar (SHPB). This typically consists of two slender rods between which the specimen is placed (the input and output bars). A gas gun is used to project a third rod of the same material and diameter into the end of the input bar. This generates an elastic wave that travels down the bar to the specimen bar interface, where it causes the specimen to be compressed. Because of the impedance mismatch between the bar and the specimen, some of the stress wave is transmitted through the specimen, whilst some is reflected back into the input bar. By measuring the waves in the input and output bars, using surface strain gauges, a standard analysis may be used to calculate the

stress and strain in the specimen as functions of time. A more detailed description is provided in (Gray III, 1999).

For dynamic testing of soft, low impedance materials, such as polymers, rubbers and foams, the impedance mismatch between the bar material and the specimen should be kept small, so as to increase the signal-to-noise level (Gray III 1999; W. Chen et al. 2002; Chen et al. 1999). Visco-elastic bars have often been used to test soft low-impedance materials, however, analysis of the experiments is made more complicated by dispersion and attenuation effects, and the pronounced effect of temperature on the elastic properties of the visco-elastic bars (Gray III, 1999). The signal-to-noise ratio can also be increased by using hollow tubular bars. Chen *et al.* (1999) investigated the dynamic stress-strain response of a silicon rubber material using a high-strength aluminium alloy bar, and a hollow transmission bar, as part of a SHPB system. The use of the aluminium alloy bar meant that dispersion and attenuation effects were negligible (unlike visco-elastic materials) and the lower Young's modulus and reduced cross-sectional area ratio led to an increased amplitude of the transmitted strain signal. This system was effectively used to measure the dynamic mechanical response of soft materials.

In this study, to ensure the bar material was more sensitive to stress measurements and capable of measuring smaller strain values a new SHPB apparatus was set up using low modulus (~ 46 GPa) magnesium AZM alloy bars. Magnesium alloy bars are preferred to polymer bars to avoid complications of dispersion and attenuation of the stress waves as they

propagate along the bar (Bacon 1999; Shergold et al. 2006; Siviour et al. 2008; Tagarielli et al. 2008).

The input bar was 12.7 mm in diameter and 1000 mm long, and instrumented with a foil strain gauge halfway along its length. The output bar was also 12.7 mm in diameter but only 500 mm long, and it was instrumented with a foil strain gauge 50 mm from the specimen. Figure 3-6 shows a schematic of the SHPB apparatus employed in this study.

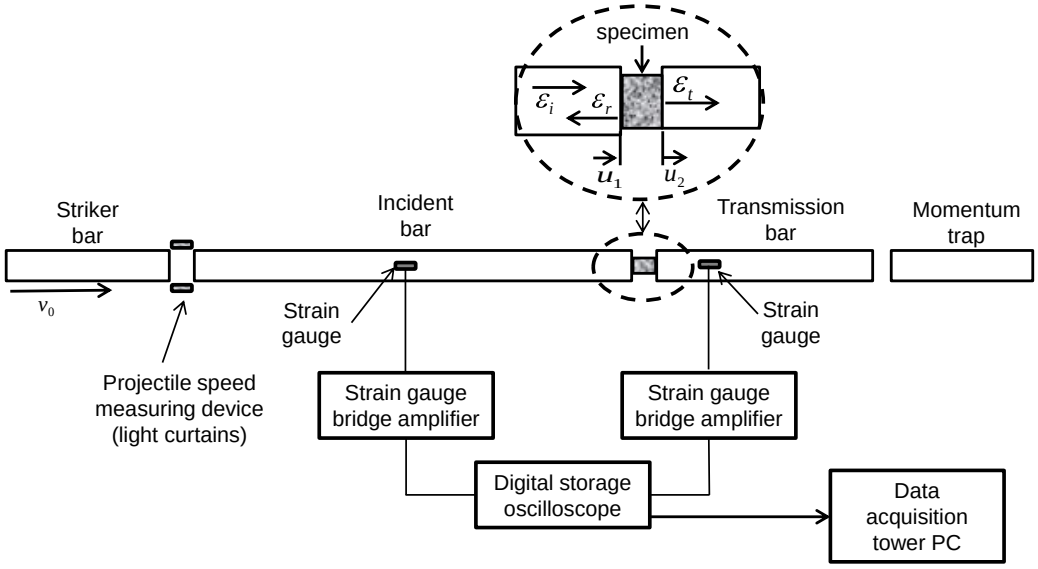


Figure 3-6: A simple schematic of the SHPB apparatus used in this study

The strain gauges were calibrated statically and dynamically, to provide a system calibration with an accuracy of better than 0.5%. The 0.5 m striker bar was set to a velocity range of 2 to 15 m s^{-1}, with the upper limit defined in such a way, to ensure the magnesium alloy bar does not yield during the test. It is assumed the waves travelling through the bars can be described using the one-dimensional wave propagation theory analysis (Kolsky, 1949; Gray III, 1999). By using sample sizes that minimise the area miss-match between the sample and the bar diameter, and by lubricating the ends of the specimens and using

long narrow bars, errors due to radial and longitudinal inertia, as well as friction effects were reduced substantially (Siviour, 2005; Kuhn, 2000). Figure 3-7 shows a picture of the general SHPB set-up used in this study.

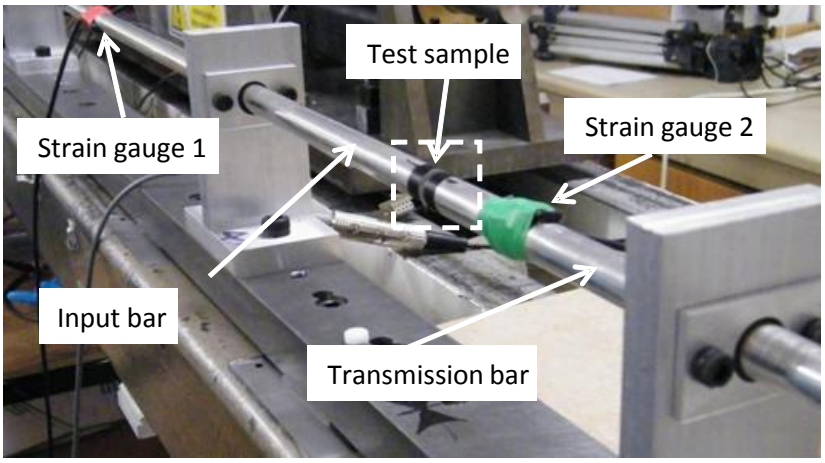


Figure 3-7: SHPB for high strain rate testing

The determination of the stress-strain behaviour of a material being tested in the Hopkinson bar, is based on the one-dimensional elastic-wave propagation theory (Gray III, 1999). According to this theory, the axial displacement $u(t)$ at a given time (see insert of Figure 3-6) is related to the axial strain history $\varepsilon(t)$ using the following equation;

$$u(t) = c_s \int_0^t \varepsilon(t)dt, \qquad [3\text{-}1]$$

where c_s is the longitudinal wave propagation speed calculated as 5098 m s^{-1} using the Elastic Young's modulus of the AZM bar E, and the bar material density ρ.

$$c_s = \sqrt{\frac{E}{\rho}} = 5098\ m\ s^{-1}. \qquad [3\text{-}2]$$

Therefore, the axial displacement at the input bar/specimen interface and the output bar/specimen interface can be calculated as shown below;

$$u_1 = c_s \int_0^t (\varepsilon_i - \varepsilon_r) dt \qquad [3\text{-}3]$$

and

$$u_2 = c_s \int_0^t \varepsilon_t dt \qquad [3\text{-}4]$$

The nominal compressive strain can hence, be calculated as

$$\varepsilon_s(t) = \frac{u_1 - u_2}{L_s} = \frac{c_s}{L_s} \int_0^t (\varepsilon_i - \varepsilon_r - \varepsilon_t) dt, \qquad [3\text{-}5]$$

where L_s is the initial length of the specimen.

The input force F_1 and output force F_2 on the incident/specimen and output/specimen interface is given as

$$F_1 = EA_b(\varepsilon_i + \varepsilon_r) \qquad [3\text{-}6]$$

and

$$F_2 = EA_b\varepsilon_t, \qquad [3\text{-}7]$$

respectively, where A_b is the cross sectional area of both bars.

Mechanical equilibrium is an important factor, which must be considered when carrying out SHPB tests (Gray III, 1999). In order for a specimen to be in mechanical equilibrium, the force amplitude on the front and rear face of the specimen must be the same. However, this does not occur concurrently, as it takes a finite time for the stress wave to travel through the specimen. This is usually achieved after a few oscillations of the stress wave through the specimen, and using thin short specimens can reduce the time it takes to achieve dynamic equilibrium. If force equilibrium is achieved $\varepsilon_t \approx \varepsilon_i + \varepsilon_r$, and Equation [3-5] simplifies to

$$\varepsilon_s = -\frac{2c_s}{L_s}\int_0^t \varepsilon_r dt, \qquad [3\text{-}8]$$

and the strain rate can be calculated as

$$\dot{\varepsilon}_s = \frac{d\varepsilon_s}{dt} = -\frac{2c_s}{L_s}\varepsilon_r, \qquad [3\text{-}9]$$

and the nominal compressive stress in the specimen is calculated as

$$\sigma(t) = \frac{A_b}{A_s} E_b \varepsilon_t(t), \qquad [3\text{-}10]$$

where A_s is the cross sectional area of the specimen.

In addition to the analytical methods discussed above, photography based methods can also be used to not only measure strain, but to also ensure the material has deformed in a uniform manner. Furthermore, the use of these methods allows for recording failure modes and damage evolution within the specimen. The high speed camera used for the high strain rate tests conducted in this study was a Specialised Imaging SIM16 model (16 frames, resolution 1 mega pixel, up to 200 million frames per second, used frame rate typically 300,000 frames per second).

3.3 Strain Measurements using Photography Based Methods

The use of image analysis methods as an alternative tool for full field strain measurements is highly invaluable. In the tests where white stripes are placed close to the gauge section, images are taken during the tests, and similar to the laser extensometer method the movement of the white stripes is closely tracked, this time using an in-house Matlab software (Jumpasut et al., 2008) developed at the University of Oxford. Furthermore, an optical technique often referred to as Speckle Metrology can also be used, where displacement is measured by tracking the motion of a random pattern on the specimen surface (Siviour et al. 2009). This technique can be used to measure the deformation fields within an inhomogeneous specimen, such as a cellular material with a random distribution of cells. A sequence of images taken during an experiment can be used to obtain accurate, quantitative, full-field measurements of the displacement fields in the deforming specimen. Prior to each experiment, reference images of the un-deformed test sample are taken. The speckle analysis can be used to track the displacement of a grid of sub-images between the reference and each deformed image, to give an array of x- (which can be used to measure Poisson's ratio) and y-displacements (to measure specimen strain) across the specimen surface. An example of this is shown in Figure 3-8 where images taken during a medium rate test on R200 were used to measure strain in the axial and transverse directions. By using cine film software tools, the number of pixels versus images plot in Figure 3-8, taken from the Phantom

camera measurements, can be converted to a displacement-time plot. The slope of the graph provides a measure of the specimen strain, which enables the user to not only determine the Poisson effect (using the x-displacement measurement, which in this case shows negligible Poisson effect for R200), but also confirms if the strain is constant along the gauge length, hence, providing the ability to determine whether mechanical equilibrium has been achieved in the specimen prior to failure.

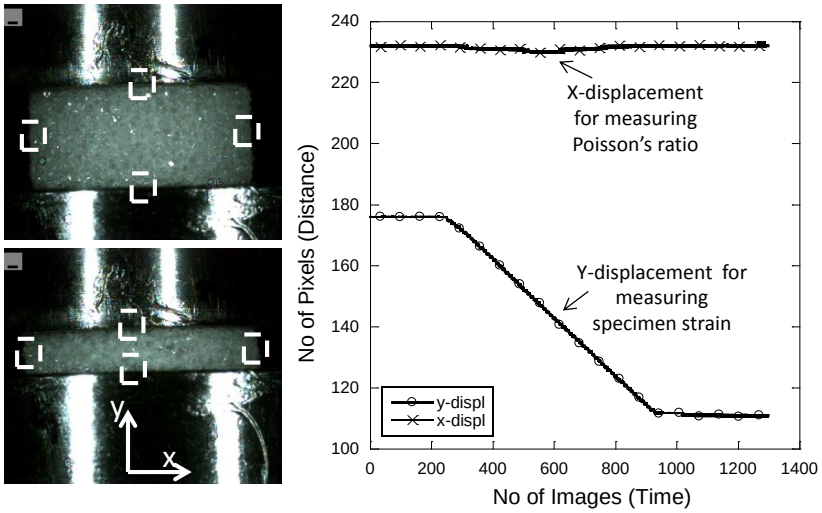


Figure 3-8: The use of photography-based methods to measure specimen strain in the x and y directions, respectively.

By combining these measurements (for compressive strain) with strain gauge measurements (in the case of the SHPB system for specimen force) or load-cell force readings (for the quasitatic and medium rate tests), the compressive stress-strain curve for each specimen can be obtained. Further details about the application of speckle metrology including image acquisition, analysis and accuracy, are given in (Siviour et al. 2009; Siviour & Grantham 2009). In most cases, the speckle pattern is manually applied to the surface of the specimen; however, for the experiments presented here, the natural

inhomogeneous surface of the foam was deemed suitable for the speckle pattern.

3.4 Compression Tests at Different Temperatures

Uniaxial quasistatic compression tests were conducted on cuboidal specimens measuring $15 \times 15 \times 10$ mm placed within an environmental chamber. Liquid nitrogen was used to create a cold environment inside the chamber, whilst an integrated oven, was used for high temperatures. The liquid nitrogen, which was kept within a metallic vessel, was connected to the temperature chamber via a hose line with an adjustable nozzle. This connection was used to manually adjust the flow rate and thus maintain the temperature within the chamber. The temperature inside the chamber was monitored using a thermocouple embedded onto the loading platens as close to the specimen as possible. Testing commenced when the specimen and the platens were in thermal equilibrium.

In this study, the quasistatic compressive behaviour of Rohacell foam of different densities was measured for a number of temperatures: ranging from -70, -40, -10, +5, +23, +70 and +200°C. The load was applied via a screw-driven Instron machine controlled and run by Instron BlueHill software, and measured with a resistive load cell of 5 kN. Compressive strains were measured using an extensometer, which was directly fitted onto grooves surrounding the flat compression platens, positioned on each side of the specimen. The specimens were loaded at a nominal strain rate of 10^{-2} s^{-1}. In all test cases, to minimise friction, the platens were lubricated with petroleum jelly (A. Trautmann et al., 2005); however, at extreme low temperatures (-70 °C), the lubricant was removed due to freezing problems. At these low temperatures, to avoid rig parts locking up due to frozen parts, the rig components were

manually traversed up and down in a free manner as the temperature in the chamber dropped. This ensured smooth displacement during the tests, and removed the high friction effects caused by frozen rig parts.

3.5 Environmental Scanning Electron Microscopy

Conventional Scanning Electron Microscopy (SEM) was developed in the early 1950's, allowing researchers to examine much larger variety of specimens using high resolution and an exceptionally large depth of field (Donald, 2003). SEM is a microscope that uses the interaction between a beam of electrons and the sample to form an image. Because the electron source must be held in a vacuum, traditional SEM is performed using an evacuated column and sample chamber. In addition, this reduces scattering of the electron beam, which enables a high quality, high resolution image. However, in order to prevent the build-up of charge on the specimens, specimens must either be electrically conductive, or provided with a thin conductive coating. A sub-micrometre thick layer of gold is typically used.

Environmental Scanning Electron Microscopy (ESEM) on the other hand is based on the use of a multiple aperture graduated vacuum system, allowing the specimen chamber to be under water vapour, or other auxiliary gases at a higher pressure. A schematic of the ESEM set-up is shown in Figure 3-9, taken from (Dragnevski, 2012). This allows non-conducting specimens to be imaged, because the gas provides the required conducting path. In this system the electrons emitted from the specimen have to travel to the detector through the gas-containing chamber, and hence undergo collisions with gas molecules. Subsequently, the build-up of charge associated with electron microscopy of insulators is neutralised through the formation of positive ions which are the result from the reaction between the electrons and the gas molecules. These tend to drift back to the surface of the specimen and create a protective layer

that neutralises the usual build-up of electrons. This means samples can be imaged in their “natural state” without the need of coating.

The ESEM chamber is generally held at pressures between 1 Torr and 10 Torr, whilst the gun and column remain at pressures of ~7.5x10^{-7} Torr.

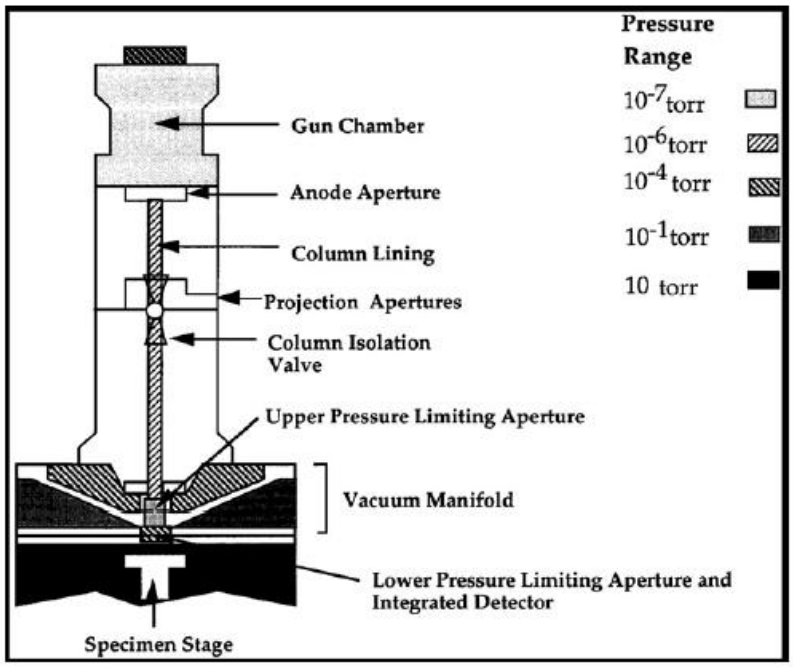


Figure 3-9: Schematic diagram of the ESEM column identifying differerent pressure zones. Taken with permission from (Dragnevski, 2012).

3.5.1 In-situ Mechanical Testing

In-situ mechanical testing in the ESEM is a well-established technique, which not only enables the user to measure the mechanical properties of the material under investigation, but also enables a step by step observation of the microstructural and fracture development of the material upon loading or unloading.

In order to explore the differences in the compressive deformation mechanisms between low- and high-density foams, in-situ compression tests

were performed in the ESEM. A loading stage of capacity 5 kN was employed to compress cubic specimens of 5 mm side between two flat plates. The test specimens were cut using a diamond-grit miniature disk saw, which minimised surface damage to the specimens. The specimen was clamped between two jaws that were driven apart by a motor connected to a lead screw through a step down gearbox (see Figure 3-10). The tests were occasionally interrupted in order to take high resolution images. The 5 kN load cell was used to record the output load, whilst the specimen displacement was also measured by the use of a Linear Voltage Displacement Transducer (LVDT).

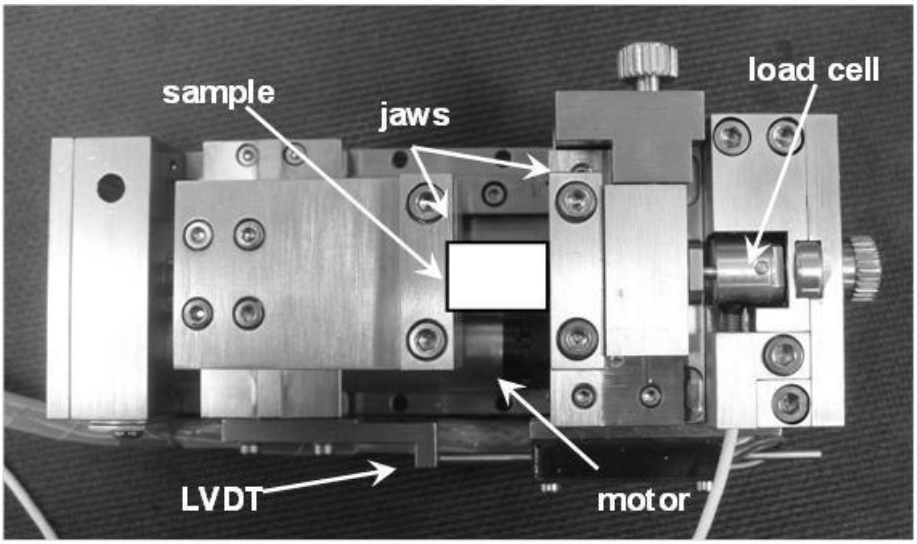


Figure 3-10: Illustrating a tensile/compression miniature stage of an ESEM machine. Taken with permission from (Dragnevski, 2012)

Chapter 4

Quasistatic Response at Different Length Scales

In this chapter the quasi-static mechanical response of Polymethacrylimide (PMI) foams of densities ranging from 50 to 200 kg m^{-3} is investigated, in order to provide experimental data to inform and validate numerical constitutive models for the response of polymer foams. The macroscopic mechanical response is characterised by conducting quasi-static compression, tension and shear experiments. Indentation experiments are performed to explore the response of the foams to a multi-axial state of stress, and finally, microscopic deformation mechanisms are identified by conducting in-situ SEM observations during static compression and tension tests. The aim of this work is to generate novel understanding on the behaviour of cellular materials. The research presented in this chapter has been published in Arezoo et. al (2011).

4.1 Experimental Results

All tests were repeated three to five times in order to quantify and reduce the effects of experimental scatter, which can be caused due to a variation in material microstructure or specimen geometry. During the machining and preparation of specimens, due care was taken to avoid applying thermal loading or residual stresses. As the volume of the foam material is not conserved during the experiments, unless otherwise stated, all stress-strain curves measured from the experiments represent engineering (nominal) stress-strain values. The measured stress versus strain response was highly repeatable, with scatter below 5%. For clarity, in most figures only one test curve is presented and scatter (mean ± standard error) is reported elsewhere.

4.1.1 Foam Isotropy

The manufacturers of Rohacell state that the material is isotropic. This is supported by the work of Li *et al.* (2000) who tested Rohacell 51WF in three mutually perpendicular directions, and reported compressive stress-strain curves of similar profiles and magnitudes in all three directions. To confirm this, for all the given foam densities similar experiments were conducted on R71, R110 and R200 and the resulting stress strain curves were compared. An example of these curves for two foam densities is shown in Figure 4-1. The curves clearly show the typical nearly linear elastic region, followed by the stress plateau region and the steep rise in the densification region. The stress-strain curves show similar mechanical behaviour in all three directions, defined

as x, y (in-plane directions) and z (out-of-plane direction), suggesting isotropic foam behaviour.

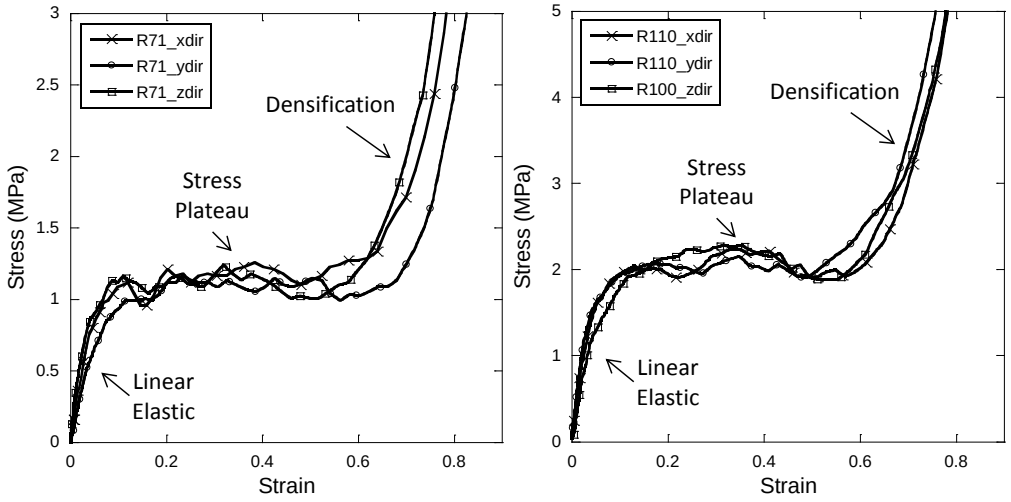


Figure 4-1: Comparison of the compressive behaviour of R71 and R110 (T=23°C, $\dot{\varepsilon} = 10^{-3}\,s^{-1}$), when tested in three mutually perpendicular directions.

4.1.2 Quasistatic Compression Test Results

Typical stress-strain compressive responses for all four foam densities, tested at a nominal strain rate of 0.001 s^{-1} are shown in Figure 4-2. The foam response comprised a linear phase followed by a stress plateau characterised by negligible strain-hardening, and final densification. As discussed in Chapter 3, strain measurements using photography-based methods revealed that negligible lateral strain was observed, implying that for these foams the plastic Poisson's ratio is close to zero. The compressive Young's modulus was measured upon elastic unloading at a plastic compressive strain of approximately 0.05, in order to obtain measurements independent of specimen surface finish or slight misalignment of the compression platens. This procedure is also in line with recommendations by Ashby *et al*. (2000) who investigated the loading and unloading behaviour of an aluminium foam and noticed that the

slope of the initial loading portion of the stress-strain curve was lower than that of the unloading curve. Their investigations suggested the reduced slope was due to localised plasticity in the specimen, at stresses well below the compressive strength of the foam. As a result, they recommend the Elastic Young's modulus measurements should be made from the slope of the unloading curve

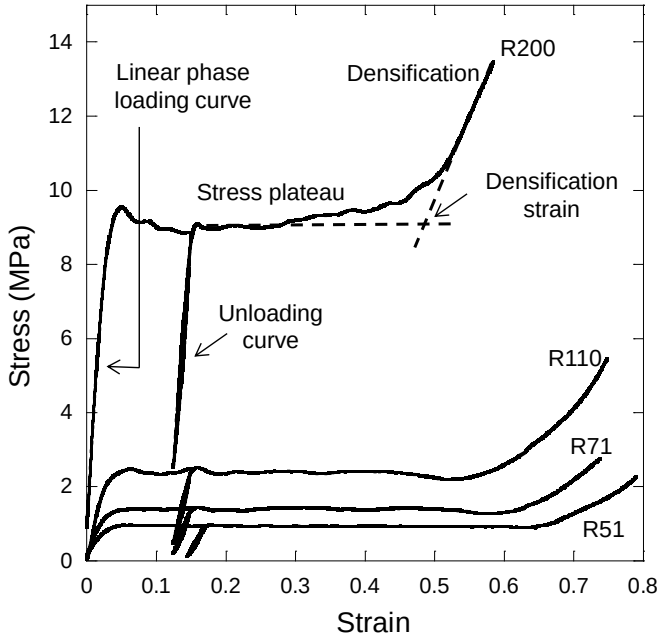


Figure 4-2: Compressive loading and unloading behaviour of Rohacell foam (T=23°C, $\dot{\varepsilon} = 10^{-3}\ s^{-1}$), in four foam densities.

Measured mechanical properties are summarised in Table 4-1 for all foam densities (includes mean ± standard error), where values of the measured compressive plateau stress σ_{pl}, compressive yield stress σ_{Yc} (defined as the flow stress at a nominal plastic strain of 0.2%) and densification strain ε_D (defined as the intersection of the tangents to the stress plateau regime and the densification regime) are given.

Material	E_c (MPa)	E_t (MPa)	G (MPa)	σ_{Yc} (MPa)	σ_{pl} (MPa)	ε_D	σ_{Yt} (MPa)	σ_{Ft} (MPa)	τ_Y (MPa)	τ_F (MPa)
R51	32.1±0.3	72.7±0.9	15±0.7	0.93±0.02	0.9±0.04	0.76±0.03	1.2±0.06	1.42±0.02	0.5±0.05	0.8±0.04
R71	47.1±1.2	100.3±0.2	29±1.1	1.4±0.01	1.39±0.3	0.68±0.04	1.6±0.04	1.77±0.03	0.8±0.07	1±0.03
R110	83.3±0.9	132±2.9	41±2.3	2.5±0.03	2.4±0.08	0.68±0.01	2±0.03	2.2±0.06	1.3±0.04	1.2±0.06
R200	253.8±6.5	375.3±6.8	164±5.5	10±0.14	9±0.3	0.65±0.04	6±0.23	7.8±0.3	3.6±0.17	5±0.43

Table 4-1: Measured uniaxial quasistatic mechanical properties of Rohacell foam.

4.1.3 Quasistatic Tensile Test Results

Figure 4-3 shows the tensile test results of all four Rohacell foam densities at a nominal strain rate of 0.001 s^{-1}.

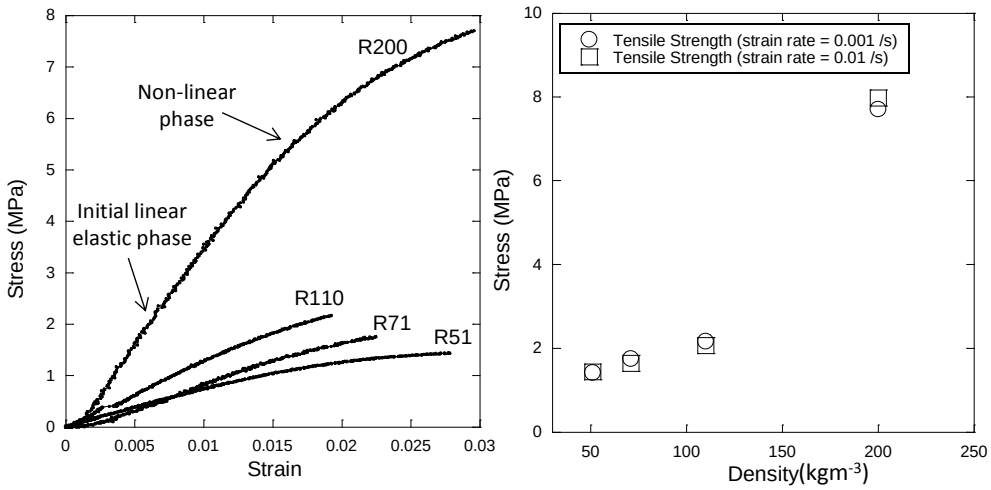


Figure 4-3: Tensile test stress-strain results (T=23°C, $\dot{\varepsilon} = 10^{-3}\ s^{-1}$), and strain rate dependency of tensile strength.

The strain rate dependency of the material under quasistatic tensile loading was investigated by repeating the tests at a strain rate of 0.01 s^{-1}. The results demonstrate a negligible strain rate dependency of the tensile strength results. Similar trends were observed for the compressive strength of the

material, when tested at three distinct quasistatic strain rates, which are further discussed in Chapter 5 of this thesis.

In Figure 4-3 (left image), for all the densities, the response comprised an initial linear elastic phase followed by a non-linear phase of pronounced strain-softening. Brittle failure occurred at nominal strains of 2-3% by the propagation of a crack perpendicular to the loading direction. Table 4-1 includes the measured tensile elastic modulus E_t , tensile failure stress σ_{Ft} and tensile yield stress σ_{Yt} for all foams; again, the yield stress in tension is defined as the tensile flow stress at a plastic nominal strain of 0.2%.

The brittle behaviour observed in Figure 4-3 is commonly seen in most rigid polymer foams (Gibson & Ashby 1999). The non-linear behaviour of the stress-strain curve seen in compression is caused by buckling of the cell walls, which leads to progressive collapse, giving a long horizontal stress plateau. Thus one would expect an increase in strength with increasing density, as the thicker cell walls buckle less early. In tension, however, the cell edges, which initially lie at an angle to the tensile axis, now rotate and stretch towards this axis, giving rise to structure stiffness. Failure then occurs by cracks forming within the solid cell wall material, which propagate in a fast manner leading to brittle failure in tension. These changes in geometry usually cause the material to be stronger in tension than compression and this appears to be the case for the low density Rohacell foam (R51 and R71). However, with increased relative density, the foam material is observed to be stronger in compression than tension. The measured elastic response also demonstrates the material exhibiting a greater tensile modulus than the compressive modulus, especially

for foams of low density. As a result, both the elastic and plastic macroscopic response of the foam displays a tension/compression asymmetry (see Figure 4-4 as an example for yield stress values).

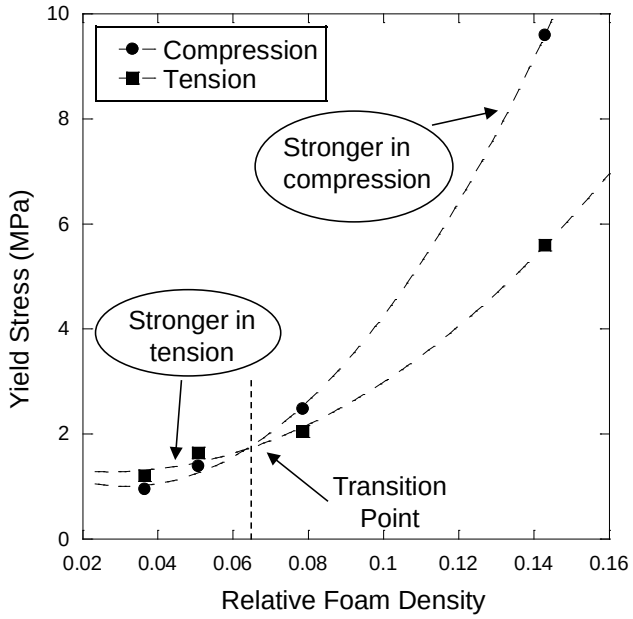


Figure 4-4: Tension/compression asymmetry of measured yield stress vs. relative foam density (T=23°C, $\dot{\varepsilon} = 10^{-3}\, s^{-1}$).

Although, some conjectures have been made regarding this tension/compression asymmetry, the literature is yet to provide supporting evidence for the observed behaviour. A novel opportunity exists to investigate this behaviour with the aid of in-situ compression and tensile experiments.

4.1.4 Quasistatic Shear Test Results

Single-lap shear experiments were conducted using prismatic foam specimens with an I-shaped cross-section, with shear deformation occurring in the web of the I-beam. The I-beam was sandwiched between two steel plates and bonded to these by a structural adhesive; the plates were connected to a screw-driven test machine by pin-joints.

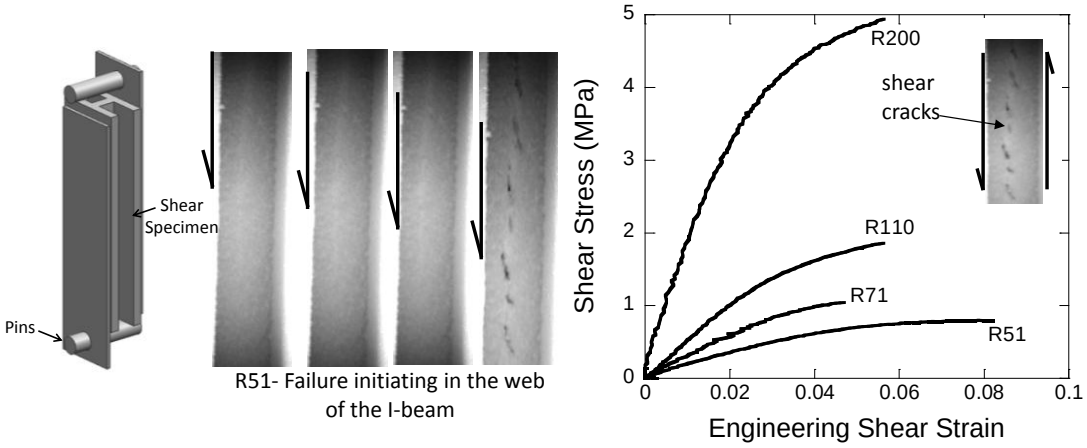


Figure 4-5: Shear stress-strain plots (T=23°C, $\dot{\varepsilon} = 10^{-3}\, s^{-1}$) of all four Rohacell foam densities investigated (shown on right), and an example of R51 failing under shear load (shown on left).

During the experiment the test machine reduced the spacing between the pin-joints, therefore applying a compressive force on the steel fixture, resulting in a shear action on the I-shaped foam core. Initially, the tension version of the shear test was experimented; however, failure occurred along the load line, invalidating the test. Therefore, the compressive version of the test was used. A non-contact laser extensometer of resolution 1µm and gauge length 10 mm was employed to record the relative displacement between the two flanges of the I-beam, thereby determining the engineering shear strain.

The measured stress-strain responses in shear for the four foams are reported in Figure 4-5. Unlike the compressive response, the shear response of the foam does not include the long plateau region, followed by densification. They comprise a linear elastic regime, followed by a nonlinear phase. It appears that the foam is fairly brittle, showing little crushing after failure. However, a small amount of ductile behaviour is seen just before failure, indicating plastic deformation. To identify the transition of elastic to plastic behaviour in the foam material, a method similar to that used in tensile tests to identify the yield

strength was used, i.e. a 0.2% offset strain was defined. The shear stress was determined by finding the intersection of the stress-strain curve with a line parallel to the initial slope of the curve which intercepts the abscissa at 0.2% strain. From this intersection point onwards the shear stress and strains correspond to a plastic deformation. Failure was by formation of shear micro-cracks in the central portion of the web, as seen in Figure 4-5. Table 4-1 lists values for the shear modulus G, the stress at failure τ_F and the shear yield stress τ_Y (defined as the shear flow stress at a plastic engineering shear strain of 0.2%) for the four foam densities. The measured values were in line with those reported by material data-sheets (Evonik Industries 2011) and in existing literature (Zenkert & Burman, 2009).

4.1.5 Indentation Experiments

When cellular materials are used in critical load-bearing applications, their response to multi-axial stresses becomes important. Engineers, who design lightweight sandwich structures, require precise information about the way in which the cellular material will behave under biaxial or tri-axial loading. In this study, in order to explore the response of the foams to a tri-axial state of stress, indentation tests were performed on the foam material. The results from these simple tests were also used for material model validation, as they encompassed compression, shear and tensile loading.

The indentation tests were performed using a steel ball bearing of radius 12.5 mm, which was forced to indent, at constant speed, blocks of foams of various foam densities (ranging from 51 to 210 kg m^{-3}), with dimensions $120 \times 120 \times 50$ mm. The tests were performed using an in-house Hounsfield machine under a displacement control at a nominal constant loading rate of approximately 3 mm min^{--1}. The indentation load was applied through the steel spherical indenter. The indentation speed was chosen to give an average strain rate of 0.01 s^{-1} at an indentation depth of 10 mm (the average strain rate can be calculated as $\dot{\varepsilon} = \frac{\dot{h}}{h}$, as defined in equation [4-1], where h is the indentation depth and the dot denotes differentiation with respect to time).

$$\dot{\varepsilon} = \frac{d\varepsilon}{dt} = \frac{\Delta h / h}{dt} = \frac{\Delta h}{dt.h} = \frac{\dot{h}}{h} \qquad [4\text{-}1]$$

The load was measured via the 10 kN in-house screw driven Hounsfield testing machine. The laser extensometer was used to measure the

displacement of a white stripe positioned on the loading anvil as it displaced the ball into the foam material, relative to a white stripe positioned on a static rigid holder, placed directly above the indenter (see Figure 4-6).

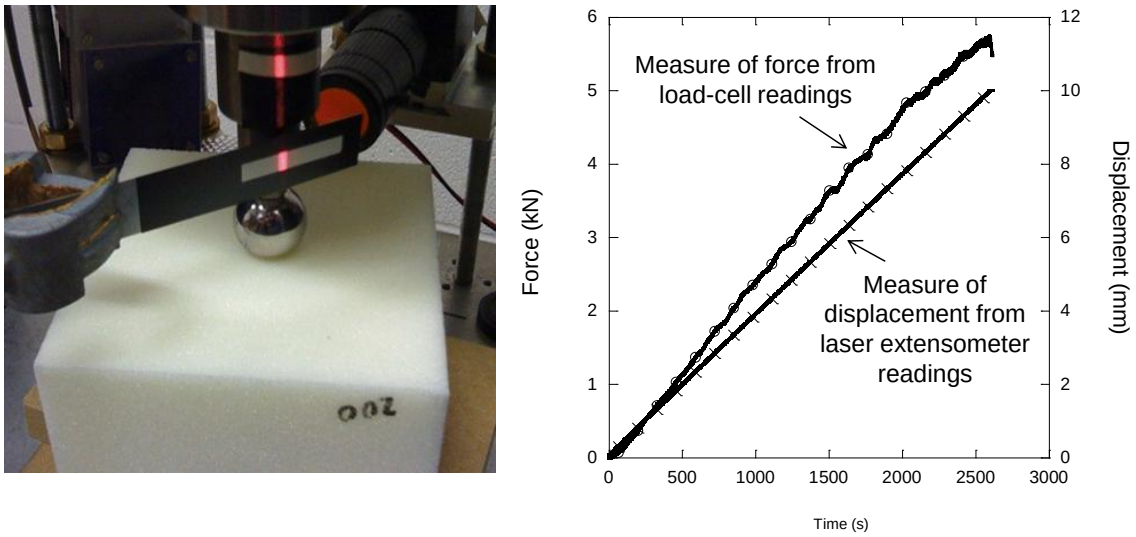


Figure 4-6: Indentation test apparatus, using laser extensometer and white stripes positioned close to the ball indenter to measure displacement, and load-cell readings to measure indentation force.

The measured indentation force versus displacement curves are presented in Figure 4-7. The load increased linearly with displacement up to an indentation depth of approximately 7 mm. At this depth, brittle cracking of the foam occurred for all densities, and the ensuing load/displacement response became non-linear. Observations subsequent to the tests confirmed that the foam had undergone fracture under the indenter.

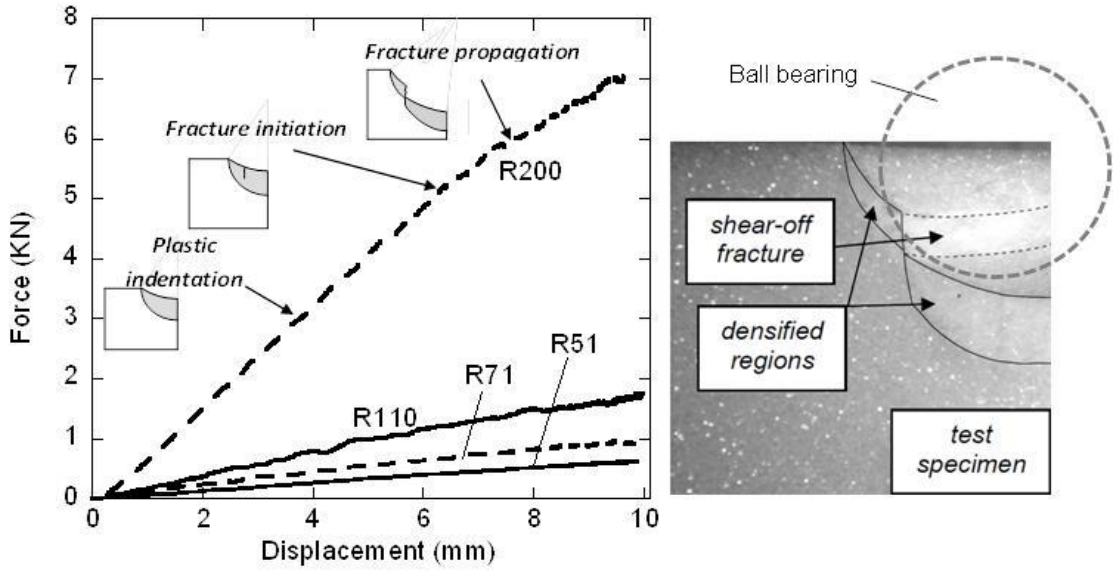


Figure 4-7: Measured indentation force versus displacement response for the four foam densities. An illustration of the indentation test is shown on the right.

The measured indentation response and microscope observation of the indentation specimens revealed that fracture occurred at similar indentation depths (and therefore at similar strains) for all foams investigated. Cracks were also seen to initiate in the region of densified foam under the indenter. In this region, the foam has acquired a locally anisotropic response due to strain-induced changes in its microstructure. These results will be further discussed when used to validate existing Finite Element (FE) models in Chapter 7.

4.2 In-situ Compression and Tension Experiments

Figure 4-8 summarises the dependence of some stiffness and strength parameters of Rohacell foams upon the foams relative density (the power-law fits through the experimental data shown in Figure 4-8 give the intercepts and exponents listed in Table 4-2). The figure shows that the yield stress is higher in tension than in compression for low-density foams, whereas the opposite is seen for high-density foams. This is in line with the findings of Zenkert *et. al* (2009), who justified this by conjecturing that elastic buckling mechanisms might intervene in the compressive deformation of low-density foams, thus, reducing the measured yield stress. The measured elastic response of the foam is asymmetric, with the materials tensile modulus greater than the compressive modulus, especially for foams of low density.

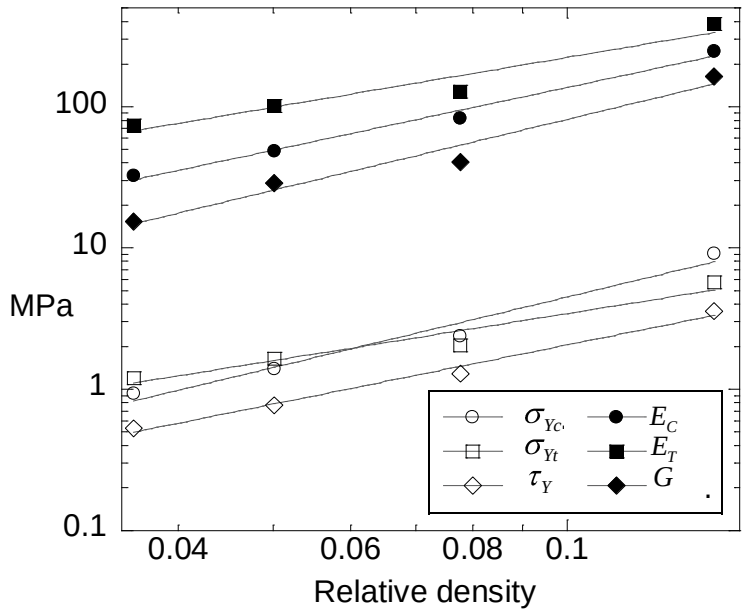


Figure 4-8: Scaling of elastic and plastic properties with the relative density of the foam (the scales of both axes are logarithmic, T=23°C and $\dot{\varepsilon} = 10^{-3}\ s^{-1}$). Average values are reported; the data scatter was less than 5% on all properties.

Several micromechanical models for the response of an idealised foam geometry (Chen & Lakes, 1995; Gibson & Ashby, 1999) predict equal stiffness and yield stresses in tension and compression, based on the assumption that cell-wall collapse in both uniaxial tension and compression is governed by a plastic cell-wall bending mechanism. On the other hand some authors (Deshpande & Fleck 2001) have recognised that low-density foams with slender cell-walls can collapse under a macroscopic compressive stress by elastic buckling of the cell-walls.

$Y = A\bar{\rho}^{b}$	A, (MPa)	b
σ_{Yc}	105	1.66
σ_{Yt}	44	1.11
τ_{Y}	51	1.39
E_{C}	4106	1.47
E_{T}	3333	1.17
G	3784	1.66

Table 4-2: Pre-factors (A) and exponents (b) for power-law fits of the experimental data shown in Figure 4-8

An Environmental Scanning Electron Microscope (ESEM) was employed to observe the details of the foams microstructure. Figure 4-9 shows four micrographs for the four foam densities investigated here. Figure 4-10 shows the depth of field and detail of geometry that can be achieved using an ESEM, by showing an example of a single R200 cell with an image of the cell wall edges shown on the right.

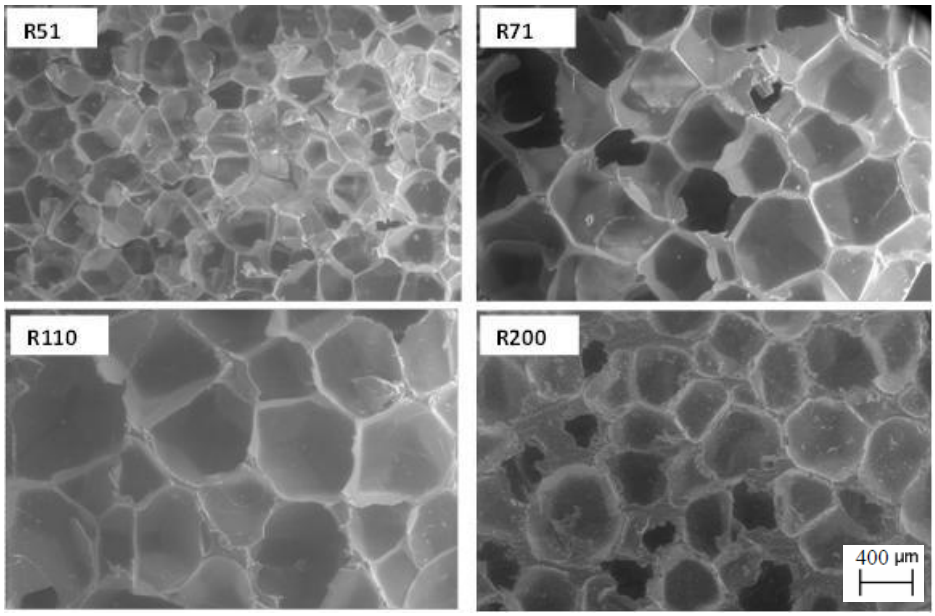


Figure 4-9: ESEM micrographs of the four foams investigated in this study, showing the variation of material microstructure with relative density.

The shape of the closed cells was similar to the idealised tetrakaidecahedral geometry, as recognised by other authors (Gibson & Ashby 1999; Chen & Lakes 1995).

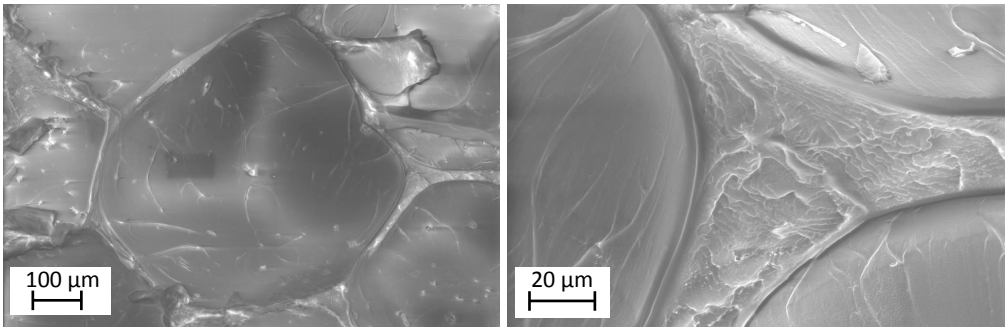


Figure 4-10: An example of a single R200 cell and the level of detail of the cell wall geometry shown on the right.

For this foam geometry, Gibson and Ashby (1999) have provided predictive formulae to obtain the relative density as a function of geometrical parameters. The average cell size, cell-wall length and thickness were measured from statistical analysis of the ESEM scans and results from these

measurements are presented in Table 4-3, which includes values of the slenderness ratio of the cell walls (measured as the ratio of the average edge length to the average cell wall thickness), as well as the measured and predicted relative densities. Gibson and Ashby's predictions are accurate for low density foams but under-predict the relative density of foams of higher density.

Density ($kg\ m^{-3}$)	Cell Diameter (μm)	Edge Length (μm)	Edge Thickness (μm)	Cell-Wall Slenderness Ratio	Measured Relative Density	Predicted Relative Density
51	380	230	7	36	0.04	0.03
71	960	510	17	30	0.05	0.04
110	930	580	14	40	0.08	0.03
200	640	350	28	12	0.14	0.1

Table 4-3: Measured average micro-structural paramters for the four foams under investigation, and predicted relative density according to Gibson and Ashby

In order to explore the differences in the compressive deformation mechanisms between low and high-density foams, in-situ compression tests were performed in the ESEM. A loading stage of capacity 5 kN was employed to compress cubic specimens of 5 mm side between two flat, lubricated plates. Test specimens were cut by using a diamond-grit miniature disk saw which minimised surface damage on the specimens. The tests were occasionally interrupted in order to take ESEM scans.

The in-situ compression tests revealed that plastic deformation of the foam was initially uniform, up to plastic compressive strains (ε^{pl}) of the order of 5%. Beyond this strain level, premature collapse of individual cells triggered localisation of deformation along bands perpendicular to the loading direction and of width of the order of the cell size. Such bands increased their length and

thickness with continued macroscopic compressive deformation, as is shown in Figure 4-11 for a R200 specimen. Some specimens collapsed by formation of multiple deformation bands and their final coalescence.

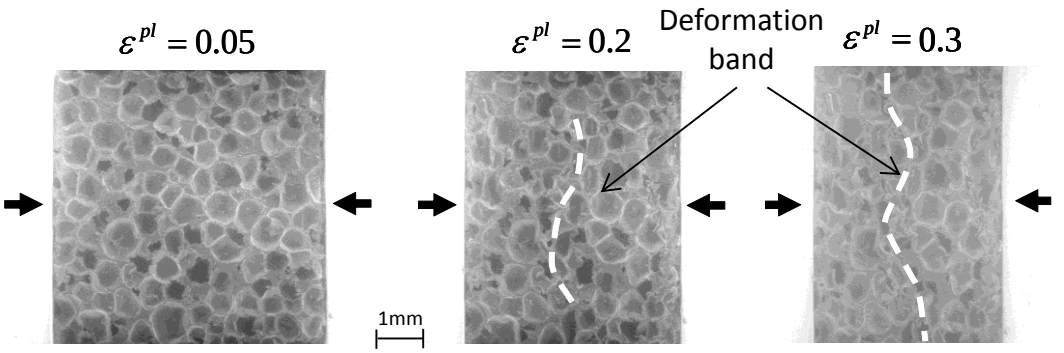


Figure 4-11: ESEM scans from an in-situ compression test on the R200 foam; uniform plastic deformation is followed by strain localisation initiated by plastic bending of the cell walls.

The mechanism by which individual cells collapsed was found to depend on the foam density. The left-hand side of Figure 4-12 shows a sequence of three ESEM scans of a R51 foam undergoing compression, in displacement control. The first frame shows the initiation of elastic buckling of an initially straight cell-wall upon compressive loading. As the load is increased further, the lateral deflection of the buckled edge increases and a crack develops in an adjacent cell-wall. The sample is then unloaded and the buckling deformation is partially recovered.

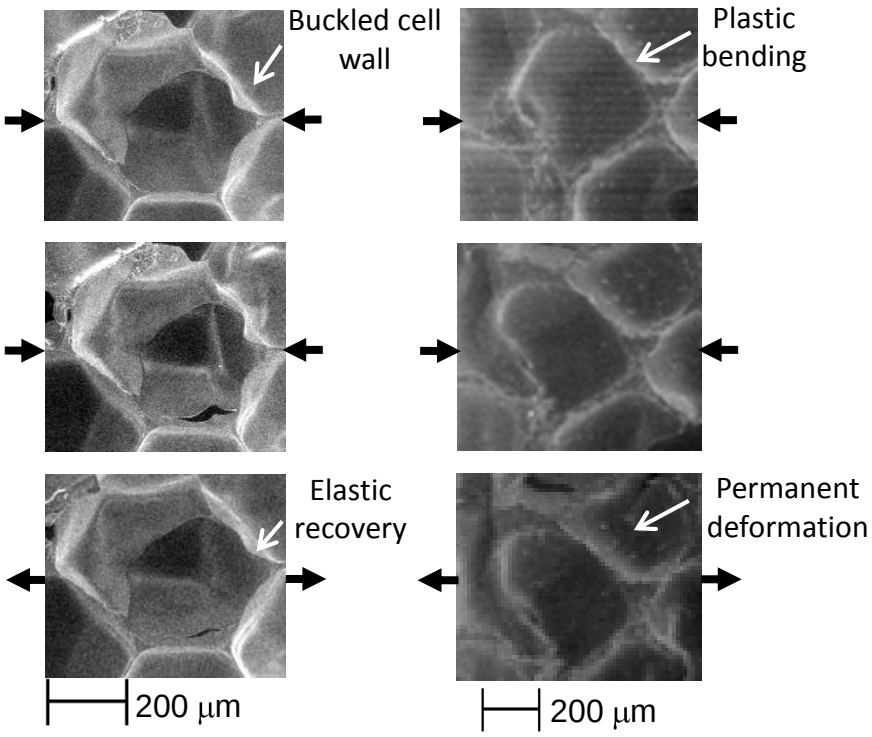


Figure 4-12 Left: ESEM scans from an in-situ compression test on the R51 foam, showing cell wall buckling followed by elastic unloading. Right: similar ESEM scans for foam R200, showing cell wall plastic bending, with permanent deformation upon unloading.

The right-hand side of Figure 4-12 shows the deformation of a R200 foam cell consequent to a similar loading-unloading sequence. This thick-walled cell initially deforms by bending of the cell-wall upon loading; subsequent unloading revealed that this deformation was permanent, and therefore plastic bending had taken place.

The *in-situ* compression tests described above showed that foams of low density collapsed by a combination of elastic buckling and plastic bending, with slender cell-walls undergoing elastic buckling and stockier cell-walls experiencing plastic bending. In high-density foams, the thick-walled cells deformed primarily by plastic bending of cell walls. Some tensile tests conducted in the ESEM revealed that the microscopic deformation mechanism was similar for high and low-density foams; this consisted of bending and

stretching of the foam cell-walls, while failure was by fast propagation of a fast unstable crack.

In-situ compression tests revealed that elastic cell-wall buckling occurred in the low-density foams even at very low levels of applied stress; typically this was observed in cells of large diameter and with slender cell-walls. The existence of this mechanism may justify the measured asymmetry of the elastic moduli in tension and compression; this asymmetry is indeed more pronounced for foams of low relative density.

4.3 Concluding Discussion

Analysis of the microstructure of the four foams under investigation revealed that the material comprises cells of tetrakaidecahedral shape, with different cell diameter and cell-wall thickness for each foam density; no simple scaling laws could be identified relating geometrical microstructural features to the foam relative density: the foam microstructure is strongly dependent on the manufacturing process (as well as on relative density). Cell diameter, cell-wall slenderness and their statistical distributions can deeply affect the macroscopic foam response; for example foams R110, of relatively high density, possess the highest average cell-wall slenderness of all foams investigated. The data presented in Figure 4-8 suggests that the measured stiffness and strength parameters for the R110 foam are systematically lower than the values predicted by the power-law fits $Y = A\bar{\rho}^b$ (Table 4-2). It appears reasonable to argue that this is due to the high slenderness of the R110 cell-walls, promoting elastic buckling mechanisms.

Foams of lower relative density and slender cell-walls display a tendency to undergo elastic buckling of the cell-walls under macroscopic compressive loading, while this phenomenon is not observed for foams of higher density and thicker cell-walls. The tendency of the low-density foams towards elastic cell-wall buckling in compression is observed even at low levels of stress, corresponding to the initial linear macroscopic response of the material. This observation is consistent with the measured asymmetry of elastic moduli in tension and compression, for a given foam density.

In-situ experiments revealed that macroscopic plastic collapse of the foams is driven by different mechanisms for low-density and high-density foams; collapse is initiated by a combination of elastic buckling and plastic bending of the cell walls for low-density foams, while plastic cell-wall bending is responsible for the macroscopic plastic collapse of high-density foams.

Existing micromechanical models for the elastic response of open-cell cellular solids (see for example (Chen & Lakes, 1995)) predict that the material stiffness scales with the relative density according to a power-law. If the active deformation mechanism is driven by axial loading of the cell-wall (e.g. cell-wall buckling), these models predict a power-law exponent approaching 1; on the other hand, if deformation is by cell-wall bending, the power-law exponent is 2 (for open-cell foams; the numerical values of the exponents of these scaling laws are slightly reduced for the case of closed-cell foams). The data presented in Figure 4-8 suggests that the measured variation of compressive elastic modulus with $\bar{\rho}$ could be better fitted by two distinct power-law expressions: namely, a power-law of exponent around 1.2 for $\bar{\rho} < 0.08$, and a power-law of exponent 1.8 for $\bar{\rho} > 0.08$. The observed increase of power-law exponent with relative density is consistent with the notion of different deformation mechanisms active for the low-density and high-density foams.

The experimental findings reported in this study suggest that the geometric features of the foam microstructure and their statistical distribution can substantially affect the macroscopic mechanical response. The tension/compression asymmetry of foam stiffness and yield stress are examples of the effect of foam microstructure on its macroscopic response. In the following chapter, the data and understanding generated from the quasistatic

test results and SEM observations will be further used to understand the sensitivity of the foams response to strain rate and temperature.

Chapter 5

Compressive Deformation of Rohacell Foams: Effects of Strain Rate and Temperature

In the aerospace industry conventional metallic components are increasingly being replaced by composite sandwich structures in an attempt to increase specific stiffness and strength, as well as durability. Polymer foams are often used as the core of these sandwich structures. Considering the wide range of temperatures at which structural components in an aircraft operate, and as many components are exposed to the risk of impact loading, it is necessary to develop a thorough understanding of the mechanical response of cellular polymers and their sensitivity to both temperature and applied strain rates.

This chapter provides a comprehensive data-set for the rate dependence of all four densities of Rohacell foam under compressive loading at strain rates between 10^{-3} and 5000 s^{-1} at room temperature (23°C). As well as

providing stress-strain data, observations on the failure of the material are made. In order to better understand the behaviour at high strain rates, further quasi-static experiments (at 10^{-2} s^{-1}) are performed at five further temperatures from -70 to +200°C. The similarity between the effects of increasing strain rate and decreasing temperature on the foam response is demonstrated, and by using a recently established time-temperature superposition method, the data at different temperatures are used to validate, and better understand the causes of, the observed rate dependence. The novel findings from this chapter have been published in the International Journal of Impact Engineering (Arezoo et al., 2013)

5.1 Experimental Methods

5.1.1 Specimen Size and Preparation

As discussed in Chapter 3, quasistatic experiments at room temperature showed that the measured mechanical response was independent of specimen size for a wide range of sizes. Based on these data, circular cylindrical specimens of diameter 9 mm and height 4 mm were used in all room temperature experiments, independent of the imposed strain rate. The choice of such small specimens was dictated by the specific requirements of high strain rate testing, namely: rapidly achieving stress equilibrium; minimising stresses due to lateral inertia; and achieving sufficiently high specimen strain rates without yielding the loading bars in the Split-Hopkinson bar used for the experiments. Chapter 3 provides a more comprehensive discussion on the experimental apparatus employed, however, a brief description of specific points pertinent to the current experiments is also provided in section 5.1.3.

Quasi-static experiments conducted at different temperatures were performed on cuboidal specimens measuring $15 \times 15 \times 10$ mm. This choice was dictated by the constraints imposed by the environmental chamber used in the tests. All samples were machined by conventional methods and were cut in such a way that the specimen's axis was aligned with the thickness direction of the foam plates.

5.1.2 Quasistatic and Medium Rate Experiments

Uniaxial compression experiments were performed at room temperature and at different strain rates in order to determine the sensitivity of the

mechanical response to the loading rate. Strain rates between 10^{-3} and 10^{-1} s^{-1} were achieved using a screw-driven Hounsfield machine which forced plastic collapse of the specimen by means of two flat metal platens whose surface was lubricated with PTFE spray. The load was measured with a resistive load cell whereas compressive strains were measured by a non-contact laser extensometer. Tests were also video-recorded by a digital camera in order to observe the macroscopic mechanism of deformation.

Medium strain rates (1 to 100 s^{-1}) were achieved using a bespoke, hydraulically-driven loading rig fitted with a resistive dynamic load cell. The specimen was placed in contact with two lightweight metallic cylinders; one of these cylinders was stationary while the other one was accelerated to speeds of the order of 2 m s^{-1} (with negligible acceleration times), causing plastic deformation of the specimen. The shortening of the specimen was measured by a high speed video-camera (Vision Research, Phantom model 7.1) and bespoke image analysis software, thereby determining the strain history for the specimen.

5.1.3 Split Hopkinson Pressure Bar (SHPB) Experiments

High strain rates (ranging from 800 to 5000 s^{-1}) were obtained with a Split-Hopkinson Pressure Bar setup (SHPB). Chapter 3 provides a detailed description of this test method, where further information can also be found in (Gray III, 1999). Due to the low strength of the polymer foams tested in this study, a dedicated Hopkinson bar of enhanced sensitivity was developed in order to increase the signal-to-noise ratio. The apparatus was similar to that developed by other authors for materials of similar strength and comprised

magnesium alloy bars of diameter 12.7 mm, the input and output bars were 1 m and 0.5 m long respectively. Both bars were instrumented with foil strain gauge stations placed halfway along the length of the input bar and at a distance of 50 mm from the specimen end of the output bar. Forces in the bar were recorded by connecting the strain gauge stations to a Wheatstone bridge and a 500 kHz Fylde signal amplifier with a gain of 1000. The gauges were calibrated statically and dynamically. The displacement of the specimen ends were obtained by both direct observation using an ultra-high speed camera (model SIM-X 16) and calculation via the classic analysis of the force signals; the two methods provided similar strain-time histories.

High-speed photographs were taken in conjunction with the SHPB experiments and used to measure the history of strain field in the specimen as a function of time, by means of a digital image correlation procedure; it was found that the strain field in the specimens was uniform. It was observed that while foams R51, R71 and R110 showed a ductile response, with little evidence of fracture, R200 underwent brittle microcracking upon compression; the material in contact with the input bar was progressively eroded with increasing applied strain, and this manifested in a uniform cloud of sub-mm fragments being ejected radially during the test.

Figure 5-1a shows the typical “trapezoidal, almost square wave” pulses as seen in conventional SHPB experiments (Gray III, 1999) for R200, with a striker bar speed of approximately 6.5 m s^{-1}, giving a strain rate of 1500 s^{-1} (Figure 5-1b). The stress versus strain time history measured with the SHPB setup is only valid after dynamic stress equilibrium of the specimen has been

achieved, i.e., when the forces exerted on the sample by the input and output bars attain the same value.

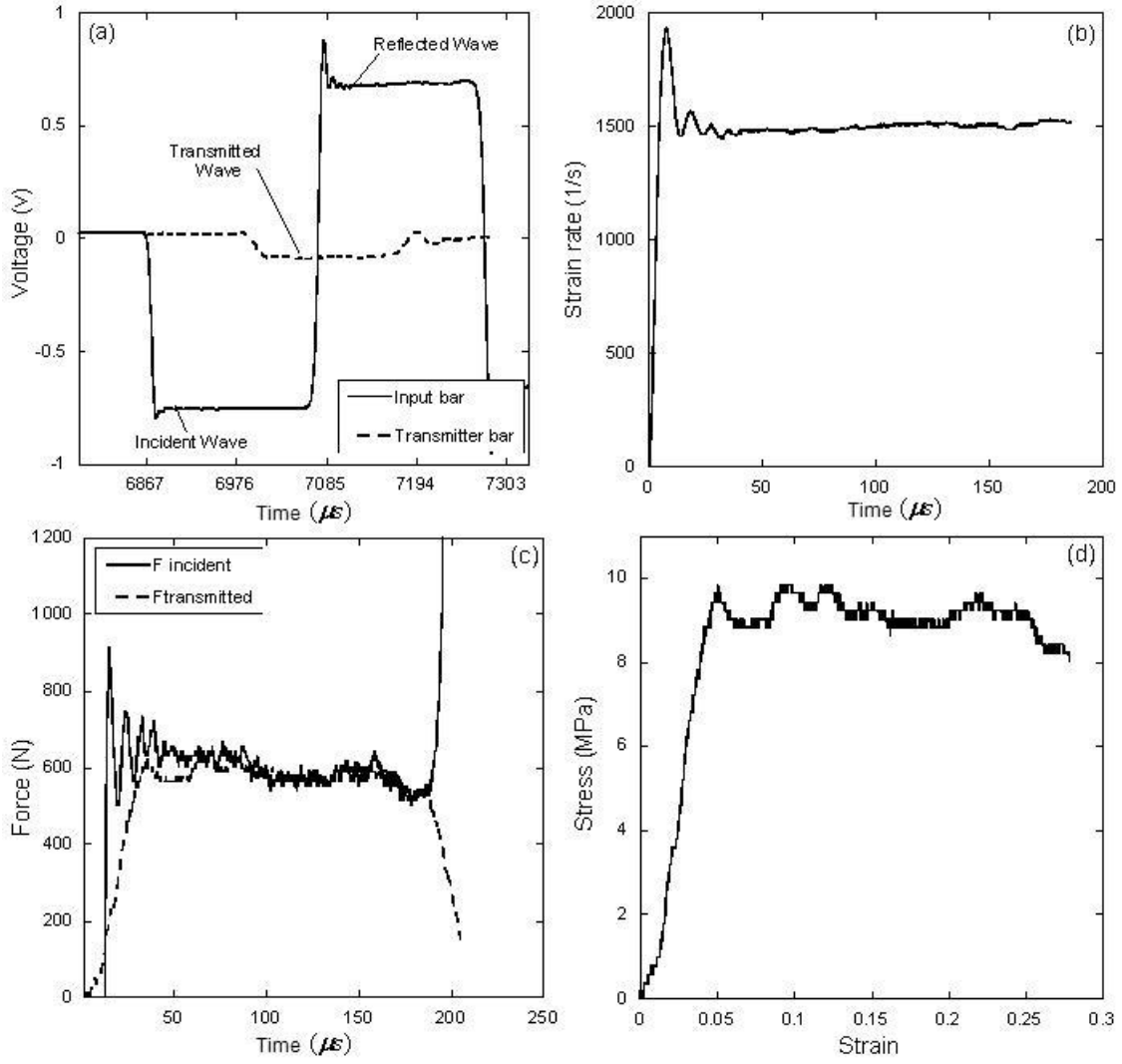


Figure 5-1: Experimental data gathered from the SHPB test, showing the incident and reflected voltage readings (a) at a strain rate of 1500 s^{-1} (b). The axial force histories on the two ends of the specimen indicate stress equilibrium (c). The processed data is used to obtain the dynamic compressive stress-strain curve (d).

For each of the experiments performed, the instant at which equilibrium was achieved was determined, by plotting the forces on the front (calculated from the incident and reflected waves) and rear (calculated from the transmitted wave) face of the specimen as functions of time. Figure 5-1c gives an example

of such plots for R200 tested at a strain rate of 1500 s^{-1}. It is clear that the specimen is in equilibrium after about 50 μs from the beginning of the test; at this time the compressive strain in the specimen is of the order of 0.1, i.e., the applied strain is in excess of the yield strain. A similar response was observed for all SHPB experiments. It follows that the SHPB experiments cannot be used to calculate the apparent stiffness of the material; on the other hand, they permit valid measurements of the flow stress of the foam during the plastic collapse phase. Once the necessary dynamic test conditions are satisfied, the data is processed to obtain the dynamic stress-strain curves (Figure 5-1d).

Hopkinson bar experiments were repeated for all foam densities over a range of strain rates and the results were compared against the quasistatic and medium rate experiments. The duration of the test was not sufficient to capture the densification region of the foam, which, as seen from the quasistatic tests, usually occurs above 60% strain. However, the stress plateau region was observed and quantified as the average flow stress at between 10 to 50% plastic strain.

5.2 Experimental Results and Discussion

5.2.1 Strain Rate Sensitivity of the Response at Room Temperature

Preliminary quasi-static compression experiments conducted on all foam densities, with specimens cut in three mutually perpendicular directions, confirmed that the material response was insensitive to direction (further detailed in Chapter 3). Compressive tests at all strain rates were repeated a minimum of five times and it was found that the measured stress versus strain response was highly repeatable, with scatter in flow stress below 10%.

Selected compressive stress versus strain responses for all four foam densities are shown in Figure 5-2, which includes data from low, medium and high strain rate tests for foams R51, R71, R110 and R200. In this figure, for clarity, only on test per strain rate region is shown and scatter is reported in Figure 5-4.

The different foams display different sensitivity to the imposed strain rate. Foams R51 and R71 exhibit a mild rate sensitivity, with the plateau stress increasing by around 20 to 30% when the strain rate is increased from 10^{-3} s^{-1} to 10^{3} s^{-1}. R110 exhibits an almost rate insensitive behaviour; in contrast, the flow stress of R200 increases by more than 30% with strain rate increasing from 10^{-3} s^{-1} to 10^{2} s^{-1}, but then decreases as the applied strain rate reaches 10^{3} s^{-1}. For all foams and at all strain rates, negligible transverse strain was observed in the photographs taken during the experiments, implying that for these foams the plastic Poisson's ratio is close to zero.

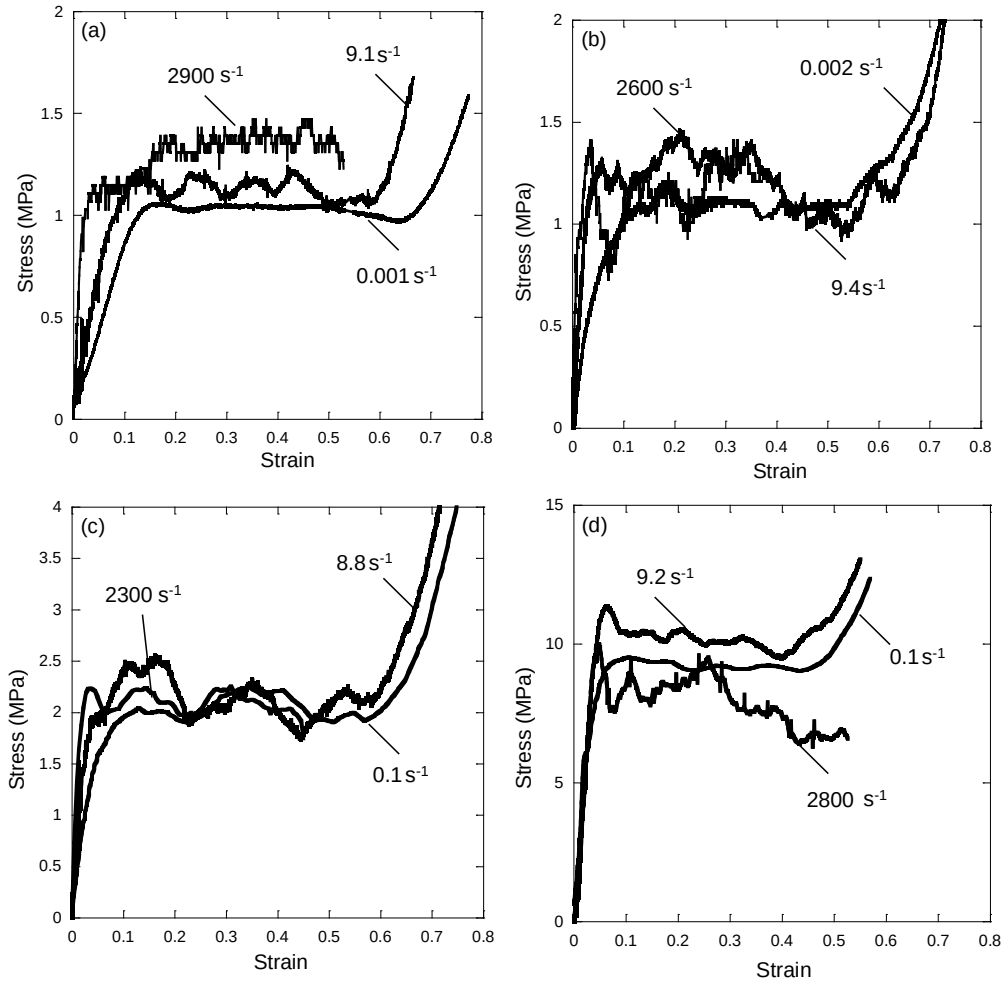


Figure 5-2: Compressive stress-strain response of Rohacell foam, tested at room temperature and different strain rates (T=23°C, $\dot{\varepsilon} = 10^{-3}$ to 10^{4} s-1); (a) R51; (b) R71; (c) R110; (d) R200.

At strain rates up to 10^2 s^{-1} the response of all foams comprises a linear phase followed by plastic collapse with negligible strain-hardening (plateau phase) and final densification. At higher strain rates, on the order of 10^3 s^{-1} the stress-strain curves for all foams display higher oscillations in stress, which may indicate a more brittle response. At these rates, the plastic collapse response of the material is different in the four foams: R51 and R71 display a mild strain hardening response, R110 collapses at approximately constant flow stress, whereas R200 exhibits a mild strain softening. The softening of R200 is in line with the brittle fracture mechanism observed via high-speed photography at

high strain rates (see Figure 5-3 and Figure 5-5). Densification cannot be fully investigated in the SHPB tests, in which the loading ends at compressive strains of the order of 0.5.

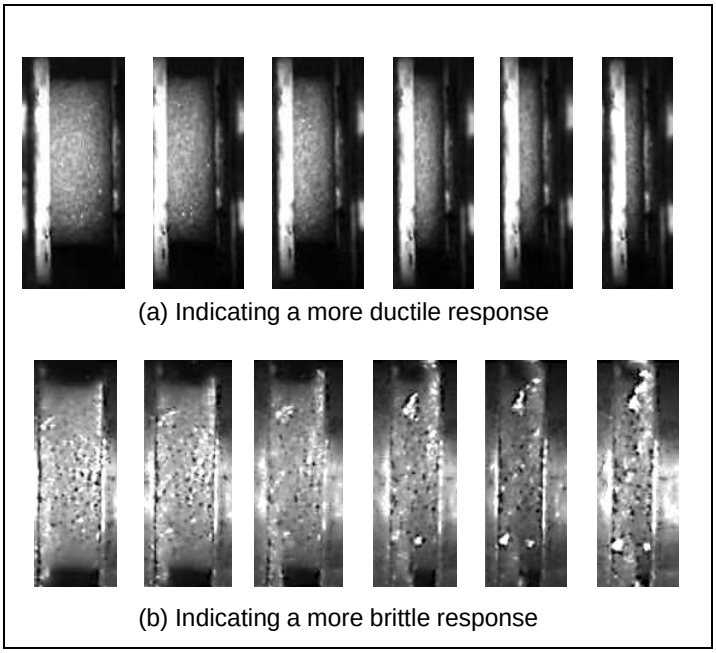


Figure 5-3: A sequence of photographs taken during compression testing of R200, (a) at quasistatic (T=23°C, $\dot{\varepsilon} = 10^{-3}\ s^{-1}$) and (b) at high strain rate (T=23°C, $\dot{\varepsilon} = 10^{3}\ s^{-1}$) loading conditions.

In order to summarise the strain rate dependence of the four foams tested, Figure 5-4 shows the measured collapse stress (defined as the flow stress at a nominal plastic strain of 0.2) as a function of the applied strain rate for all specimens; similar trends are followed by the plateau stress (defined as the average flow stress at nominal compressive strains between 0.1 and 0.5) versus strain rate data. The low strength of R200 at high strain rates is again consistent with the brittle failure mechanisms displayed in SHPB tests for this foam. This is evident in Figure 5-3, which shows images of R200 taken during quasistatic and high strain rate tests. At low-loading rates, the material behaves

in a ductile manner and is tolerant of greater loads due to its ability to redistribute the load through the yielding process. However, at high loading rates brittle fracture occurs ahead of yield failure. This type of failure is catastrophic, requires less energy than a yield failure and hence, is associated with low-energy absorption levels.

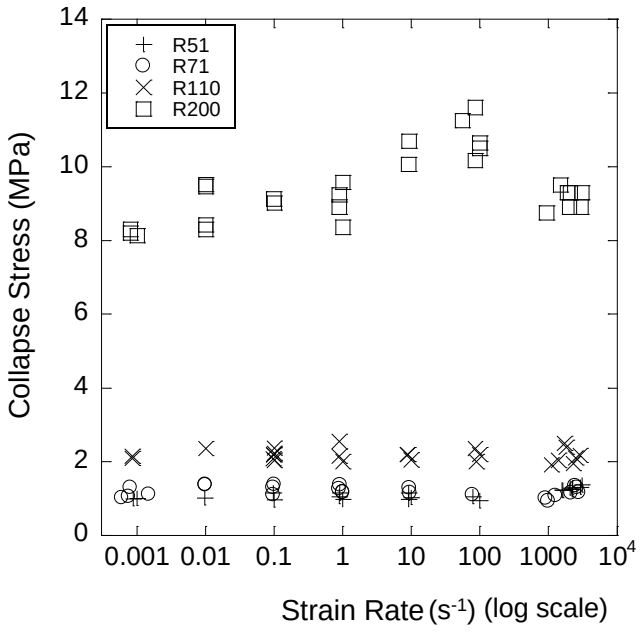


Figure 5-4: Summary of the sensitivity of the compressive collapse stress to the imposed strain rate (T=23°C, $\dot{\varepsilon} = 10^{-3}$ to 10^{4} s^{-1}), for all the foams tested in this study.

Embrittlement of polymers at high rates of strain is commonly observed (Gray III 1999; Soni et al. 2009; McCrum et al. 1997; Richeton et al. 2006), and different authors have reported a similar behaviour for other polymeric foams (e.g. (Song et al. 2004)).

To understand this behaviour in more detail, it is useful to consider the parent material. The composition of the raw polymer is rarely known with precision for polymer foams, as chemical changes during the foaming process followed by a certain degree of polymer chain alignment, ageing and oxidation

of the polymer all affect its final composition. According to the manufacturer, the raw polymer for Rohacell foam is close to Polymethylmethacrylate (PMMA). When loaded in compression at moderate to high-strain rates, PMMA, in common with many polymers, exhibits a significant reduction in apparent strain hardening, which is attributed by many authors to adiabatic heating effects, whereby some fraction of the plastic work is converted to heat (Arruda et al. 1995; Mulliken & Boyce 2006; Richeton et al. 2006). It must be noted that these adiabatic effects are sometimes observed even under quasistatic loading due to the low thermal diffusivity of polymers. It is expected that eventually (with increasing strain) the thermal softening effect will be dominated by strain hardening due to the evolution of chain orientation with increased plastic strain. However, as the adiabatic temperature rise approaches the glass transition temperature, the effect on the strain hardening rate is greater. In the case of PMMA, when tested at loading rates exceeding 1000 s^{-1}, the strain hardening effect can completely disappear (Richeton et al. 2006).

It has also been reported that the compressive behaviour of many polymers appears to transition from ductile to brittle when tested at low to high strain rates (Arruda et al., 1995). Some materials, including PMMA, are highly susceptible to crazing, and fracture is by craze nucleation, followed by craze breakdown into tensile microcracks (Fleck et al. 1990). Any local in-homogeneity can lead to a local tensile stress which can initiate this brittle failure. Therefore, the compressive behaviour of R200 is consistent with its being dominated by the response of the raw polymer. Softening is evident at high-loading rates (shown as a reduced slope in the strain hardening curve in

Figure 5-2). It would appear from the experimental evidence gathered so far that the main contributing factor affecting the apparent drop in yield and plateau strength is not thermal instability, but brittle fracture.

Embrittlement of the parent polymer is not necessarily the only reason for the brittle response of R200 at high strain rates, given the different response observed in other foams made from the same polymer at the same strain rates. It was reported in Chapter 4 that the four foams under investigation possess different microstructural features, such as cell size and wall thickness. The local maximum strain in the cell walls scales linearly with the microscopically applied strain rate (Gibson & Ashby 1999) by a constant of proportionality which depends on the geometrical details of the microstructure (assuming microscopic collapse by plastic cell wall bending). It is therefore possible that the relatively long and slender cell walls of foams of low density result in lower local strain rates than those applied to the stockier cell walls of R200, for a given imposed macroscopic strain rate. In addition, upon compression, the gas trapped in these closed cell foams can affect the state of stress at a microscopic level and therefore the onset of failure. However, a detailed analysis of the relative influence of these mechanisms upon the macroscopic foam response is beyond the scope of this study.

In contrast to R200, R51 was seen to behave in a relatively ductile manner, even at high loading rates. After each test, most of the 4mm thick Rohacell foam specimens were highly damaged or disintegrated; however, it was observed that unlike the other densities, R51 remained almost intact,

although in a compact rubbery state. Figure 5-5 shows an example of a R200 and R51 test sample, after being subjected to a high strain rate experiment.

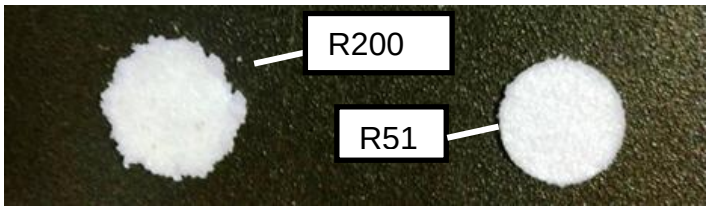


Figure 5-5: R200 and R51 test samples post SHPB experiment

The stress-strain response of R51 also indicates signs of strain hardening with increased plastic strain. R51 showed an elevation of approximately 30-40% plateau strength between the lowest and highest strain rates. Some researchers argue this enhancement can be due to shock waves propagating through the material (Reid & Peng 1997). In these cases, the enhanced dynamic plateau stress σ_d is given by:

$$\sigma_d = \sigma_p + \frac{\rho_0 v^2}{\varepsilon_D} \qquad [5\text{-}1]$$

where σ_p is the plateau stress, ρ_0 is the density, ε_D is the densification strain and v is the impact velocity. For the range of densities and velocities analysed in this study the example of (Deshpande & Fleck 2000) is followed and a criterion of 20% elevation in strength is adopted to define the impact velocity at which shock waves become important. Using this criterion, shock propagation effects become important at impact velocities exceeding about 50 m s^{-1}. These velocities are greater than those encountered in this study (max velocity reached for SHPB testing was 15 m s^{-1}).

In summary, the most likely underlying cause of the observed rate dependence in the material is the inherent strain rate sensitivity of the raw

polymer. At higher foam densities, the ductile to brittle transition behaviour, which is interlinked with the relative density of the foam, leads to material failure by the nucleation and growth of crazes. Cracks form by the breakdown of a craze, and propagate towards catastrophic growth. This leads to brittle fracture occurring at stress levels below the yield stress, with the foam behaving in an almost elastic-brittle manner. Following the example of previous authors (Siviour et al. 2005), this will be confirmed through use of the time-temperature superposition principle, which allows the polymer behaviour to be modified without introducing inertia driven effects.

A simplified form of the Eyring equation shows that the effect of rising temperature on the material deformation is equivalent (in the sense of producing the same flow stress) to its behaviour at ambient temperature at a lower strain rate (Walley & Field 1994), according to the following relation:

$$\ln \dot{\varepsilon}_1 = \frac{T_0}{T_0 + \Delta T} \ln \dot{\varepsilon}_0, \qquad \textit{[5-2]}$$

where T_0 is the ambient temperature (295 K), $\dot{\varepsilon}_0$ is the imposed strain rate and $\dot{\varepsilon}_1$ is the equivalent strain rate. If the test data and understanding of the foam behaviour at high strain rates are correct, it would be expected that similar behaviours occur when this material is tested at low temperatures and quasistatic loading rates. In the next section, a comprehensive study towards understanding the effect of temperature on the deformation behaviour of this material at different foam densities is presented.

5.3 Compression Tests at Different Temperatures

5.3.1 Experimental Methods

For quasistatic testing at different temperatures, the experiments were conducted at a nominal imposed strain rate of 10^{-2} s^{-1} and at seven temperatures (namely, 203, 233, 263, 278, 296, 343 and 473 K), in order to determine the sensitivity of the response of all foams to temperature. The tests were performed in a screw-driven Instron machine coupled with an environmental chamber; load was measured by a resistive load cell of 5 kN capacity placed outside the chamber, while specimen shortening was measured by a mechanical, resistive extensometer connected to the loading platens (after calibration of this extensometer at all the temperatures at which tests were performed). The chamber was equipped with resistive heating elements which were employed in tests above room temperature; low temperatures were obtained by circulation of cold nitrogen vapour inside the chamber, and the temperature control was performed automatically by the environmental chamber. An additional temperature reading was obtained by a thermocouple connected to the loading platens. In all test cases, to minimise friction, the platens were lubricated with petroleum jelly (Trautmann, 2005).

5.3.2 Sensitivity of the Quasistatic Response to Temperature

Figure 5-6 presents a summary of the measured compressive stress-strain response for all foams at a strain rate of 10^{-2} s^{-1} and at temperatures ranging from 203 to 473 K.

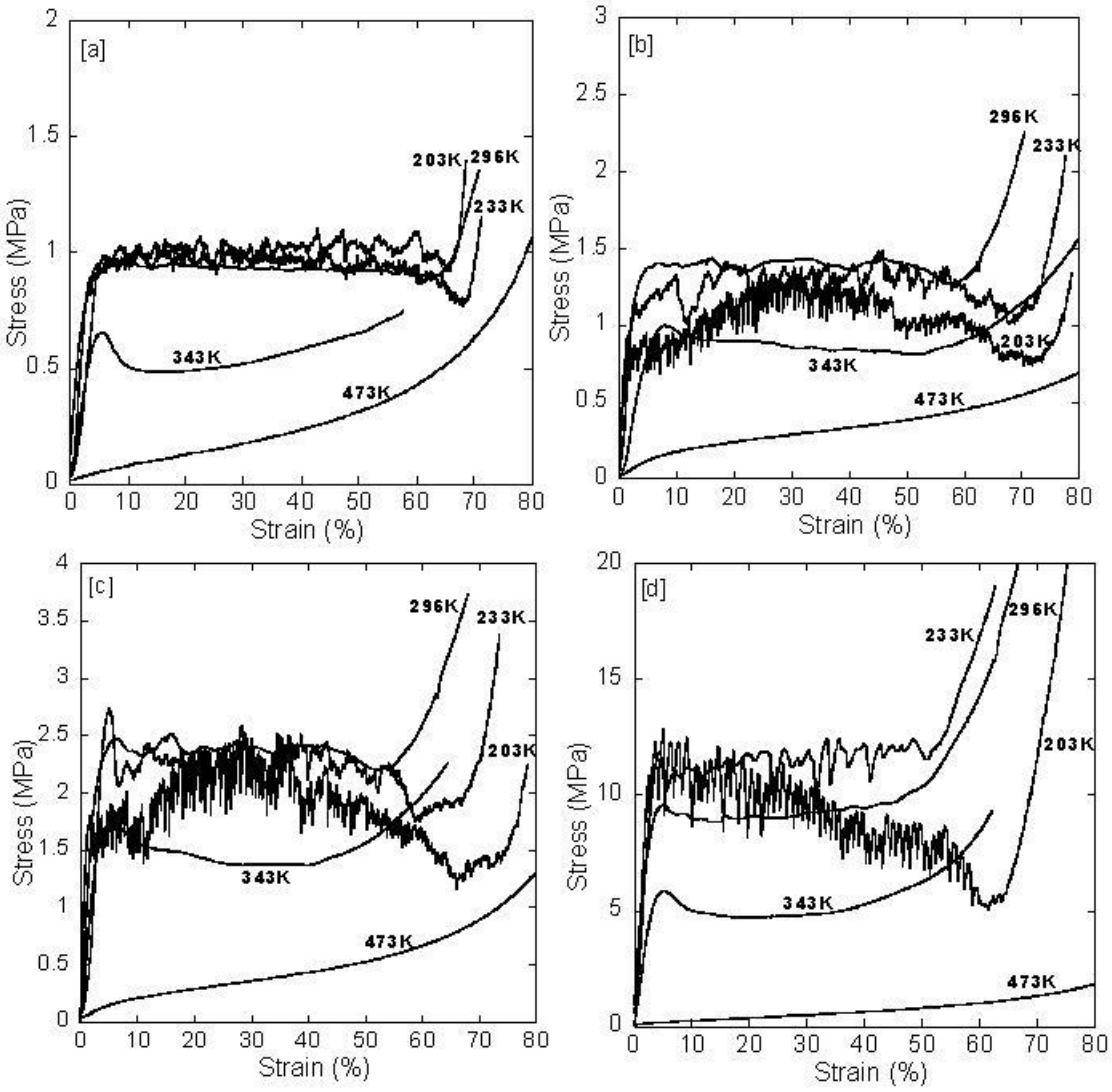


Figure 5-6: Compressive stress-strain response of Rohacell foams at a strain rate of $\dot{\varepsilon} = 10^{-2}\, s^{-1}$ *and different temperatures in the range 203-473 K ; (a) R51; (b) R71; (c) R110; (d) R200.*

At the highest temperature of 473 K, all foams display a soft response with no clearly defined yield point, indicating that the material is above its glass transition temperature and undergoes viscous flow. Figure 5-7 contains photographs of specimens made from all foam materials after testing at this temperature, and shows that foams underwent permanent deformation, driven by the trapped gas in the foams' closed cells. The lateral 'bulging' of the specimens is more pronounced for R200.

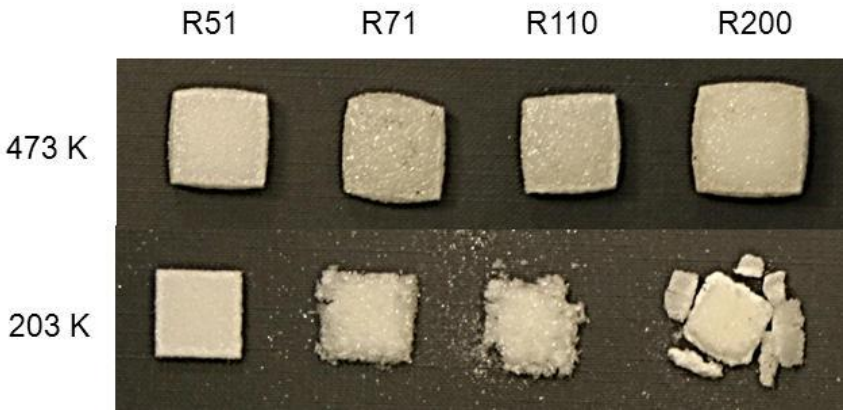


Figure 5-7: Photographs of foam specimens after quasi-static compression (up to densification strain) at temperatures of 203 and 473 K.

Figure 5-8a shows the sensitivity of the measured foam stiffness to temperature; it is clear that the stiffness of all foams has dropped substantially at 473 K, consistent with them being above their glass transition temperature. If the temperature is decreased to the range 233-343 K, the measured response of all foams shows an approximately linear viscoelastic phase followed by visco-plastic collapse and final densification, with stiffness increasing with decreasing temperature. At the lowest temperature of this range (233 K) the measured flow stress begins displaying oscillations, indicating a transition towards a brittle response.

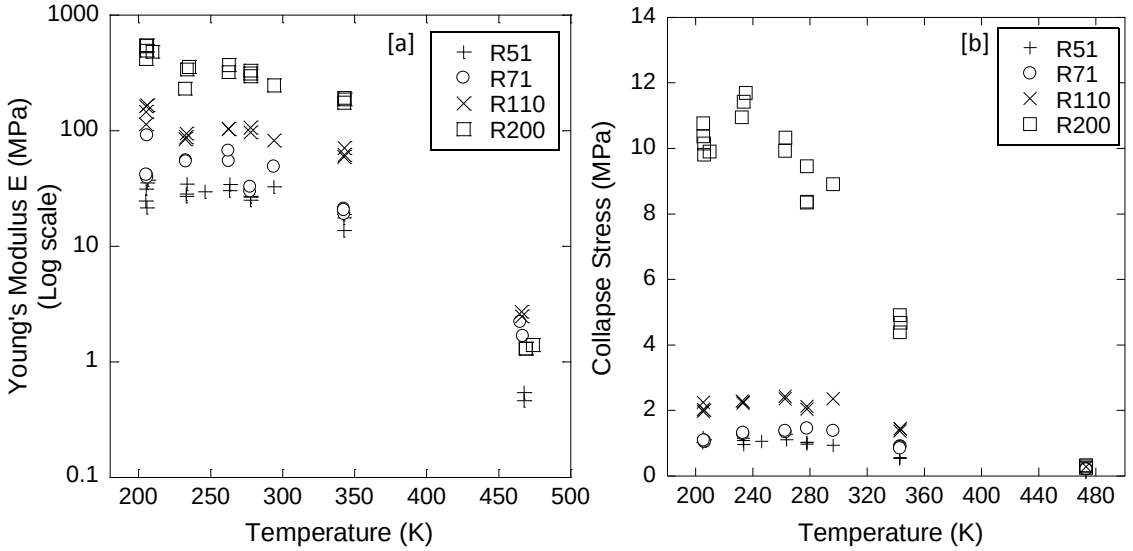


Figure 5-8: Summary of the sensitivity of (a) the foams' Young's modulus E and (b) the collapse stress to temperature (T=203-473 K, $\dot{\varepsilon} = 10^{-2}\ s^{-1}$), for all foams tested in this study.

When the temperature is further decreased to 203 K all foams display high oscillations in the measured stress/strain history, clearly indicating a brittle response (a further indication of a brittle response was the high level of acoustic emission observed for tests at this temperature). Foams of different densities show a different hardening response at 203 K: while R51 collapses at a constant stress prior to densification, R71 and R110 display an initial strain hardening and subsequent strain softening, attributable to fracture events, prior to densification. The R200 foam shows an approximately linear strain softening after the onset of collapse. Evidence of brittle response at 203 K can be gathered by observing different foam specimens following the compression experiments, as shown in the lower part of Figure 5-7. It is also clear from these photographs that foams of lower relative density show less evidence of fracture mechanisms while foams of higher density, such as R200, display a pronounced brittle response with evident cracking.

Figure 5-8b presents the sensitivity of the collapse stress (again, defined as the flow stress at a nominal plastic strain of 0.2) to temperature (similar trends are observed for the plateau stress). As the temperature is decreased from 473 K the collapse stress tends to increase; however at a critical temperature this tendency is inverted and the collapse stress decreases by further decreasing the temperature. The critical temperatures are approximately 203 K, 263 K, 278 K and 263 K for foams R200, R110, R71 and R51, respectively. The measured sensitivity of the collapse stress to increasing imposed strain rate (Figure 5-2 & Figure 5-4) is remarkably similar to the sensitivity exhibited by the foams to decreasing temperature (Figure 5-6 & Figure 5-8b). Figure 5-9 shows a direct comparison of selected stress/strain histories: in Figure 5-9a the similarity of the high strain rate response of R200 at room temperature and the quasi-static response of the same foam at 203 K is outlined. In Figure 5-9b it is shown that for the case of R51, the quasi-static response at 203 K is more similar to the medium-rate response at room temperature than to the high strain rate response at room temperature; however it should be noted that the quasi-static collapse stress at 203 K is only 15% lower than the collapse stress at room temperature and high strain rate.

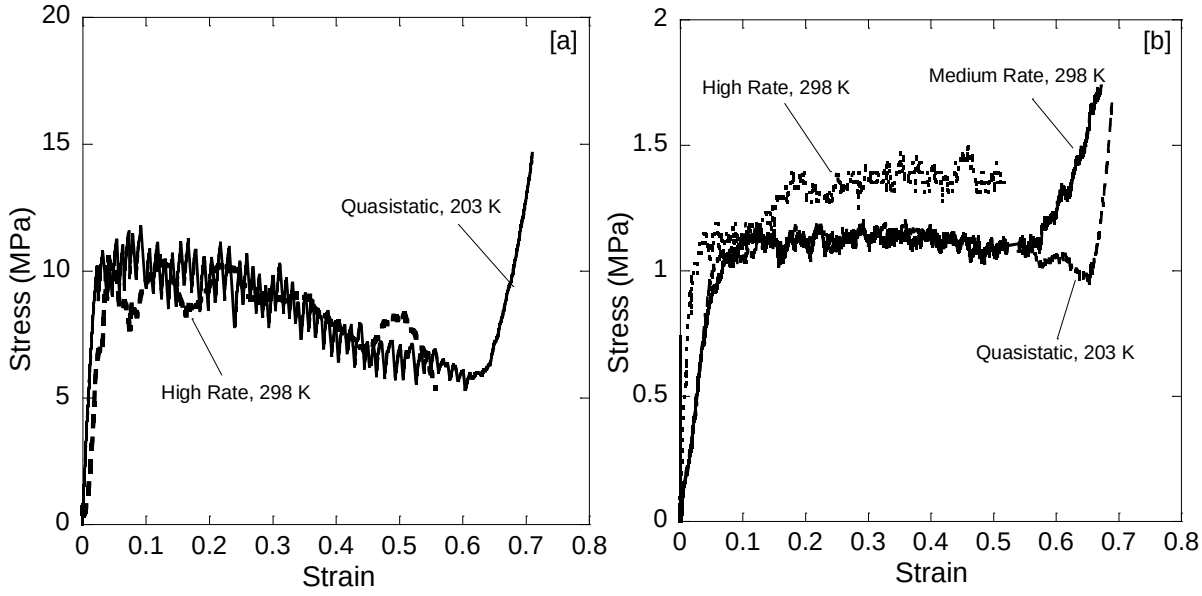


Figure 5-9: (a) Comparison of two stress/strain responses of R200 at $\dot{\varepsilon}=10^{3}\ s^{-1}$, $T=298$ K and $\dot{\varepsilon}=10^{-3}$, $T=203$ K; (b) comparison of three stress/strain responses of R51: $\dot{\varepsilon}=10^{3}\ s^{-1}$, $T=298$ K and $\dot{\varepsilon}=10^{-3}\ s^{-1}$, $T=203$ K and $\dot{\varepsilon}=10^{2}\ s^{-1}$, $T=298$ K.

Figure 5-10 shows a direct comparison of selected post-test specimens. The similarity of the high strain rate response of R200 and R51 at room temperature and the quasi-static response of the same foam at 203 K is outlined.



Figure 5-10: Similarity of the high strain rate response of R200 and R51 at room temperature and the quasi-static response of the same foam at 203 K.

The observations above reinforce the idea that the sensitivity of the response of these foams to temperature and strain rate is mainly related to the strain rate and temperature sensitivity of the parent polymer, with the details of the foams microstructure having a less important effect. If this is the case, the time-temperature superposition principle can be employed to map the data obtained at different strain rates to the data measured at different temperatures.

5.4 Time-Temperature Superposition

To gather an understanding of material behaviour over a wide range of strain rates, ranging from quasistatic to high loading rates, a single experimental technique at one temperature will not suffice. It would be most beneficial if a simple interrelation were to exist between time-scale and temperature, such that all the required experiments to map out a materials response could be made on a single test machine with a limited strain rate range, where the test temperature could vary. This would negate the large number of experimental approaches currently needed to map out the strain rate response. It is considerably more convenient to change the temperature of an experiment, in order to bring the points of interests to within a time-scale that is readily available. This is achievable by using the time-temperature superposition principle, which provides a simple interrelation between time-scale and temperature. This principle basically implies that the viscoelastic behaviour of a material at experiments performed at a fixed strain rate and varied temperatures is conceptually equivalent to experiments performed at a fixed temperature and varied strain rate (and vice versa) (Ward & Sweeney, 2005).

In an investigation by Siviour *et al.* (2005) the strength of polycarbonate and polyvinylidene difluoride was investigated over a wide range of strain rates at room temperature, and again at a high loading rate and varied temperatures. A simple empirical formula was then used to map the two sets of data in the form of:

$$T = T_0 + A(\log \dot{\varepsilon}_0 - \log \dot{\varepsilon}) \qquad [5\text{-}3]$$

where T_0 is the room temperature, $\dot{\varepsilon}_0$ is the nominal strain rate of the hopkinson bar experiments and A is a constant value signifying the time/temperature sensitivity. This formula is very similar to the well-known Williams-Landel-Ferry (WLF) type time-temperature superposition function (Williams et al., 1955), which describes a shift function relating changes in time to changes in temperature observed in the mechanical properties of viscoelastic solids such as polymers. The simple one parameter formula (Equation [5-3]) was successfully used to map the compression stress-strain curves at different strain rates to those at different temperatures using a constant value of A=17 K per decade of strain rate. It was concluded that the increase in strength observed in each material at high strain rates was due to the shift of low temperature polymer relaxations to room temperature via Equation [5-3].

Williamson *et. al* (2008) similarly mapped the compressive strain rate/temperature data for a polymer bonded explosive using a time-temperature superposition similar to Equation [5-3]. In their study an empirically determined sensitivity of 13K per decade of strain rate was used to successfully map the data. In this study, using the collected data at different strain rates and temperatures, the apparent change in strain rate was measured graphically, as a function of temperature, using Equation [5-3].

5.4.1 Time Temperature Superposition Results

The temperature and strain rate data was reduced to a single parameter - plateau stress - for comparison. In Figure 5-8b and Figure 5-4 the dependence of the collapse (or plateau) stress on temperature and strain rate is

presented, respectively. Using Equation [5-3], a value of A=17 K was found to successfully map the variable strain rate data onto the variable temperature data (see Figure 5-11). The room temperature (T_0) was chosen as 23°C (296 K) and the nominal strain rate ($\dot{\varepsilon}_0$) for the variable temperature tests was chosen as 0.01 s^{-1}. The mapping was accurate within 10-15% in the range 203 to 296 K.

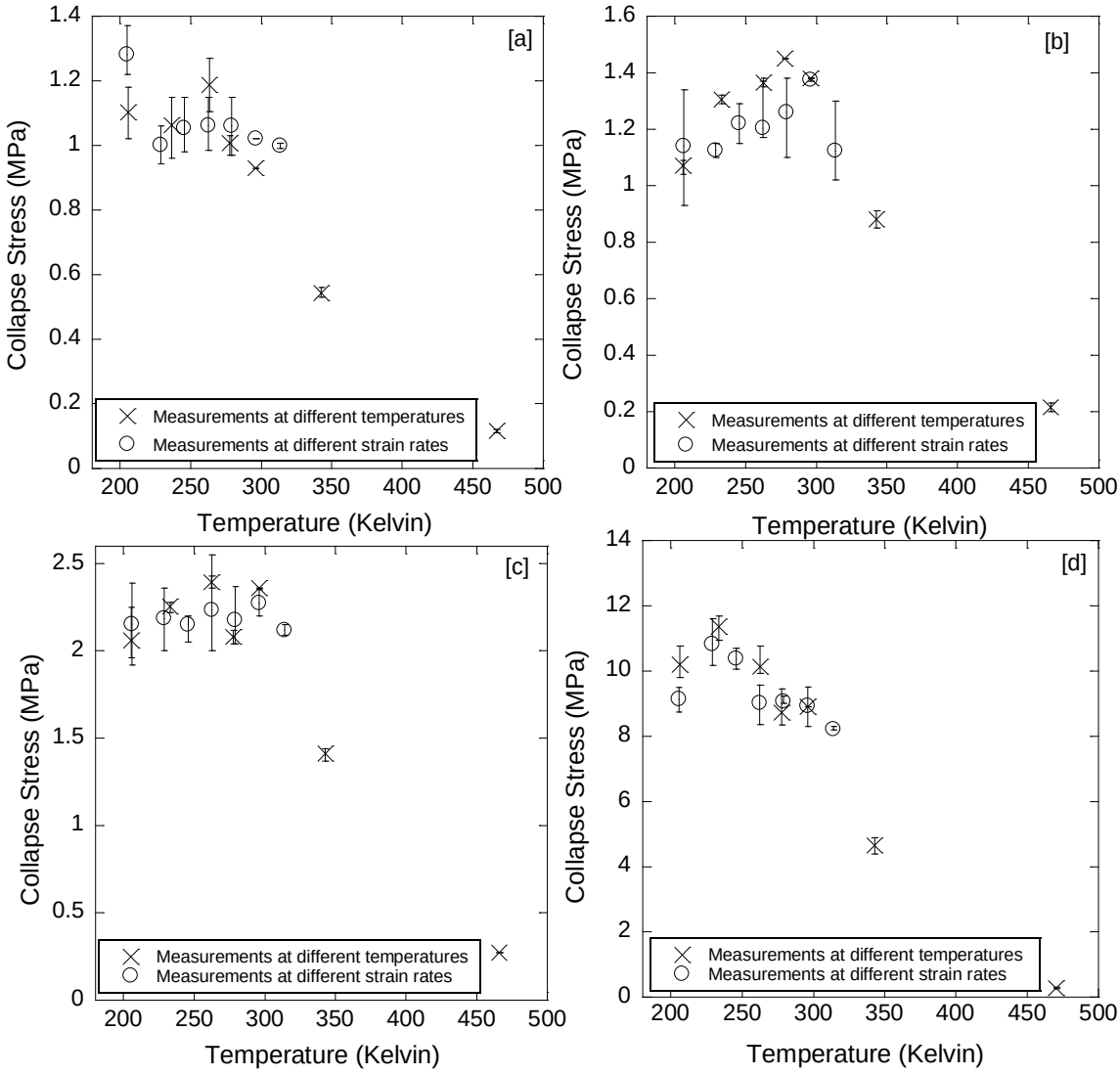


Figure 5-11: Measured collapse stress as a function of temperature; data obtained at different strain rates was mapped to the temperature axis by using equation [5-3]; (a) R51; (b) R71; (c) R110; (d) R200.

5.5 Foam Stiffness

In Chapter 4 the sensitivity of the apparent compressive foam stiffness E_F to the relative density $\bar{\rho}$ at $\dot{\varepsilon}$=10^{-2} s^{-1} and T =296K was measured and it was found that this could be expressed by the power-law relation $E_F = E_S \bar{\rho}^{m_E}$, where E_S=4106 MPa is the compressive stiffness of the solid parent polymer material at the same strain rate and temperature, and m_E =1.47 is a material property. It is known that at temperatures well below the glass transition temperature T_g the stiffness of solid polymers can be taken to vary linearly with temperature

$$E_S(T) = E_S^0\left(1-\alpha\frac{T}{T_g}\right) = E_S^0(1-\beta T) \qquad [5\text{-}4]$$

where $E_S{}^0$ is the stiffness of the polymer at 0 K and β is a fit parameter. Upon assuming that the scaling relation measured in Chapter 4 is valid at every temperature, we can write

$$E_F \Big/ \bar{\rho}^{m_E} = E_S^0(1-\beta T) \qquad [5\text{-}5]$$

which gives the foam stiffness as a function of relative density and temperature. Figure 5-12 shows a best fit of equation [5-5] through the measurements conducted in this study, giving $E_S{}^0$=10125 MPa and β=2.14 $\times 10^{-3}$ K^{-1} for the Rohacell foams investigated here. This formula can be employed to obtain estimates of foam stiffness in preliminary design calculations for Rohacell foams of varying density at varying temperatures, when an uncertainty of a factor of ca. 2 can be tolerated.

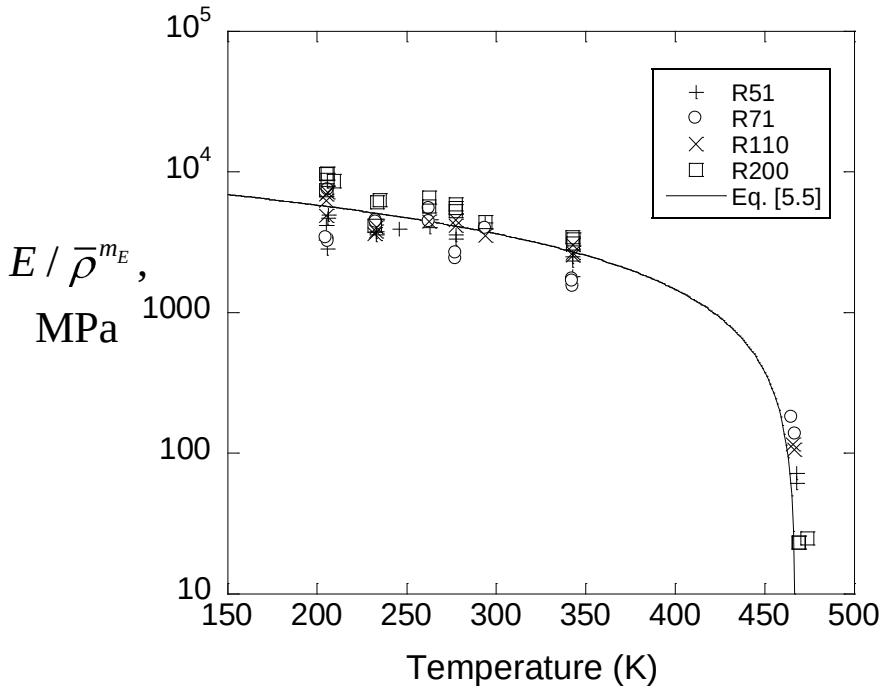


Figure 5-12: Normalised apparent foam stiffness versus temperature. Predictions from Eq. [5-5] are compared to experimental data for all foams tested

5.6 Conclusions

The uniaxial compressive response of Rohacell foams of grade WF and density of 51, 71, 110 and 210 kg m^{-3} was measured at strain rates from 10^{-3} to 5×10^{3} s^{-1} and at temperatures ranging from 203 to 473 K. All foams exhibited mild strain rate sensitivity and a ductile response at low to medium strain rates, but showed progressive embrittlement as the strain rates were increased beyond 100 s^{-1}. The materials displayed great sensitivity to the imposed temperature; the response was of rubbery type at 473 K, but showed the characteristics of an elasto-plastic compressible solid in the range 233-343 K. At the lowest temperature (203 K) all foams showed an elastic-brittle response, however the tendency towards a brittle response was more pronounced for foams of higher relative density.

Observations suggest that the sensitivity of the foams response to strain rate and temperature is principally governed by the inherent sensitivity of the parent polymer blend, with a minor effect of microstructural features and micro-inertia. The time-temperature superposition allowed mapping the strain rate sensitivity of the foams to the sensitivity of the response at different temperatures. A simple formula was also provided to give initial estimates of the foam stiffness as a function of temperature and relative density.

Chapter 6

Strain–Induced Anisotropy Effects

In previous chapters, experiments revealing the sensitivity of Rohacell foam to imposed strain rate and temperature, together with an understanding of the material response at microscopic length scales, were described.

In this chapter, the strain-induced anisotropic properties of Rohacell foams will be investigated, where the residual mechanical response of the pre-crushed material at different foam densities, and different loading directions, will be characterised. Cellular materials, which are generally integrated into composite sandwich structures, are used to their best potential under compressive loading, by absorbing and spreading the load through a combination of buckling and bending of cell walls. In the aerospace industry however, cellular materials are used in complex and unconventional design conditions, and are required to resist complex stress states. Upon handling, assembly or repair, these low density materials may be subjected to accidental loading, and during flight they may be subject to impact loading (e.g bird strike or ice impact), leading to significant crushing within the material. This leads to the material properties changing, upon application of strain. Engineers must

ensure they account for this in their design calculations. Research, however, is limited in this area and this chapter is focussed on quantifying this effect and filling the current gap in the literature.

6.1 Experimental Investigation

6.1.1 Specimen Preparation

The Rohacell material examined in this study was obtained from the same batch of material as that tested in the previous chapters and was in the form of large plates of thickness 55 mm and two different densities, namely 51 and 200 kg m^{-3}. Flat rectangular specimens measuring $100 \times 70 \times 55$ mm were machined out of the large plates using a milling machine, in such a way that the specimen's axis was aligned with the thickness direction of the foam plates. Uniaxial compression tests were then conducted at room temperature, whereby the specimens were loaded at a nominal strain rate of 10^{-3} s^{-1} by flat platens, lubricated with a PTFE spray. The load was applied by a screw-driven machine and measured with a resistive load cell. In this study, the material was crushed to 50% strain. Cross-head displacement was used for measuring axial strain. Figure 6-1 illustrates a block of Rohacell foam as it was crushed to 50% strain and the resulting stress-strain curve calculated from load-displacement readings off the test machine.

The crushed material was then left to stand for 24 hours, to allow for visco-elastic strain recovery. Once this was achieved, compressive and tensile specimens were cut out of the pre-crushed material. A schematic of the specimen preparation is shown in Figure 6-2.

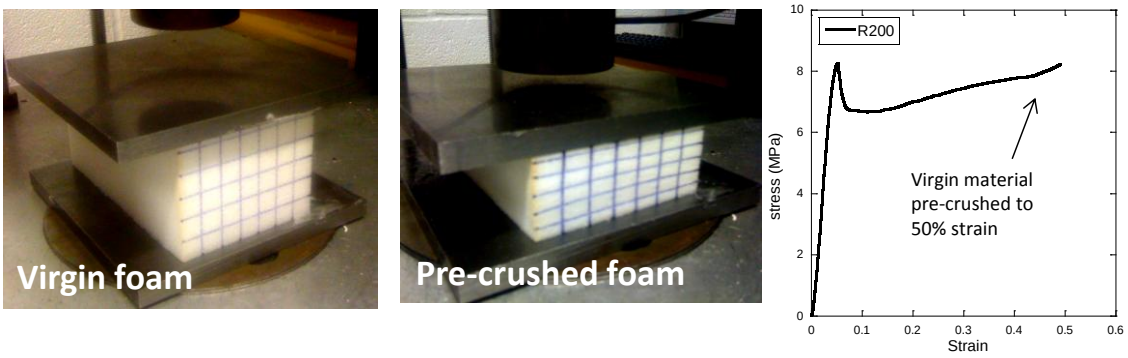


Figure 6-1: Block of Rohacell foam pre-crushed to 50% strain, and resulting stress-strain curve calculated from force-displacement readings off the Hounsfield machine

For the tensile tests, flat dogbone specimens with a gauge portion measuring $9 \times 5 \times 5$ mm (this choice was dictated by the constraints imposed by the block of Rohacell foam material available), and for the compression tests small prismatic blocks measuring $10 \times 5 \times 4$ mm were cut out of the pre-crushed Rohacell foam block, both in directions parallel (axial) and perpendicular (transverse) to initial crush.

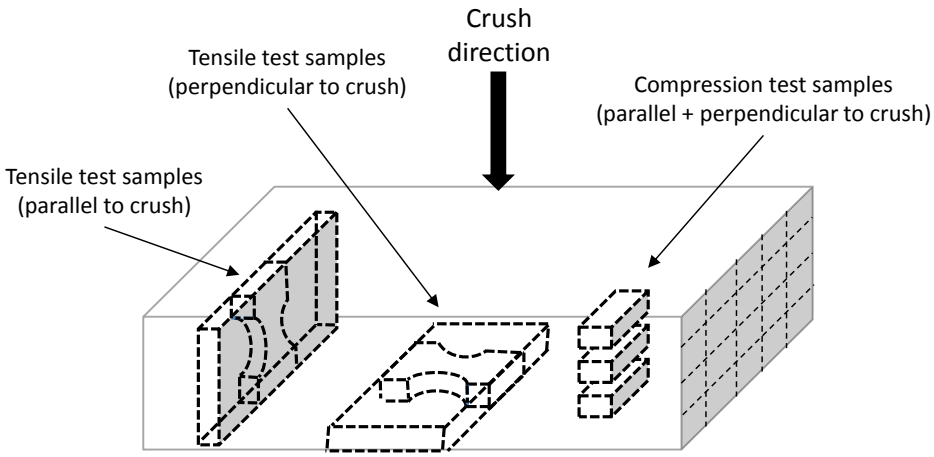


Figure 6-2 Schematic of specimen samples cut out of pre-crushed Rohacell foam

6.2 Experimental Results

6.2.1 Tensile Response, Parallel and Perpendicular to Crush

The tensile load was applied by a screw-driven machine and measured with a resistive load cell. The specimens were loaded at a nominal strain rate of 10^{-3} s^{-1} through end-grips connected to the test machine by a pin-joint in order to eliminate spurious bending moments. The tensile strain was measured by using image analysis techniques. The experiments in each test case were repeated a minimum of three times and the results were repeatable.

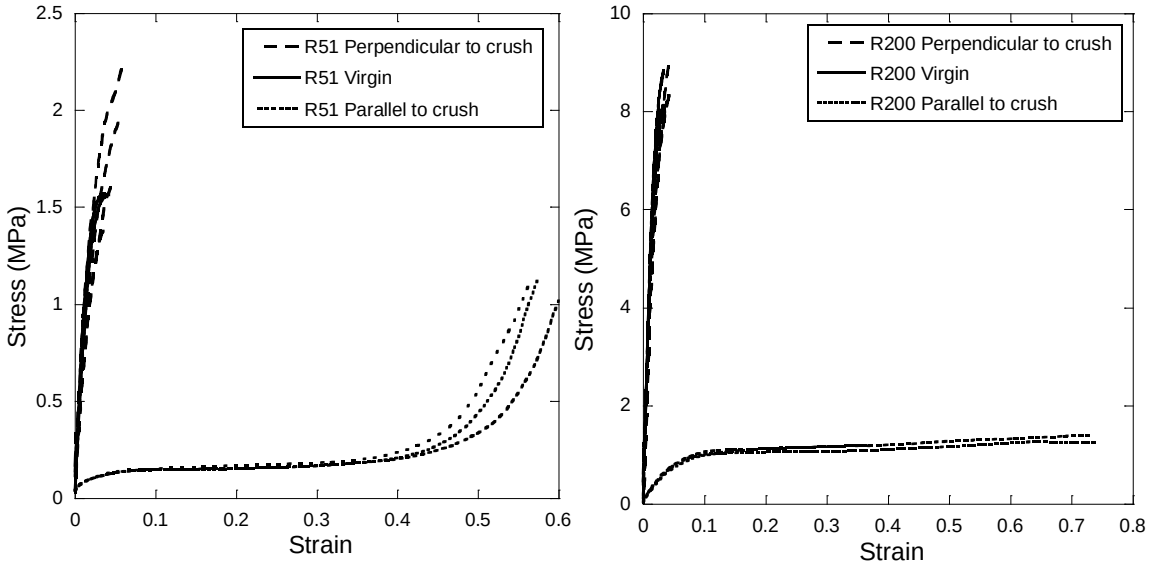


Figure 6-3: Tensile stress-strain curves for virgin & pre-crushed Rohacell foam (R51 & R200), conducted parallel (axial) and perpendicular (transverse) to initial crush (T=23°C, $\dot{\varepsilon} = 10^{-3}\ s^{-1}$).

Figure 6-3 presents the resulting three stress-strain curves measured from the tensile tests conducted on the pre-crushed foams, when loaded in the directions parallel (axial) and perpendicular (transverse) to initial crush. The tensile response of the virgin material is included for comparison.

For the virgin materials, brittle failure occurred at nominal strains of 2-3% by the propagation of a crack perpendicular to the loading direction. When tested in the transverse direction, R200 demonstrated tensile failure stress (σ_{Ft}) and strains (ε_{Ft}) greater than that of the virgin material. The effect was more pronounced for foam R51. When tested in the axial direction, both R51 and R200 exhibited a significant drop in tensile strength values, demonstrating a more ductile behaviour with much greater strains to failure. The stress-strain curves closely resemble typical compression curves, also reported by Koissin (2006), comprising a stress plateau region following the elastic response, followed by stress densification (in the case of R51). R200 failed in the stress-plateau region, prior to densification.

Material	Testing Direction	σ_{Ft} (MPa)	ε_{Ft}	E_t (MPa)	Specific σ_{Ft} (MPa.m³/kg)	Specific E_t (MPa.m³/kg)
R51 Virgin	-	1.58±0.01	0.04±0.005	68±0.8	0.03±0.0002	1.3±0.02
R51 (Post crush)	Transverse	1.9±0.2	0.06±0.009	50±6.2	0.02±0.002	0.45±0.05
	Axial	1.1±0.01	0.58±0.01	1.8±0.1	0.01±0.0001	0.02±0.0001
R200 Virgin	-	8.3±0.2	0.03±0.002	382±2.5	0.04±0.001	1.9±0.01
R200 (Post crush)	Transverse	8.5±0.3	0.04±0.001	326±3.2	0.02±0.001	0.8±0.008
	Axial	1.32±0.06	0.7±0.001	14±0.3	0.003±0.0001	0.03±0.001

Table 6-1: Average tensile material properties measured from the resulting stress-strain curves of Figure 6-3

Average material properties (includes mean ± standard error) measured from the stress-strain curves of Figure 6-3 are tabulated in Table 6-1. In this table, the specific strength (σ_{Ft}) and stiffness (E_t), defined as the ratio of the measured strength and stiffness to the foam density (original density for virgin

material and post-crush density for pre-crushed materials), has also been provided.

6.2.2 Compressive Response, Perpendicular to Crush

Uniaxial compression tests on pre-crushed materials were conducted at room temperature. The specimens were loaded at a nominal strain rate of 10^{-3} s^{-1} using flat platens, lubricated with a PTFE spray. The load was applied by a screw-driven machine and measured with a resistive load cell. Axial strain was measured using image analysis techniques. The Young's modulus (E_c) was measured as the initial slope of the stress-strain curve. The yield stress (σ_{Yc}) was defined as the measured stress at 0.2% plastic strain. The plateau stress (σ_{pl}) was measured as the average flow stress at nominal compressive strains between 0.1 and 0.5, and the densification strain (ε_D) was measured as the intersection of the tangents to the stress plateau regime and the densification regime.

Figure 6-4 compares the compressive response, perpendicular to the crushing direction, to that of the virgin material (for clarity only one curve per test case has been shown). It was found that the strength (yield and plateau stress) and stiffness of the pre-crushed R51 was comparable to that of the virgin material; however, densification occurred at much lower strains. In contrast, R200 demonstrated greater strengths compared to the virgin material, with the material showing signs of densification at lower strain levels.

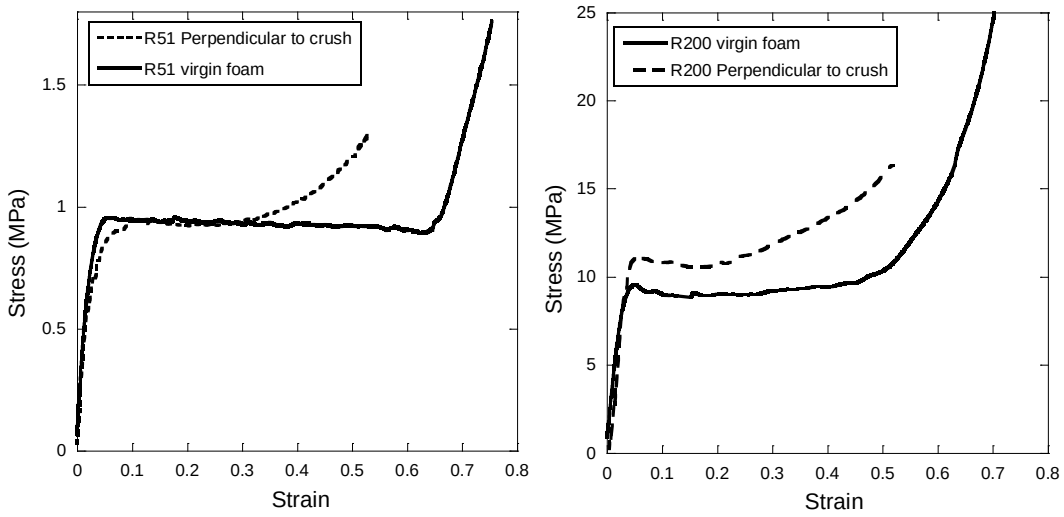


Figure 6-4: Compressive stress-strain results of virgin and pre-crushed transversely loaded R51 and R200 (T=23°C, $\dot{\varepsilon} = 10^{-3}\ s^{-1}$).

Average material properties (mean ± standard error) measured from the resulting stress-strain curves of Figure 6-4 are tabulated in Table 6-2, where the specific values have also been provided.

Material	Testing Direction	σ_{Yc} (MPa)	Specific σ_{Yc} (MPa.m³/kg)	σ_{pl} (MPa)	Specific σ_{pl} (MPa.m³/kg)	E_c (MPa)	Specific E_c (MPa.m³/kg)	ε_D
R51	Virgin	0.95±0.02	0.02±0.001	0.9±0.04	0.02±0.001	28.4±0.3	0.56±0.006	0.63±0.03
R51 (Post crush)	Transverse	0.94±0.02	0.01±0.001	0.9±0.03	0.01±0.001	26.3±2.7	0.26±0.025	0.42±0.04
R200	Virgin	10.9±0.14	0.05±0.001	8.9±0.3	0.05±0.002	281.9±6.3	1.41±0.032	0.56±0.04
R200 (Post crush)	Transverse	9.1±0.43	0.03±0.001	12.3±0.5	0.03±0.001	249.8±31	0.62±0.08	0.27±0.03

Table 6-2: Average material properties measured from the resulting stress-strain curves of Figure 6-4

6.2.3 Normalised Specific Residual Strength and Stiffness

A graphical representation of the residual specific stiffness of pre-crushed Rohacell foam, relative to that of the virgin material is presented in Figure 6-5. The figure illustrates both tensile (shown as positive values on the graph) and compressive (shown as negative values on the graph) test results.

From Figure 6-5 it is clearly seen that pre-crushing has a detrimental effect on the specific residual stiffness of Rohacell foam, for axial and transverse, compressive and tensile loading. Under transverse tensile loading, the specific stiffness of R51 and R200 is seen to drop by 64% and 58%, respectively. Upon axial tensile loading, the specific stiffness drops significantly, approximately 99% for R51 and R200, relative to the virgin material. Under axial compressive loading, R51 and R200 demonstrate a 50% drop in specific stiffness values. Under transverse compressive loading, R51 and R200 demonstrate a 54% and 56% drop in specific stiffness values.

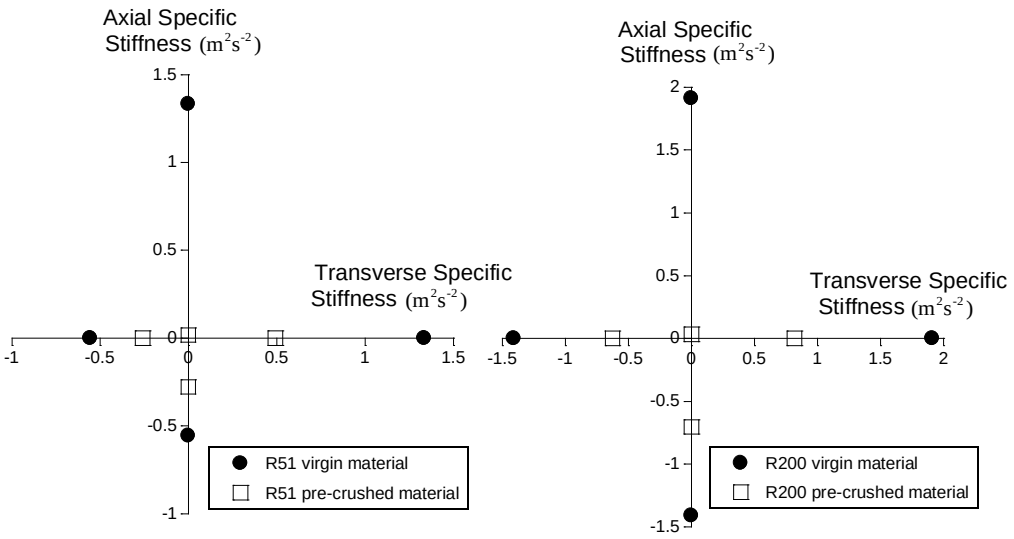


Figure 6-5: Specific residual foam stiffness at 50% pre-crushed strain, for foams R51 (left) and R200 (right), relative to the virgin material, in axial and transverse directions (T=23°C, $\dot{\varepsilon} = 10^{-3}\, s^{-1}$*).*

Figure 6-6 illustrates the specific residual strengths of R51 and R200, in the axial and transverse directions, relative to that of the virgin material. At 50% pre-crushed strain, under transverse tensile loading, the specific strengths of R51 and R200 drop by 40% and 50%, respectively. Upon axial tensile loading the specific residual strength of the pre-crushed material drops by an even

greater amount, with R51 dropping by 65% and R200 by 92%, relative to the virgin material. At 50% pre-crushed strain, under transverse compressive loading, R51 and R200 demonstrate a 51% and 43% drop in specific strength values, respectively. Under axial compressive loading, R51 and R200 show a 50% drop in specific strength values.

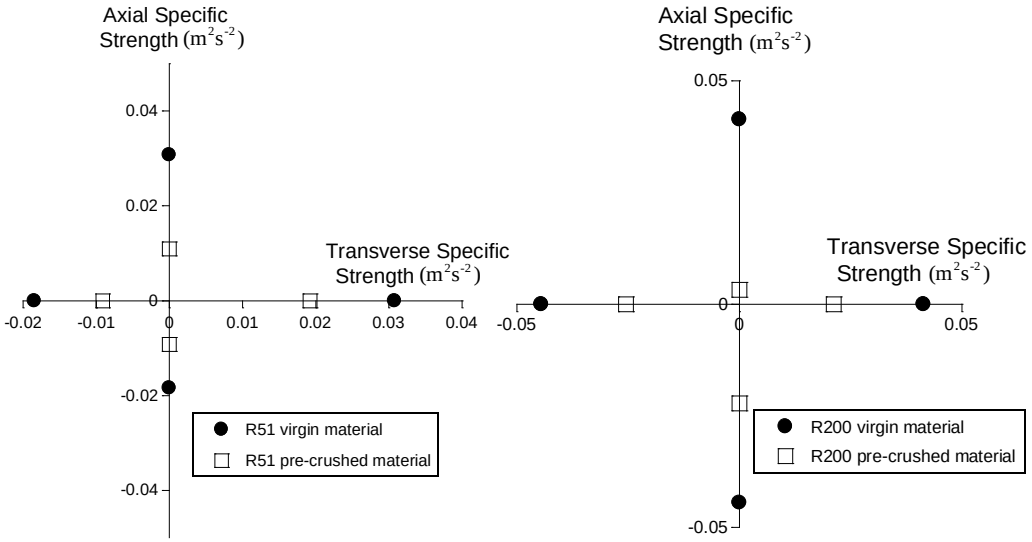


Figure 6-6: Specific residual foam strength at 50% pre-crushed strain, for foams R51 (left) and R200 (right), relative to the virgin material, in axial and transverse directions (T=23°C, $\dot{\varepsilon} = 10^{-3}\, s^{-1}$*).*

6.2.4 Discussion

The data generated in this chapter supplements the limited data currently found in the literature on the pre-crush properties of Rohacell foams of different densities. It has been shown that pre-crushed Rohacell foams exhibit strain-induced anisotropic properties, where the mechanical response of the material varies in different loading directions.

In this study, and similar to the findings of Li *et al.* (2000), the tensile stress-strain curves of pre-crushed R51, when loaded in the axial direction, resembled typical compressive curves, i.e. the three typical regions of elastic, stress plateau and densification were observed. In contrast, R200 only followed the elastic and stress plateau behaviour of a compressive stress-strain curve, and was seen to fail prior to densification. Upon tensile loading of the pre-crushed material, the buckled cell-edges which initially lie at an angle to the tensile axis now rotate towards this axis. The elastic response is initially dominated by cell-edge unfolding, but as the cell walls rotate towards the tensile axis, this change in geometry gives rise to structure stiffness. Upon further loading, as the edges become more aligned, stretching, rather than bending, dominates the deformation. This behaviour is more pronounced for R51. R200 exhibits a more brittle-like behaviour with brittle fracture occurring during unbuckling of the thicker cell walls, prior to stretching, by the fast propagation of a single crack within the thick cell walls of the material. Figure 6-7 illustrates the deformation behaviour of pre-crushed R200 (shown on top) and R51 (shown below) under tensile loading.

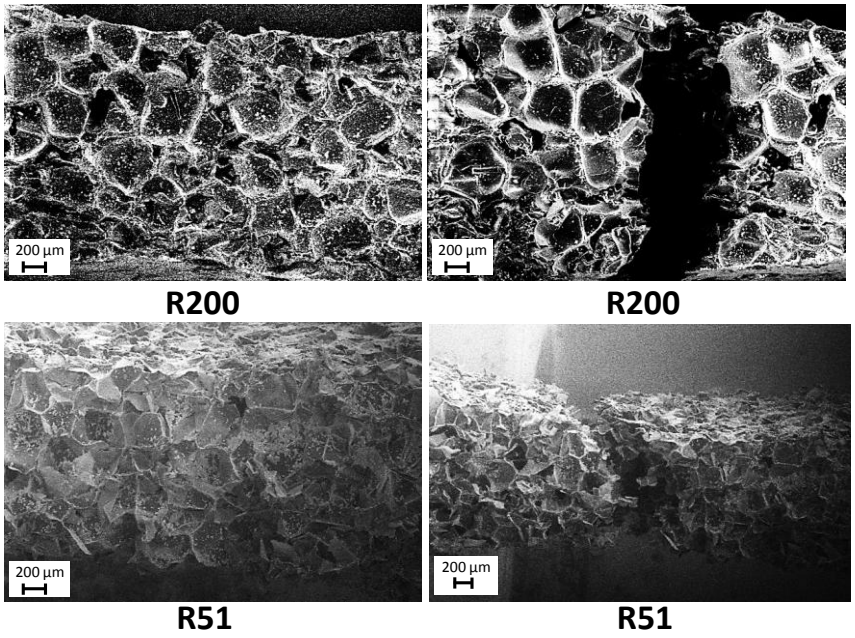


Figure 6-7: Deformation behaviour of pre-crushed R200 (top) and R51 (bottom) under transverse tensile loading

The experimental results in this study revealed that pre-crushed R51 demonstrated greater residual strengths in tension than in compression when loaded in the transverse direction. In contrast, pre-crushed R200 demonstrated greater residual strengths in compression than in tension. This tension/compression asymmetry of the strength of the material is similar to that observed in the virgin material, as reported in Chapter 4, where ESEM observations were used to understand this asymmetry by observing different microscopic deformation mechanisms occurring during in-situ compression and tensile tests. In particular, a combination of elastic buckling and plastic bending of the cell walls of R51 and plastic cell-wall bending of R200 appeared to be the main reason for the tension/compression asymmetry. It would appear that similar trends are present when residual properties are considered.

The tension/compression asymmetry of the moduli and strengths, and the strain-induced anisotropic properties of Rohacell foams are important

findings which are often neglected in the literature. As foam materials are generally used to their best potential under compressive loading, compressive properties are typically reported. Numerical models generally require a single moduli and strength parameter to predict foam behaviour, where the user is expected to input compressive values, assume these values remain unchanged, and use similar values in tension. A simple test method which can be used to demonstrate how results can be over or under-estimated, if unequal moduli in tension and compression, and strain-induced anisotropy in foams, is not considered, is the three-point-bend test.

Due to the simplicity of specimen preparation and testing, and ease of analysis, the three-point-bend test is used extensively in material characterisation. In addition, the three-point-bend test is a simple way to subject a specimen to tension, compression and shear simultaneously.

The three-point-bend experiments were performed on the virgin and pre-crushed foam material. The work of Chamis (1974) provides simple beam formulas for materials with unequal tensile and compressive stiffness or strength, which were used herein to predict the three-point-bending response.

6.3 Three-Point-Bend Experiments

6.3.1 Experimental Apparatus and Specimen Preparation

Three-point-bend experiments were performed on virgin and pre-crushed (to 50% strain) R51 and R200 foams. Prismatic specimens measuring 200x80x10 mm for R200 foam and 200x80x15 mm for R51 foam were cut from pre-crushed foam blocks. An illustration of the 3-point bend apparatus is shown in Figure 6-8.



Figure 6-8: Three-point-beam bending apparatus, R51 pre-crushed specimen shown prior to failure (left image) & post failure (right image)

A steel roller measuring 15mm in diameter was positioned central to the beam of span 185 mm. The load was applied by a screw-driven machine and measured with a resistive load cell. The test samples were loaded at a cross-head speed of 2 mm/min. The machine compliance was measured and seen to be negligible (the rig contributes ~0.035mm to a beam displacement of 30mm); hence, the crosshead displacement was used for measuring the mid-span deflection.

6.3.2 Three-Point-Bend Test Results

All tests were replicated a minimum of three times and it was found that the measured force versus displacement response was repeatable. Results are presented in Figure 6-9. For clarity only two curves per test case are plotted and scatter is reported in Table 6-3. The material behaviour comprised an elastic response, followed by a non-linear response indicating plasticity. The non-linearity was more pronounced for the pre-crushed foams.

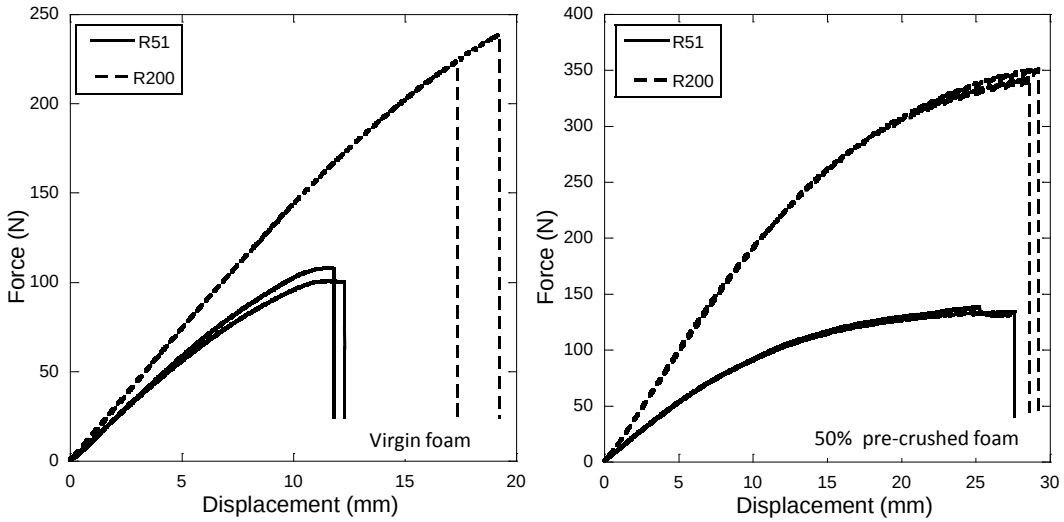


Figure 6-9: Force versus displacement 3-point-bend test results of R51 and R200, in their virgin (left) and pre-crushed (right) state.

Average measured mechanical properties (mean ± standard error) are reported in Table 6-3. The table includes values of the yield force (defined as the tangent force at 0.2 mm displacement), the displacement at the yield point and the force and displacement at the point of material failure.

Mechanical Properties	R51		R200	
	Virgin	50% pre-crush	Virgin	50% pre-crush
Yield Force (N)	65.3±4.1	64±2.8	166±6.7	202±9.2
Yield Displacement (mm)	7±0.3	9±0.3	12±0.54	12±0.53
Failure Force (N)	104±2	135±2	232±5.3	346±3.5
Failure Displacement (mm)	12±0.14	26±0.64	18.25±0.7	29±0.36

Table 6-3: Measured average 3-point-bend properties

6.3.3 Three-Point-Bend Test Predictions

In this section, we proceed to predict the three-point-bending response. Predictions are based on the work of Chamis (1974), on beams made from materials displaying tension/compression asymmetry in stiffness and strength. The following equations and relations were used to develop the theory used herein. Only the final equations are given and the detailed derivations can be found in Chamis (1974). For a material with different moduli in tension and compression:

$$\sigma_T = \varepsilon_T E_T, \qquad [6\text{-}1]$$

and

$$\sigma_C = \varepsilon_C E_C, \qquad [6\text{-}2]$$

where the subscripts T and C denote tension and compression, respectively. The force equilibrium equation at a point (x, z) in a beam is given by

$$\frac{d\sigma}{dx} - \frac{d\tau}{dz} = 0, \qquad [6\text{-}3]$$

where σ and τ denote normal and shear stress, respectively and $0 \le x \le L$ and $h_b \le z \le h_t$ (refer to Figure 6-10). The resultant force at a section x is given by

$$\int_{-h_b}^{0} \sigma_T dz + \int_{0}^{h_t} \sigma_C dz = 0, \qquad [6\text{-}4]$$

where h_b is measured from the neutral plane to the bottom of the beam and h_t to the top.

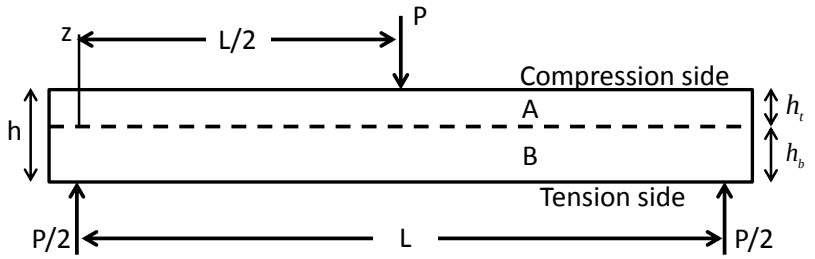


Figure 6-10: Schematic of geometry of three-point-bend test specimen from material with unequal tensile and compressive properties.

The resulting moment at a section x is given by

$$M = b\int_{-h_b}^{0} \sigma_t z dz + b\int_{0}^{h_t} \sigma_c z dz, \qquad [6\text{-}5]$$

where b is the beam width. The location of the neutral plane (plane of zero bending stress) is given by:

$$\frac{h_t}{h_b} = \left(\frac{E_T}{E_C}\right)^{1/2} \qquad [6\text{-}6]$$

$$h_b = \frac{h}{[1+(\frac{E_T}{E_C})^{1/2}]} \qquad [6\text{-}7]$$

where h is the beam thickness. The bending stiffness, D, also known as bending rigidity or flexural rigidity, is given by

$$D = \frac{b}{3}(h_b{}^3 E_T + h_t{}^3 E_C). \qquad [6\text{-}8]$$

Equation [6-8] can also be written as

$$D = \frac{1}{3} b h h_b^{\,2} E_T, \text{ or } D = \frac{1}{3} b h h_t^{\,2} E_C. \qquad \textit{[6-9]}$$

Maximum flexural Deflection

The equation for computing the maximum bending deflection (deflection at mid-point) is given by

$$w_{\max} = \frac{PL^3}{48D}[1 + 1.6 b h_b^{\,2} h \frac{E_T^{\,2}}{GD} (\frac{h_b}{L})^2], \qquad \textit{[6-10]}$$

where P is the load, L is the length, and G is the shear modulus. In this study $(\frac{h_b}{L})^2 = 0.001$, and hence the second term of equation [6-10] is very small and can be assumed negligible. Equation [6-10] can be used to determine the slope of the load vs. bending deflection curve as:

$$P = \frac{48D}{L^3} w_{\max} \qquad \textit{[6-11]}$$

For the case where $E_T = E_C,\ h_b = h_t = (h/2),$ equation [6-10] reduces to:

$$w_{F\max} = \frac{PL^3}{4bh^3(E_T \text{or} E_C)} \Rightarrow P = \frac{4bh^3(E_T \text{or} E_C)}{L^3} w_{F\max}, \qquad \textit{[6-12]}$$

where the variable $w_{F\max}$ is the flexural deflection for no shear contribution and the coefficient of $w_{F\max}$ is the slope of the load-deflection curve, when the tensile and compressive moduli are assumed equal.

The measured slope from the force-displacement curves of Figure 6-9 versus the predicted slopes from equation [6-11] (assumes unequal moduli) and equation [6-12] (assumes equal moduli), for foams R51 and R200, in their virgin and pre-crushed state were compared in Figure 6-11.

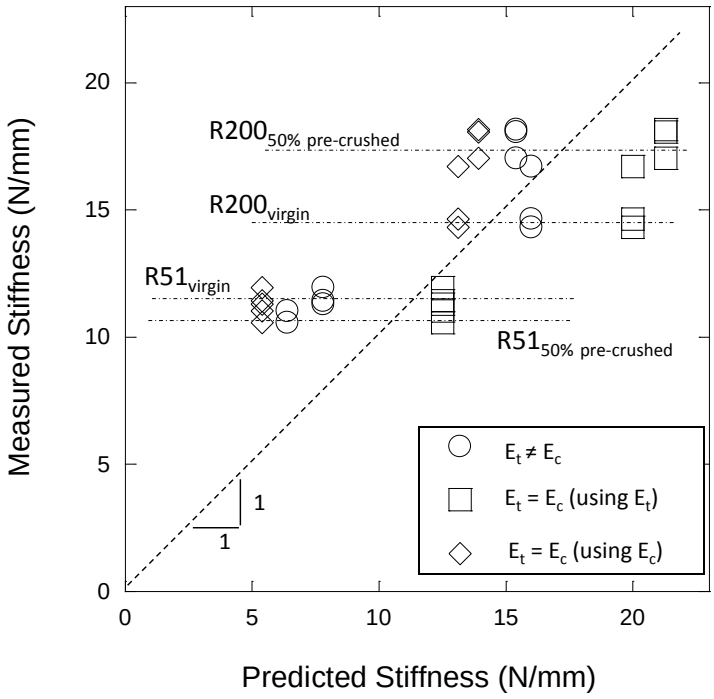


Figure 6-11: Measured versus predicted stiffness (slope), using equation [6-11] (assumes unequal moduli) and equation [6-12] (assumes equal moduli).

A graphical representation of Figure 6-11 is presented in Figure 6-12, where the force-displacement histories of the three-point-bend experiments are also provided. The predicted slope AB is calculated using equation [6-11], assuming unequal moduli, and anisotropic properties for the pre-crushed material. The predicted slopes ED and CD are calculated using equation [6-12], assuming equal moduli and isotropic properties for the pre-crushed material, where the subscripts t and c refer to tensile and compressive properties, respectively.

For foams R51 and R200, in their virgin state, it is shown that stiffness measurements can be under or over-estimated when equal moduli is assumed. The predicted stiffness using unequal moduli are in closer agreement to the measured stiffness, although R51 results demonstrate that when equal moduli

using the tensile modulus is assumed, the predicted slope is in closer agreement to the measured values.

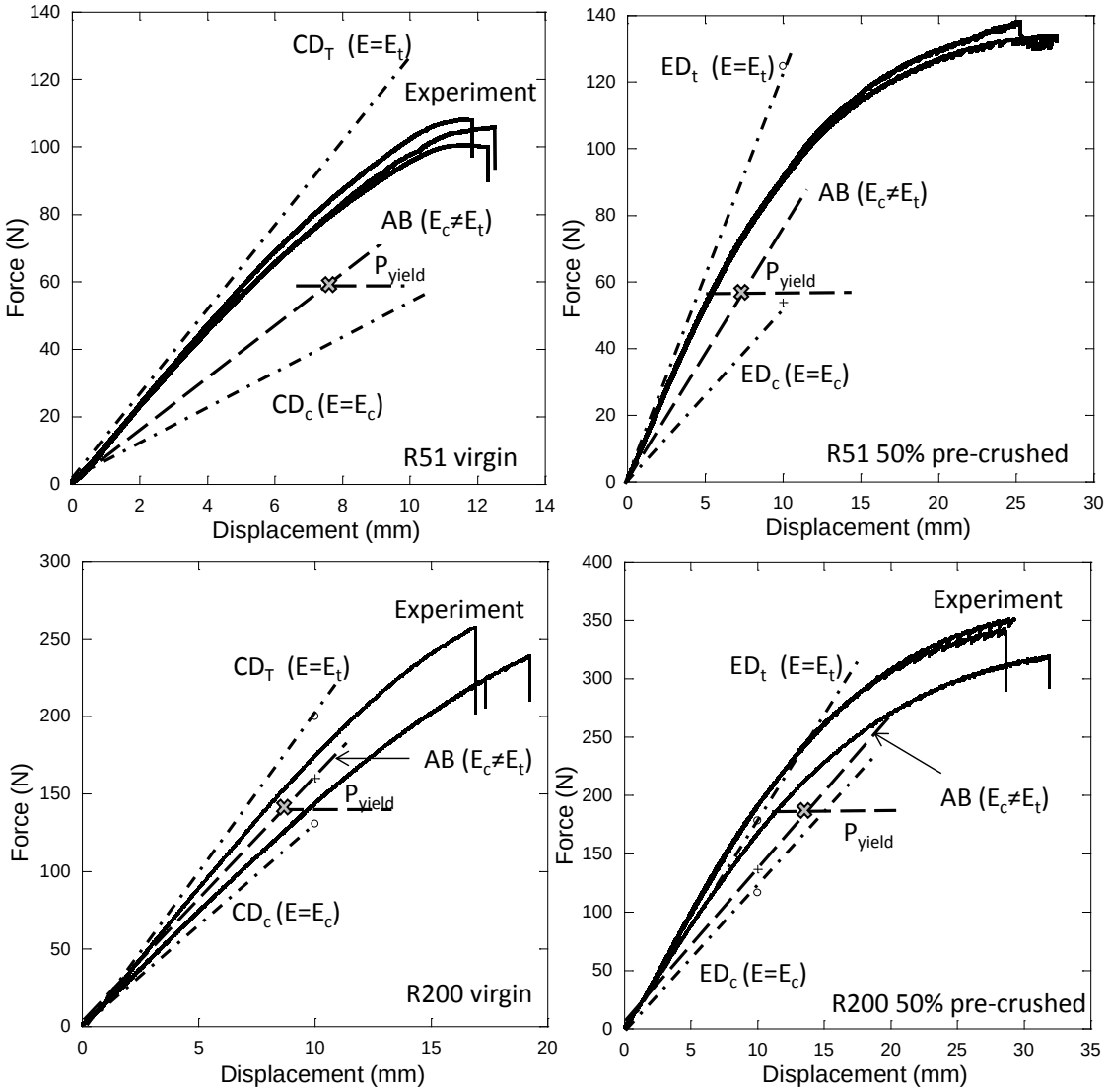


Figure 6-12: A graphical representation of the predicted slope and yield load, showing how values can be over or under-estimated if unequal moduli or anisotropic properties are not taken into account.

Chamis (1974) reported that the maximum flexural deflection is sensitive to the modular ratio, defined as the tensile-modulus to compressive-modulus ratio. In his work, when this value exceeded 1.5, the simple beam formulas were shown to underestimate the maximum deflection by 25% or more. The

modular ratio of R51 in its virgin and pre-crushed state is 2.3 and 2.0 respectively; hence, the under-estimated predictions using unequal moduli could be due to the sensitivity of the results to the higher modular ratio of R51. The modular ratio of R200 in its virgin and pre-crushed state is 1.5 and 1.2 respectively, and it is seen that the predicted slope (using un-equal moduli) is in close agreement with the measured slope. In addition the stiffness measurements will be very sensitive to any misalignment and to the initial contact with the loading roller. This sensitivity would be more pronounced for foams of lower relative density.

Maximum Flexural stresses

The maximum bending tensile ($\sigma_{T\max}$) and compressive ($\sigma_{C\max}$) stress occurs at $x = L/2$ and $z = -h_b$, and $x = L/2$ and $z = h_t$, respectively. They are given by:

$$\sigma_{T\max} = PLh_b \frac{E_T}{4D} \text{ and } \sigma_{C\max} = -PLh_t \frac{E_C}{4D} \qquad [6\text{-}13]$$

Using the top two equations, the load at the start of yield in tension (P_{Yt}) and compression (P_{Yc}) is given by:

$$P_{Yt} = \frac{\sigma_{T\max}.4D}{Lh_b.E_T} \text{ and } P_{Yc} = \frac{-\sigma_{C\max}.4D}{Lh_t.E_C} \qquad [6\text{-}14]$$

If the strain-induced anisotropic properties of the pre-crushed materials were not considered (i.e. only the virgin material properties were used), it can be shown that predictions of the yield load for pre-crushed R51 and R200 can be over or under-estimated, as shown in Figure 6-13. In this figure it is shown that when the strain-induced anisotropic material properties for the pre-crushed

foam material is taken into account, the yield load predictions (using either compression or tension properties) are in closer agreement to the measured yield load from the three-point-bend tests. These predictions demonstrate that by neglecting the change in material properties of pre-crushed materials, numerical predictions can be over or under-estimated. The minimum of the absolute values of the predicted yield loads calculated using equation [6-14] are graphically represented in Figure 6-12, as an intersecting point on slope AB. The predictions demonstrate that in all but one test case (R51, 50% pre-crushed) the material appears to fail in tension prior to compression.

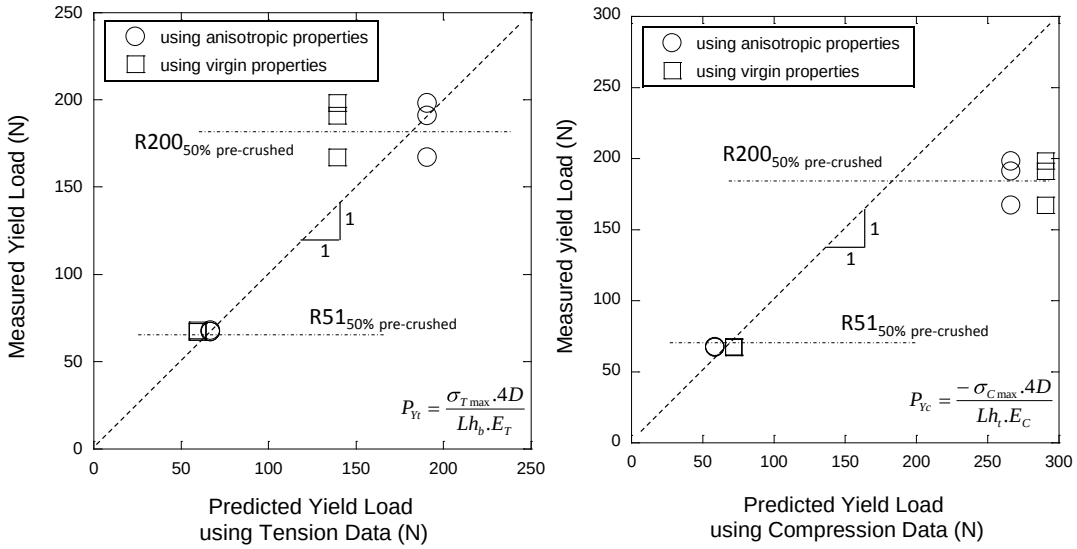


Figure 6-13: Measured versus predicted yield load, using equation [6-14], for pre-crushed R51 and R200, where virgin and strain-induced anisotropic properties are considered

In Table 6-4 a summary of the specimen geometry and material data used to derive the equations provided in the study above is given.

3-point-bend-beam measurements	Notation	R51 Virgin Material	R200 Virgin Material	R51 50% pre-crushed	R200 50% pre-crushed
Span Length (mm)	L	185	185	185	185
Beam Width (mm)	b	77	76	77	81
Beam Thickness (mm)	h	15	10	15	10
Tensile Modulus (MPa)	E_T	76	417	57	326
Compressive Modulus (MPa)	E_C	33	272	28	280
Bending Stiffness (MPa)	D	1034904	2108816	838408	2036403
Force-Displacement slope (N/mm)		12	15	11	18
Yield Load (N)	P	65	166	64	202

Table 6-4: Specimen geometry and material properties derived from the equations provided above

6.3.4 Stiffness and Strength Predictions of Pre-crushed Material

From the study conducted above, it was found that the slope and yield load of the three-point-bend force-displacement results could be predicted using measured data from the virgin and pre-crushed Rohacell foams. Equally, it can be demonstrated that material data from virgin and pre-crushed material can be extrapolated to predict the strength and stiffness of the material, pre-crushed to any value of strain, as discussed below.

The specific residual tensile strength and stiffness of R51 and R200 pre-crushed to 50% strain, normalised to that of the virgin material is shown in Figure 6-14 (this figure is analogous to the graphical representation presented in Figure 6-5; the compressive data has not been shown, but can be similarly presented). The data from Figure 6-14 was interpolated to obtain residual strength and stiffness properties of the foam material at 25% pre-crushed strain.

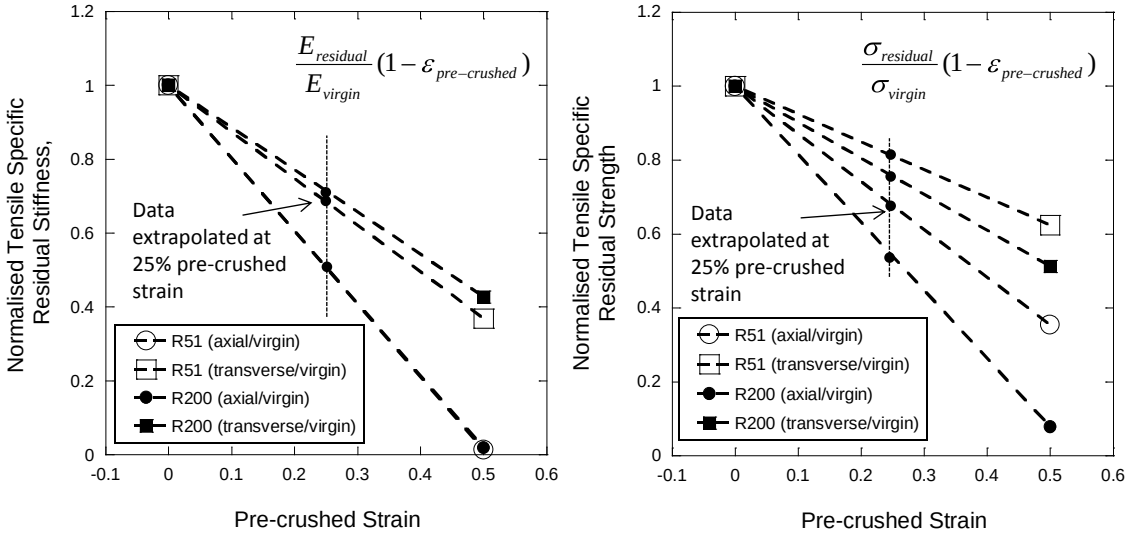


Figure 6-14: Normalised specific tensile residual foam stiffness (left) and strength (right) with respect to that of the virgin material, at 0 and 50% pre-crushed strain for R51 and R200

A series of three-point-bend tests were repeated on R51 and R200 foam material pre-crushed to 25% strain. By using equation [6-11], i.e. $P = \frac{48D}{L^3} w_{\max}$ and the interpolated data from Figure 6-14, the slope (AB) of the three-point-bend force-displacement graph was predicted (see Figure 6-15). Similarly, slope ED was also predicted using equation [6-12], i.e. $P = \frac{4bh^3(E_T \text{or} E_C)}{L^3} w_{F\max}$ using equal moduli and virgin material properties, and it was found that the predicted slope using unequal moduli and pre-crushed foam properties lies between those predicted for equal moduli and virgin properties.

Equation [6-13], i.e. $\sigma_{\max} = PLh_b \frac{E}{4D}$ was used to determine the yield stress of the 25% pre-crushed material, where the value of the yield load (P) was directly measured off the three-point-bend force-displacement graph (measured at 0.2mm displacement offset). The tensile and compressive yield stress of R51 and R200, pre-crushed to 25% strain, using the three-point-bend

measurements and equation [6-13] was measured as 1.6 and 9.2 MPa, respectively.

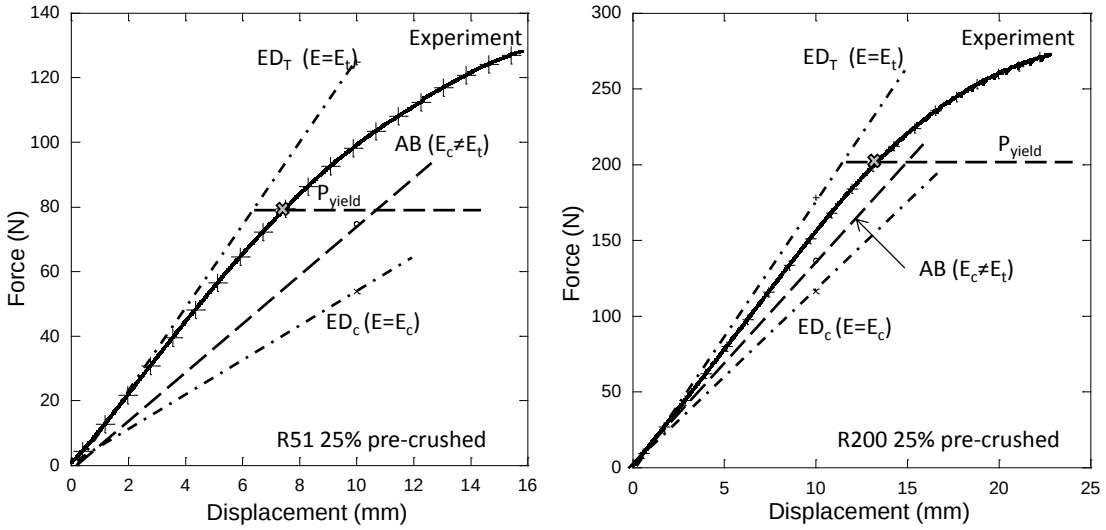


Figure 6-15: Three-point-bend force-displacement results of R51 and R200 pre-crushed to 25% strain. The predicted slope AB using unequal moduli and anisotropic properties lies between the slope predictions using equal and virgin properties.

6.4 Conclusions

In this chapter, the tensile and compressive mechanical properties of pre-crushed Rohacell foam of low and high foam densities were measured. The results demonstrated that pre-crushing has a detrimental effect on the strength and stiffness of the foam, with specific residual properties dropping significantly, relative to the un-crushed virgin material. In addition, similar to that observed for the virgin material, a tension/compression asymmetry of the residual strength of the pre-crushed material was observed. The data generated supplements the limited data currently found in the literature, and will help designers account for the effect of pre-crushing in their design calculations.

In the latter part of this chapter a series of three-point-bend experiments were performed on virgin and pre-crushed foam material, at low and high foam densities. It was found that either neglecting the foams tension/compression asymmetry, or the changes in stiffness and strength due to pre-crushing, leads to incorrect predictions of the foams structural response. Predicted results which take into account tension/compression asymmetry and strain-induced anisotropic properties, lie within the region bound by the predicted behaviour when the aforementioned effects are not taken into account.

Current Finite Element foam material models do not account for the tension/compression asymmetry, or the strain-induced anisotropic material properties observed in this study; hence, extreme care must be taken when using these material models under complex loading conditions. A detailed analysis of the relative influence of the tension/compression asymmetry or the changes occurring in the material under applied strain, on FE predictions, is

beyond the scope of this study. However, in the following chapter the capability of existing FE material models for predicting the foam response under complex loading will be addressed, and the shortfalls and recommendations for further improvement will be discussed.

Chapter 7

Macroscopic Numerical Modelling

Due to the highly non-linear behaviour of closed cell polymer foams, uniaxial mechanical properties are not always sufficient for predicting the complex in-service loading conditions the material is subjected to. Indentation tests on the other hand allow the user to explore the response of foams to a tri-axial state of stress, and can provide nonlinear material parameters which aid in material development and product design.

The use of numerical finite element codes to simulate the mechanical response of cellular structures largely depends on the accuracy and efficiency of the applied material models. Numerical simulation of cellular structures is inherently an approximation, as the foam cell structure is generally modelled as a 3D-continuum using Finite Element solid brick elements, with a material law which is only capable of predicting the macroscopic foam response. The constitutive model selected for modelling the foam response must be capable of producing a stable and efficient numerical solution for large strains and displacements. However, in order to achieve the most efficient numerical

solution procedure, one must be prepared to sacrifice the accuracy of the constitutive model, going instead for a more simplified configuration.

In this chapter, results from a series of indentation experiments are presented and used to validate some existing constitutive models for foam materials. The comprehensive experimental database obtained in Chapters 4 and 5 will be used to specify the input parameters of the chosen material models. It must be noted it is not the intent of this study to investigate the theory behind each material model, it is only intended to demonstrate the capability of existing foam models for predicting the response under complex loading, identify the shortfalls, and provide recommendations towards improving the existing models.

7.1 Experiments

7.1.1 Indentation Experiment

In Chapter 4, in order to explore the response of the foam to a tri-axial state of stress, indentation tests were performed. The indentation load was applied through a steel spherical indenter, using a ball bearing of radius 12.5 mm.

The measured indentation force versus displacement curves are presented in Figure 7-1. The load increased linearly with displacement up to an indentation depth of approximately 7 mm. At this depth, brittle cracking of the foam occurred for all densities, and the ensuing load/displacement response became non-linear. Observations subsequent to the tests confirmed that the foam had undergone fracture under the indenter.

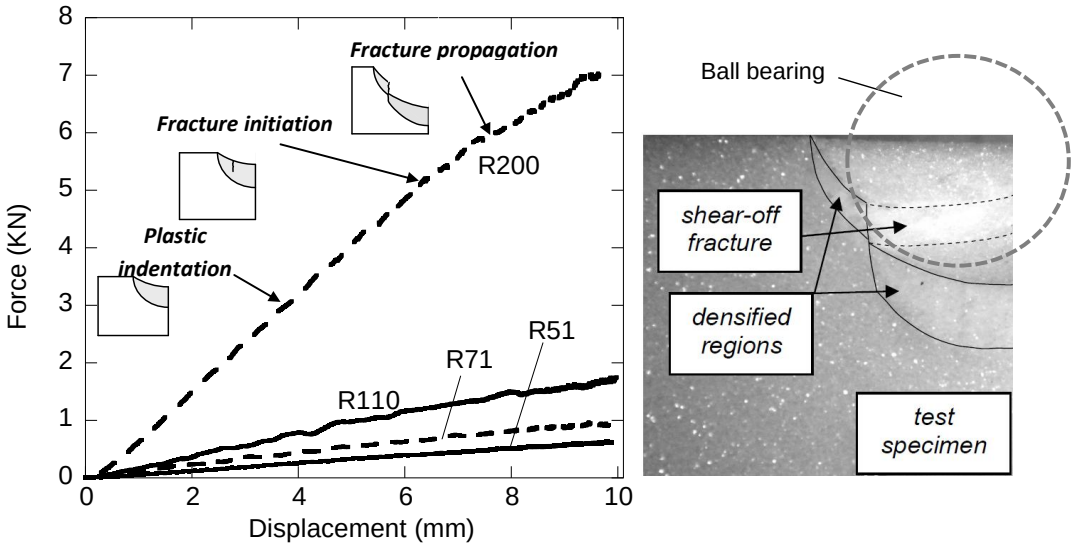


Figure 7-1: Measured indentation force versus displacement response for the four foam densities. An illustration of the indentation test is shown on the right.

The measured indentation response and microscope observation of the indentation specimens revealed that fracture occurred at similar indentation depths (and therefore at similar strains) for all foams investigated, and cracks were seen to initiate in the region of densified foam under the indenter. In this region, the foams have acquired a locally anisotropic response due to strain-induced changes in their microstructure.

To assess the capability of current Finite Element models in predicting the foam response under tri-axial loading, a study was conducted using an applicable material model in both ABAQUS and LS-DYNA.

7.2 Finite Element Simulations & Results

7.2.1 ABAQUS (Mat Crushable Foam)

The commercial software ABAQUS Standard[1] was used to perform Implicit, non-linear FE simulations of the indentation experiments, for the purpose of comparison of numerical results with experimental evidence. Due to the large size of specimens employed in the indentation tests, the measured load versus displacement response was independent of the specimen size. As a consequence, the geometry of the indented foam blocks was not modelled explicitly but an axisymmetric calculation was set-up, by modelling the foam blocks as circular cylinders of diameter 300 mm and height 50 mm.

Four-node linear axisymmetric quadrilateral elements were used (the CAX4 elements of ABAQUS) and a typical mesh comprised 5000 elements. All degrees of freedom of the nodes on the lower face of the foam cylinder were constrained. The indenter, of diameter 25 mm, was modelled as an analytical, axisymmetric rigid body. All translations and rotations of the indenter were constrained, with the exception of the translation in the direction normal to the foam cylinder; an indentation displacement of 10 mm was imposed in this direction. Frictionless contact was imposed at the foam/indenter interface.

The foams were modelled using the *crushable foam* model of ABAQUS (Deshpande & Fleck 2000). This model is based on a quadratic yield surface in the Von Mises – hydrostatic stress space. Based on experimental evidence, the plastic Poisson's ratio was assumed to be zero, isotropic strain hardening was assumed, and the measured compressive response of the foams was used to

[1] Hibbit, Karlsson and Sorensen Inc.

calibrate the model. A rate-insensitive version of the model was used to perform these calculations, and a fracture/damage criterion was not included. For all foam densities, the FE simulations predicted an indentation response characterised by negligible pile-up or sink-in; this is in line with experimental observations (see Figure 7-2).

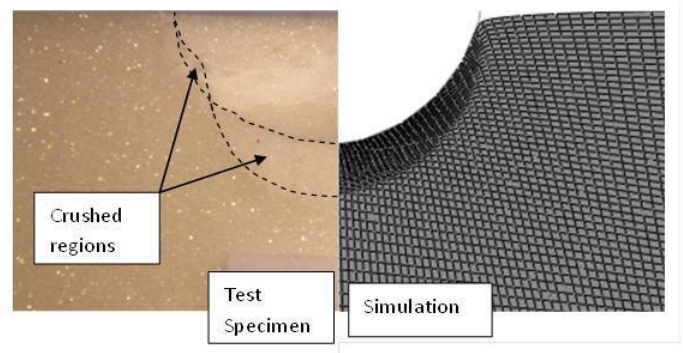


Figure 7-2: Indentation experiment vs. numerical modelling (Abaqus) simulation

Figure 7-3 shows that the predicted load/displacement response is in excellent agreement with the measured response for indentation depths below 7 mm. Recall that at depths around 7 mm fracture phenomena were observed in the experiments and as a result the FE calculations, which do not account for fracture events, over-predict the load for indentation depths beyond 7 mm.

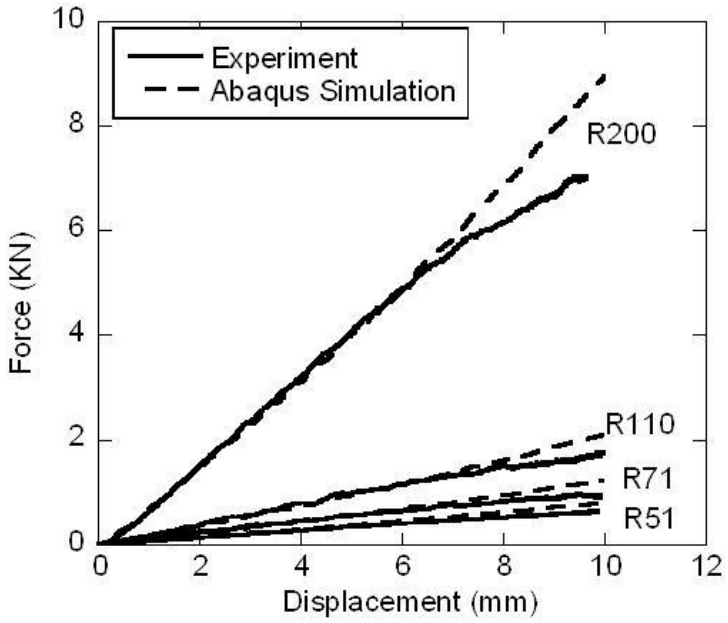


Figure 7-3: ABAQUS simulation vs. experimental indentation response

The model employed (Deshpande & Fleck 2000) is capable of capturing the elasto-plastic quasi-static response of Rohacell WF foams of different densities; however, due to a lack of a fracture criterion, it is unable to capture the post-peak load response once fracture starts to occur. Fracture and damage criteria need to be developed to model the mechanical response of these brittle foams.

There are several FE foam material models available in LS-DYNA[2], which encompass failure criterions; thus, the crushable foam material model is investigated in the following section.

7.2.2 LS-DYNA (Mat Crushable Foam)

Reyes *et al.* (2003) implemented the Deshpande and Fleck foam (Deshpande & Fleck 2000) material model in LS-DYNA as **MAT_154*. The yield function is defined as:

[2] Livermore Software Technology Corporation (LSTC)

$$\phi = \hat{\sigma} - Y \leq 0, \qquad [7\text{-}1]$$

where the yield stress Y is expressed as:

$$Y = \sigma_p + R(\hat{\varepsilon}), \qquad [7\text{-}2]$$

where σ_p is the foam plateau stress, $R(\hat{\varepsilon})$ represents the strain hardening and $\hat{\varepsilon}$ is the equivalent strain. Deshpande and Fleck define the equivalent stress $\hat{\sigma}$ as:

$$\hat{\sigma}^2 = \frac{1}{[1+(\alpha/3)^2]}[\sigma_e{}^2 + \alpha^2 \sigma_m{}^2], \qquad [7\text{-}3]$$

where σ_e is the Von Mises effective stress, σ_m is the mean stress, and the parameter α defines the shape of the yield surface as:

$$\alpha^2 = \frac{9(1-2\upsilon^p)}{2(1+\upsilon^p)}, \qquad [7\text{-}4]$$

where υ^p is the plastic coefficient of contraction. From the uniaxial compression tests negligible lateral plastic deformation was seen, hence, a zero plastic poisson ratio was assumed, resulting in α^2=4.5.

The yield stress Y is given as:

$$Y = \sigma_p + \gamma \frac{\hat{\varepsilon}}{\varepsilon_D} + \alpha_2 \ln\left(\frac{1}{1-\left(\frac{\hat{\varepsilon}}{\varepsilon_D}\right)^\beta}\right). \qquad [7\text{-}5]$$

The first term represents the start of the stress plateau region σ_p once the elastic region has been traversed. The second term is a linear strain-hardening function, which includes γ as a coefficient used to define the slope of

the stress-strain curve and a strain hardening term which involves an equivalent strain $\hat{\varepsilon}$ to densification strain ε_D ratio. The third term represents the non-linear strain hardening term defined by material parameters α_2 and β and again the strain hardening ratio. The material parameters σ_p, γ, α_2 and β were obtained through curve fitting of simple uniaxial compression tests. Reyes *et al.* (2003) empirically relate the densification strain ε_D to the foam relative density using the function given below:

$$\varepsilon_D = -\frac{9+\alpha^2}{3\alpha^2}\ln\left(\frac{\rho_f}{\rho_s}\right), \qquad [7\text{-}6]$$

where ρ_f and ρ_s are the foam and base material densities, respectively.

Reyes *et al.* calibrated their model against uniaxial tests carried out on aluminium foam specimens and the modelling results were seen to accurately represent all the measured stress-strain curves. One of the main advantages of the LS-DYNA version of the Deshpande and Fleck model is that a fracture criterion has been implemented within the model, which allows the removal (erosion) of elements when a critical value of volumetric strain is reached. Figure 7-4 illustrates the experimental quasistatic compressive stress-strain curves of R51 and R200 (at a nominal strain rate of 0.01 s^{-1}), and the corresponding curve fit using Equation [7-5], to obtain the material parameters σ_p, γ, α_2 and β (tabulated in Table 7-1).

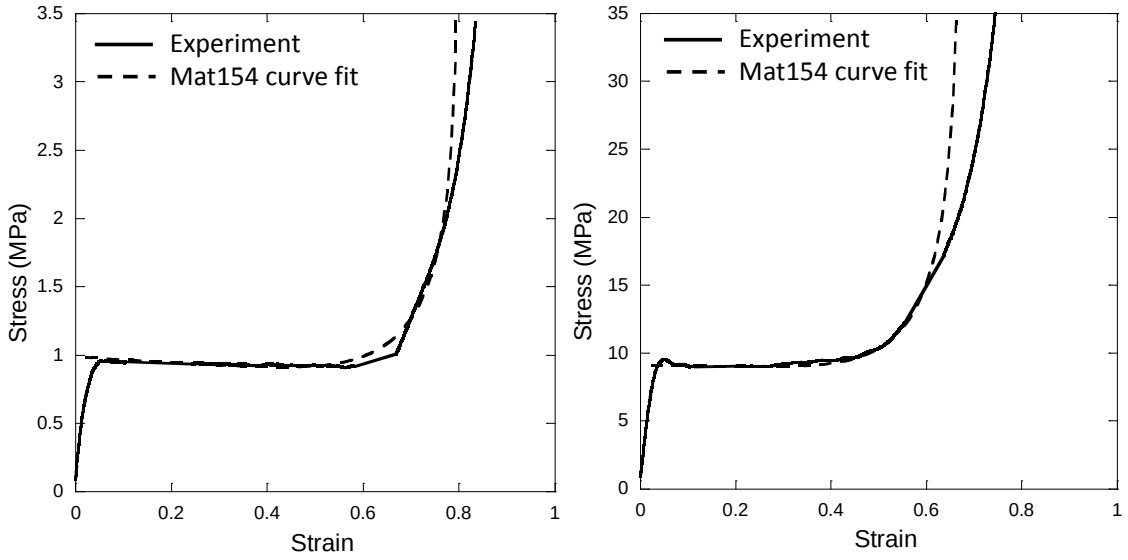


Figure 7-4: Uniaxial compression experimental results (T=23°C, $\dot{\varepsilon} = 10^{-2}\, s^{-1}$) for R51 (shown on left) and R200 (shown on right), and the corresponding curve fit using Equation [7-5].

As Rohacell foam shows negligible lateral deformation the Poisson's ratio was considered zero, hence, uniaxial strain can replace volumetric strain. The failure strain from uniaxial tensile tests was used as the critical value of volumetric strain (referred to as cfail in *MAT_154*), for removal (erosion) of elements.

Material	Density (kg m^{-3})	Young's Modulus (MPa)	α	γ	ε_D	α_2	β	σ_p	cfail
R51	51	32.5	2.12	-0.16	0.8	0.8	6.8	0.98	0.03
R200	200	246.4	2.12	-0.3	0.67	9.9	6.8	9.1	0.03

*Table 7-1: Input parameters for *MAT_154, measured from fitting equation [7-5] to the uniaxial compressive stress-strain curves of R51 and R200*

7.2.2.1 Model Parameters

A 3D model of the indentation test was created using default eight-node brick elements with a one point reduced integration scheme. The indenter was modelled as a rigid steel body, constrained to move normal to the top surface of

the foam. 57600 elements were used to model the foam, and a fine mesh was defined below the indenter region (see Figure 7-5).

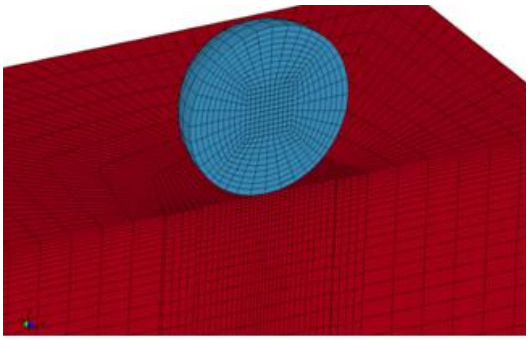


Figure 7-5: Cross-section of an indentation experiment in LS-DYNA

The **Contact_Surface_To_Surface* card was used to model the contact between the indenter and foam block, including the optional soft constraint-based formulation, which is recommended when the material constants of the surfaces in contact have large differences in elastic bulk moduli values, e.g. foam materials interacting with metals. In some occasions, when foam materials are highly compressed, the solid elements may invert, leading to negative volume and error termination. To avoid this, the **Contact_Interior* card was used, which ensured constant contact between the interior surfaces of the solid elements of the foam material. Under compressive loads, it is possible elements within the foam will interact with one another. To avoid elements penetrating each other and causing numerical instabilities, the **Contact_Automatic_Single_Surface* card was also used.

7.2.2.2 Results

Figure 7-6 shows the force-displacement results of the indentation tests run in LS-DYNA using *MAT_154* (the ABAQUS results have also been included for comparison).

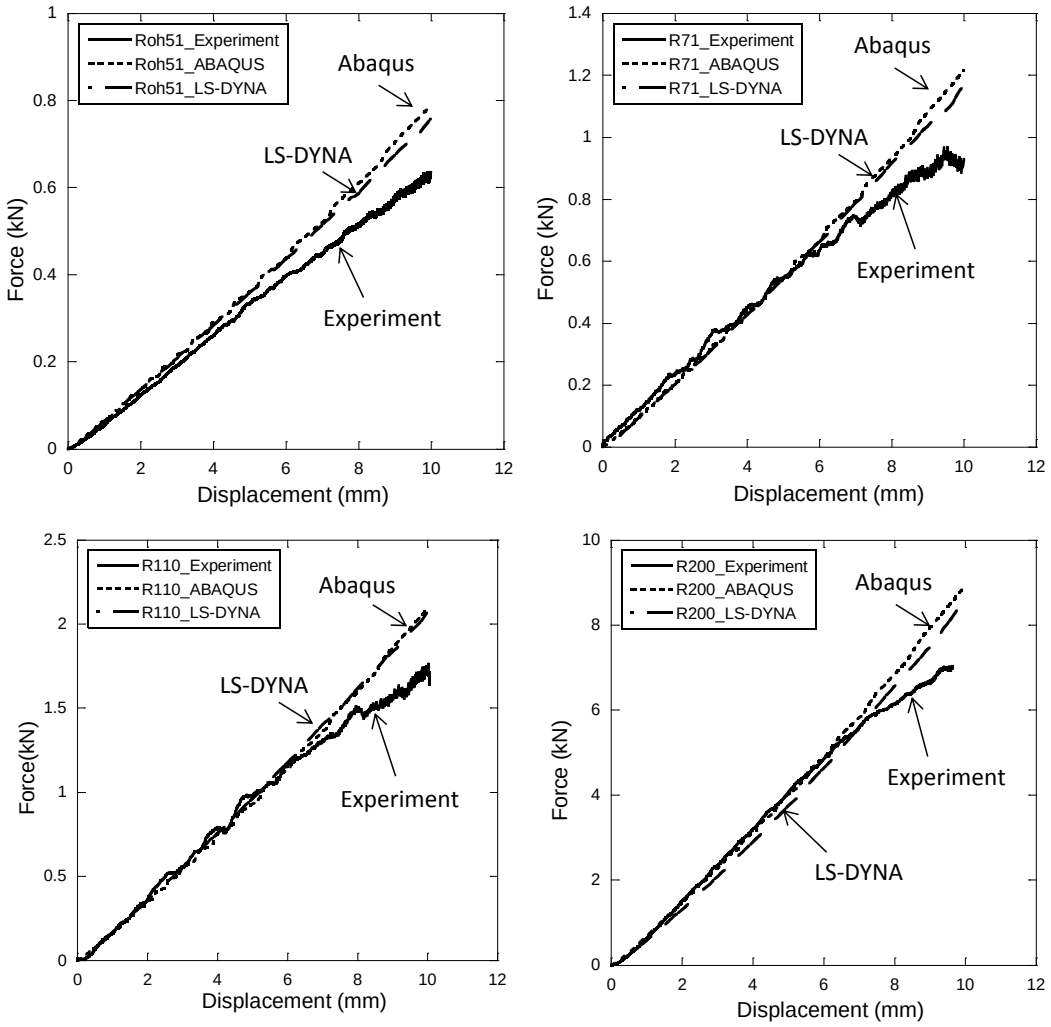


Figure 7-6 Indentation test results vs. numerical modelling (in both ABAQUS and LS-DYNA) using the Deshpande and Fleck Material model, for all four foam densities.

The results show that similar to the ABAQUS model, the LS-DYNA foam model is capable of capturing the elasto-plastic quasi-static response of Rohacell WF foams of different densities; however, once fracture starts to occur, even with the presence of a failure criteria (cfail), the resulting force

values over-estimate the experiments. This result, however, was not totally surprising as Reyes *et al.* reported that their model agreed very well with uniaxial tests conducted on Aluminium foam; however, when they used their material model to calibrate against a series of indentation experiments conducted by Hanssen *et al.* (2002), their results similar to that seen here, showed over-estimated force values compared to the experiments. They however, further optimised their FE model to also include a stress-based fracture criterion. This allowed elements to be eroded once the maximum principal stress reached a critical value. They claim this version of the model proves to give a much more realistic result, compared to the strain-based option, however, unfortunately, only the strain-based option was implemented in LS-DYNA.

7.3 Discussion

The *Deshpande and Fleck* model implemented in LS-DYNA was capable of capturing the elasto-plastic response of the foam material at different densities, however, once fracture occurred, even with the presence of a failure criterion (cfail), the resulting force values over-estimated the experiments.

The experimental results reported in this study suggest that the geometric features of the foam microstructure and their statistical distribution can substantially affect the macroscopic mechanical response. The tension/compression asymmetry of foam stiffness and yield stress are examples of the effect of foam microstructure on its macroscopic response. Such effects can be captured by existing continuum, phenomenological numerical models and associated (lengthy) multi-axial calibration experiments; however, such

models are unable to capture strain-induced anisotropy and the details of brittle foam fracture. A physically based, multi-scale modelling approach incorporating stochastic aspects of the foam microstructure, can in principle provide detailed predictions of all aspects of the mechanical response of foams; the development of this modelling approach is not pursued here.

Chapter 8

Conclusions, Improvements and Future Work

The objective of this thesis was to explore and generate a deeper understanding of the mechanical behaviours of cellular foam materials, with particular emphasis on their application in the aerospace industry. The aerospace company sponsoring this thesis (Rolls Royce Plc.) has an invested interest in the use of light-weight cellular materials for their future generation engines. It has therefore been the main objective of the author to ensure that this thesis fills some of the gaps in the current understanding of cellular materials, that it responds to the many unanswered engineering questions in the literature, and generates new data and a better understanding of the use of these materials in aerospace applications. The material of interest investigated in this study was a closed-cell Polymethacrylimide foam, also known by the trade name of Rohacell foam. However, the research focus and data generated by this work are not specific to this material, but cover a broad range of cellular

materials such as open or closed-cell, polymer or metallic, foam or honeycomb materials.

Chapter 1 provided the background and the objectives for this research. The need for a better understanding of the complex response of cellular materials was discussed and the main research objectives laid out. In Chapter 2 the strategy deployed to meet the objectives was justified through an overview of the state-of-the-art published work on the theories and ideas pertinent to the research project. Gaps in the literature were identified and discussed, and the research strategy employed for addressing these gaps highlighted. Once the foundation of the thesis was established, the remaining chapters concentrated on generating new data and scientific understanding.

Quasistatic Response at Different Length Scales

Quasistatic compression and tensile experiments conducted on four Rohacell foam densities (ranging from 50 to 200 kg m^{-3}) revealed that foams of lower relative density exhibited stronger yield strengths in tension than in compression, whereas the opposite was found for high-density foams. The material also appeared stiffer in tension than in compression, especially at lower foam densities. As a result, it was found that both the elastic and plastic macroscopic response of the foam displayed a tension/compression asymmetry. The literature showed that conjectures regarding this asymmetry did not provide supporting evidence and most of the micromechanical models found in the literature predicted equal stiffness and strength in tension and compression, based on the assumption that cell collapse is governed by plastic cell-wall bending. In this thesis, evidence was provided that in compression,

collapse is initiated by a combination of elastic buckling and plastic bending for low-density foams, while plastic cell-wall bending is responsible for the macroscopic plastic collapse of high-density foams. This evidence was gathered through a series of *in-situ* SEM experiments, which helped reveal how the different deformation mechanisms active for the low and high-density foams were the controlling factors behind the measured tension/compression asymmetry.

The experimental findings from the quasistatic macroscopic tests combined with *in-situ* observations have shown that the complexity of foam materials and the different deformation mechanisms occurring at different foam densities are such that simple scaling laws proposed by authors, such as Gibson and Ashby, are no longer valid for all foam densities. These scaling laws and other existing micromechanical models in the literature predict that the material stiffness scales with the relative density according to a single power-law. In this thesis it has been shown that the strength and stiffness parameters of Rohacell foam can be better fitted by two distinct power-law expressions, where an increase of power-law exponent with relative density, consistent with the notion of different deformation mechanisms active for the low-density and high-density foams is proposed.

Future Work

In Chapter 4 the macroscopic mechanical response of Rohacell foam in four foam densities was investigated using quasistatic compression, tension and shear experiments. Conventional experimental techniques in-line with ASTM test standards were employed. For *compression testing*, right cylindrical

specimens with specimen thickness governed by the requirements of high strain rate experiments were used. For *tensile testing,* standard dogbone specimens were used, whilst for *single-lap shear testing,* I-beam specimens were employed. The test techniques used and the choice of specimen size yielded uniaxial data which were both sensible and repeatable. For future testing, the use of a torsion rig test for measuring shear properties is recommended. The I-beam shear test method employed in this thesis was preferred to the torsion test, due to the ease of specimen preparation, simple data reduction procedures and availability of testing apparatus. However, the test method does not produce pure shear due to secondary stresses acting upon the specimen; thus, an increased specimen length to thickness ratio was used to reduce these effects. Torsion loading of a circular thin-walled foam specimen could potentially provide a more accurate measure of shear properties, where testing could also be conducted at different loading rates. However, the need for a large specimen size increases machining costs, and the level of machining required may expose the specimen geometry to a high risk of machine-induced damage and residual stresses, affecting the material response. Nonetheless, it is a consideration worth pursuing as part of a future study.

Effects of Strain Rate and Temperature

To assess the strain-rate dependency of the mechanical properties of Rohacell foam a dedicated SHPB of enhanced sensitivity was developed. Photography-based methods in conjunction with one-dimensional elastic wave theories were used to measure the history of the stress-strain field in the specimen as a function of time. Combined with quasistatic and medium rate

experiments, the sensitivity of the foams' response to an imposed strain rate over seven decades of strain (in the range 10^{-3} – $5x10^{3}$) was explored and reported for the first time in the literature.

It was found that the strain-rate dependency of the strength of the material did not continue to rise at very high rates of strain, as assumed for a number of foam materials and in a number of commonly used constitutive models. All foams exhibited mild strain rate sensitivity and a ductile response at low to medium strain rates, but showed progressive embrittlement as the rates were increased beyond 100 s^{-1}, leading to a drop in measured flow stress as the applied strain rate reached $5x10^{3}$ s^{-1}. The materials also displayed great sensitivity to the imposed temperature, demonstrating an elastic-brittle response at low temperatures (203 K) transitioning to a ductile-rubbery response at higher temperatures (473 K). The tendency towards a brittle response was found to be more pronounced for foams of higher relative density. A time-temperature superposition method was successfully used to map the strain rate sensitivity of the foams' response to the sensitivity of the response at different temperatures, thus reinforcing the idea that the sensitivity of the response of these foams to temperature and strain rate is principally governed by the inherent sensitivity of the parent polymer blend, with a minor effect of microstructural features and micro-inertia. Using the experimental data generated at different temperatures, a simple formula was employed to obtain initial estimates of the foam stiffness as a function of temperature and relative density. Such formulas can be useful for engineers and designers in their preliminary design calculations.

Future Work

It is known that the local maximum strain in the cell walls scales linearly with the microscopically applied strain rate (Gibson & Ashby 1999) by a constant of proportionality which depends on the geometrical details of the microstructure (assuming microscopic collapse by plastic cell wall bending). It is therefore possible that the relatively long and slender cell walls of foams of low density result in lower local strain rates than those applied to the stockier cell walls of R200, for a given imposed macroscopic strain rate. However, a detailed analysis of the relative influence of these mechanisms upon the macroscopic foam response has not been conducted in this study and it is recommended this work is investigated further as part of a future study.

An open pending question that has not been answered at this point is how the gas trapped in the closed-cell foams affects the onset of failure or the state of stress at a microscopic level. During the foaming process the blowing agent (alcohol) is evaporated at high temperatures, leaving air enclosed within the closed cells. As the lowest value of modulus tested in this study is 32 MPa (for R51) and the atmospheric air pressure is 0.1MPa, the internal air pressure contribution to the stiffness of the foam can be deemed negligible. Nonetheless, it would be interesting to conduct further experiments to quantify the effect of enclosed air pressure on the overall foam response. On a similar note, Rohacell is hygroscopic, i.e. it absorbs moisture and can expand with increasing relative humidity. It is recommended that if further experiments are performed on this material, prior to each test, the material is dried out in an oven, and the effect of moisture absorption on the material response is quantified.

Strain-Induced Anisotropic Properties

One of the many unanswered questions with which aerospace engineers are confronted, is how to account for and quantify the material property changes which occur in cellular materials due to applied strain. This question has been answered in Chapter 6, where uniaxial compression and tensile tests were performed on pre-crushed low and high density Rohacell foams. It was found that upon application of strain, Rohacell foams exhibit strain-induced anisotropic properties, where pre-crushing has a detrimental effect on the residual specific strength and stiffness of the material in different loading directions, with specific residual properties dropping significantly, relative to the un-crushed virgin material. The pre-crushed material also exhibited a tension/compression asymmetry of the residual strength, similar to that measured for the virgin material reported in Chapter 4.

In the literature it is often found that the tension/compression asymmetry of the moduli and strength and the strain-induced anisotropic properties of foams are generally neglected. In this thesis, a series of three-point-bend experiments were performed on the virgin and pre-crushed foam, and by using simple beam formulas it was found how neglecting these effects can lead to incorrect predictions of the foams' structural response.

Future Work

The experimental investigation reported in Chapter 6 was limited to foams R51 and R200. If time had permitted, more experiments would have been conducted on the intermediate foam densities to produce a more complete database. In addition, all the pre-crushed and three-point-bend tests were

performed under quasistatic loading rates. To investigate the effect of repeat impact loading on the material (for example when a fan blade or a composite fan track liner is subject to repeat ice impact shots), it would have been more appropriate and complete if strain rate effects of the pre-crushed material had also been investigated. Unfortunately, the project time did not allow for this and these activities have been left as a topic for a future study.

Macroscopic Modelling

Current Finite Element material models do not account for the tension/compression asymmetry of the strength and stiffness of the foam, or the strain-induced anisotropic material properties observed in this study. As foam materials are generally used to their best potential under compressive loading, compressive properties are typically reported. Numerical models generally require a single moduli and strength parameter to predict foam behaviour, where the user is expected to input compressive values, assume these values remain unchanged, and use similar values in tension. However, in this thesis it was shown that neglecting the tension/compression asymmetry or strain-induced anisotropic properties can lead to incorrect predictions of the foams' structural response. This finding identifies a significant shortcoming of existing FE models for predicting the foam response under complex loading.

Future Work

A review of existing FE foam material models and the use of simple indentation tests to validate their use, demonstrated that in most cases the model was capable of capturing the elasto-plastic response, but fracture could not be predicted easily. It was found that within the Finite Element discretisation

framework, FE methods cannot cope with highly compressible materials such as Rohacell foams. The non-uniform and at times unstable element deformation can lead to the removal of elements well before the material is considered to have failed, leading to numerical results under-predicting experiments significantly. It is recommended that for future studies meshless methods are investigated for predicting the failure response of the material.

The experimental results reported in this thesis suggest that the geometric features of the foam microstructure, their statistical distribution, the tension/compression asymmetry of foam stiffness and yield stress, strain rate and temperature effects and strain-induced changes in material properties, can substantially affect the macroscopic mechanical response of the material. It is recommended that as part of a future study the comprehensive experimental data-set and new findings from this thesis are taken, and a physically based, multi-scale modelling approach incorporating stochastic aspects of the foam microstructure is used to provide detailed predictions of all aspects of the mechanical response of foam materials.

Summary

The knowledge gained from this thesis presents researchers and engineers with a comprehensive experimental data-base on Rohacell foams of different foam densities, which have not appeared in the literature thus far. More appropriate predictive tools for measuring the foams' response at low and high-foam densities are presented. The temperature and strain rate dependency of the mechanical properties of Rohacell foams have been measured, and a quantitative approach towards predicting the materials' response using only one method of measurement has been identified and presented. It is shown that strain-induced anisotropic properties and compression/tension asymmetry cannot be overlooked, as it has been demonstrated and quantified that by neglecting these effects, the structural capability of the material can be over or under-estimated.

The new data and understanding generated by this thesis will allow engineers and researchers, who are developing constitutive models for predicting the response of foam materials, to account for more aspects of the mechanical behaviours in their FE models.

Resulting publications accepted so far are listed below.

Publication	Work included
Arezoo, S. et al., 2013. Compressive deformation of Rohacell foams: Effects of strain rate and temperature. *International Journal of Impact Engineering*, 51, pp.50–57.	Chapter 4
Arezoo, S. et al., 2011. The mechanical response of Rohacell foams at different length scales. *Journal of Materials Science*, 46(21), pp.6863–6870. 7	Chapter 5

References

Al-Maliky N and Fernandez J (1998) Drops in the flow stress of semi-crystalline polymers at very high rates of strain. *Journal of materials science letters*. 17, 1141–1143.

Andrews E (2001) Size effects in ductile cellular solids. Part II: experimental results. *International Journal of Mechanical Sciences*. 43 (3), 701–713.

Arezoo S, Tagarielli VL, Petrinic N. and Reed JM (2011) The mechanical response of Rohacell foams at different length scales. *Journal of Materials Science*. 46 (21), 6863–6870.

Arezoo S, Tagarielli VL, Siviour C.R. and Petrinic N. (2013) Compressive deformation of Rohacell foams: Effects of strain rate and temperature. *International Journal of Impact Engineering*. 51, 50–57.

Arruda EM, Boyce MC and Jayachandran R (1995) Effects of strain rate, temperature and thermomechanical coupling on the finite strain deformation of glassy polymers. *Mechanics of Materials*. 19 (2-3), 193–212.

Ashby M, Evans T, Fleck N.A., Hutchinson JW, Wadley HNG and Gibson LJ (2000) *Metal Foams (A Design Guide)*. Butterworth Heinemann

Bacon C (1999) Separation of waves propagating in an elastic or viscoelastic Hopkinson pressure bar with three-dimensional effects. *International Journal of Impact Engineering*. 22 (1), 55–69.

Balzer, J. E., Siviour, C. R., Walley, S. M., Proud, W. G., & Field, J. E. (2004). Behaviour of ammonium perchlorate-based propellants and a polymer-bonded explosive under impact loading. *Proceedings of the Royal Society A: Mathematical, Physical and Engineering Sciences*, *460*(2043), 781–806

Brydson JA (1999) *Plastics Materials* (7th edition). Oxford: Butterworth Heinemann

Chamis CC (1974) Analysis of the three-point-bend test for materials with unequal tension and compression properties. *Report No. NASA TN D-7572*, 33.

Chang F, Song Y, Lu D and DeSilva CN (1998) Unified constitutive equations of foam materials. *Journal of Engineering Materials and Technology*. 120, 212–217.

Chen CP and Lakes RS (1995) Analysis of the structure - property relations of foam materials. *Cellular polymers*. 14 (3), 186–202.

Chen W., Lu F, Frew D. J. and Forrestal MJ (2002) Dynamic Compression Testing of Soft Materials. *Journal of Applied Mechanics*. 69 (3), 214.

Chen W., Zhang B and Forrestal MJ (1999) A split Hopkinson bar technique for low-impedance materials. *Experimental Mechanics*. 39 (2), 81–85.

clarasonic.com (2010) *Clarasonic - Distributor of Rohacell*. [Online] Available at: http://clarasonic.com (accessed 06/10/10).

Deshpande V and Fleck N (2000) High strain rate compressive behaviour of aluminium alloy foams. *International Journal of Impact Engineering*. 24 (3), 277–298.

Deshpande VS and Fleck N A (2000) Isotropic constitutive models for metallic foams. *Journal of the Mechanics and Physics of Solids*. 48, 1253–1283.

Deshpande VS and Fleck N A (2001) Multi-axial yield behaviour of polymer foams. *Acta Materialia*. 49 (10), 1859–1866.

Dioh N, Leevers P and Williams J (1993) Thickness effects in split Hopkinson pressure bar tests. *Polymer*. 34 (20), 4230–4234.

Donald AM (2003) The use of environmental scanning electron microscopy for imaging wet and insulating materials. *Nature Materials*. 2 (8), 511–516.

Dragnevski KI (2012) A brief overview of In-situ Mechanical Testing in the Environmental Scanning Electron Microscope. *Micro and Nanosystems*. 4 (2), 92–96.

Drodge DR (2009) *"Mechanical properties of energetic composites"*. PhD thesis, Cambridge University.

Eaves D (2004) *Handbook of Polymer Foams* (1st edition). D. Eaves ed. Shropshire: Rapra Technology Limited

ERG Aerospace Corp. (2009) *Foam Properties*. [Online] Available at: http://www.ergaerospace.com (accessed 05/04/09).

Evonik Industries AG (2011) *Rohacell WF Foam*. [Online] Available at: www.roehm.com (accessed 05/02/11).

Fleck N A., Stronge WJ and Liu JH (1990) High Strain-Rate Shear Response of Polycarbonate and Polymethyl Methacrylate. *Proceedings of the Royal Society A: Mathematical, Physical and Engineering Sciences*. 429 (1877), 459–479.

Gent AN and Thomas AG (1959) The deformation of foamed elastic materials. *Journal of Applied Polymer Science*. 1 (1), 107–113.

Gibson LJ and Ashby MF (1999) *Cellular Solids Structures and properties - Second edition* (2nd edition). D. R. Clarke, S. Suresh, & I. M. Ward eds. Cambridge: Cambridge University Press

Gray III GT (1999) Classic Split-Hopkinson Pressure Bar Technique. In: H. Kuhn & D. Medlin eds. *ASM V8 Mechanical Testing*. Ohio: ASM International. 17–20.

Gundberg T (2012) *Typical sandwich construction*. [Online] Available at: http://boatdesign.net/articles/foam-core/ (accessed 08/05/12).

Hanssen AG, Hopperstad O.S, Langseth M and Ilstad H (2002) Validation of constitutive models applicable to aluminium foams. *International Journal of Mechanical Sciences*. 44 (2), 359–406.

Harrigan JJ and Reid SR (1999) Inertia effects in impact energy absorbing materials and structures. *International Journal of Impact*. 22, 955–979.

Holt JM (1999) Introduction to Mechanical Testing and Evaluation. In: H. Kuhn & D. Medlin eds. *ASM Handbook: Volume 8: Mechanical Testing and Evaluation*. Ohio: ASM International. 125–142.

Jumpasut A, Petrinic Nik, Elliott BCF, Siviour Clive R. and Arthington MR (2008) An Error Analysis into the Use of Regular Targets and Target Detection in Image Analysis for Impact Engineering. *Applied Mechanics and Materials*. 13-14, 203–210.

Ko WL (1965) Deformations of Foamed Elastomers. *Journal of Cellular Plastics*. 1 (1), 45–50.

Koissin V (2006) Deformation of Foam Cores in Uniaxial Compression-Tension Cycle. *Journal of Sandwich Structures and Materials*. 8 (5), 395–406.

Koissin V and Shipsha A (2009) Residual In-plane Mechanical Properties of Transversely Crushed Structural Foams. *Journal of Sandwich Structures and Materials*. 11 (2-3), 199–211.

Kolsky H (1949) An Investigation of the Mechanical Properties of Materials at very High Rates of Loading. *Proceedings of the Physical Society. Section B*. 62 (11), 676–700.

Kuhn H. (2000) *ASM Handbook: Volume 8: Mechanical Testing and Evaluation*. Howard Kuhn & Dana Medlin eds. Ohio: ASM International

Lederman J (1971) The prediction of the tensile properties of flexible foams. *Journal of Applied Polymer Science*. 15, 693–703.

Li P, Petrinic N., Siviour C.R., Froud R and Reed JM (2009) Strain rate dependent compressive properties of glass microballoon epoxy syntactic foams. *Materials Science and Engineering: A*. 515 (1-2), 19–25.

Li Q, Mines RAW and Birch RS (2000) The crush behaviour of Rohacell-51WF structural foam. *International Journal of Solids and Structures*. 37 (43), 6321–6341.

Livermore Software Technology Corporation (2006) *LS-DYNA Theory manual*. J. O. Hallquist ed. California

McCrum NG, Buckley CP and Bucknall CB (1997) *Principles of Polymer Engineering* (2nd edition). Oxford: Oxford Science Publications

Meyers MA and Chawla KK (2009) *Mechanical Behavior of Materials* (2nd edition). Cambridge University Press

Mills N (2007) *Polymer Foams Handbook "Engineering and Biomechanics applications and Design Guide"* (1st edition). Oxford: Butterworth Heinemann

Mines RAW (2007) Strain Rate Effects in Crushable Structural Foams. *Applied Mechanics and Materials*. 7-8, 231–236.

Mulliken A and Boyce M (2006) Mechanics of the rate-dependent elastic–plastic deformation of glassy polymers from low to high strain rates. *International Journal of Solids and Structures*. 43 (5), 1331–1356.

Nathan S (2008) Clean Machines. *Magazine Article: The Engineer*, 22–25.

Rajaneesh A, Sridhar I and Rajendran S (2011) Numerical modeling of low velocity impact response on metal foam cored sandwich panels: Effect of various facesheet materials. In: *18th International Conference on Composite Materials*. South Korea. 6.

Reid SR and Peng C (1997) Dynamic uniaxial crushing of wood. *International Journal of Impact Engineering*. 19 (5-6), 531–570.

Reyes A, Hopperstad O.S., Berstad T, Hanssen AG and Langseth M (2003) Constitutive modeling of aluminum foam including fracture and statistical variation of density. *European Journal of Mechanics - A/Solids*. 22 (6), 815–835.

Richeton J, Ahzi S, Vecchio K, Jiang F and Adharapurapu R (2006) Influence of temperature and strain rate on the mechanical behavior of three amorphous polymers: Characterization and modeling of the compressive yield stress. *International Journal of Solids and Structures*. 43 (7-8), 2318–2335.

Robinson T (2012) *Blades of Glory*. [Online] Available at: http://media.aerosociety.com/aerospace-insight/2012/02/03/blades-of-glory/6204/ (accessed 05/06/12).

Saha MC, Mahfuz H., Chakravarty UK, Uddin M, Kabir ME and Jeelani S. (2005) Effect of density, microstructure, and strain rate on compression behavior of polymeric foams. *Materials Science and Engineering: A*. 406 (1-2), 328–336.

Shergold O, Fleck N and Radford D (2006) The uniaxial stress versus strain response of pig skin and silicone rubber at low and high strain rates. *International Journal of Impact Engineering*. 32 (9), 1384–1402.

Shipsha A, Hallström S and Zenkert D (2003) Failure Mechanisms and Modelling of Impact Damage in Sandwich Beams - A 2D Approach: Part II - Analysis and Modelling. *Journal of Sandwich Structures and Materials*. 5 (33), 20.

Siebert H (2010) *Applications for PMI foams in aerospace sandwich structures*. [Online] Available at: www.reinforcedplastics.com (accessed 07/08/10).

Siviour C R (2005) *High Strain Rate Properties of Materials using Hopkinson Bar Techniques*. PhD thesis, Cambridge University.

Siviour C R and Grantham SG (2009) High resolution optical measurements of specimen deformation in the split Hopkinson pressure bar. *Imaging Science Journal*. 57 (6), 333–343.

Siviour C R, Grantham SG, Williamson DM, Proud W G and Field J E (2009) Novel measurements of material properties at high rates of strain using speckle metrology. *Imaging Science Journal*. 57 (6), 326–332.

Siviour C R, Proud W G, Salisbury DA and Winter RE (2008) High strain rate compressive behaviour of a Silicone Elastomer. In: *Proceedings of the XIth International Congress and Exposition*. Orlando. 2–8.

Siviour C.R., Walley SM, Proud W.G. and Field J.E. (2005) The high strain rate compressive behaviour of polycarbonate and polyvinylidene difluoride. *Polymer*. 46 (26), 12546–12555.

Song B. (2005) Strain-rate effects on elastic and early cell-collapse responses of a polystyrene foam. *International Journal of Impact Engineering*. 31 (5), 509–521.

Song B., Chen W. and Lu W.-Y. (2007) Compressive mechanical response of a low-density epoxy foam at various strain rates. *Journal of Materials Science*. 42 (17), 7502–7507.

Song Bo, Chen Weinong and Frew Danny J. (2004) Dynamic Compressive Response and Failure Behavior of an Epoxy Syntactic Foam. *Journal of Composite Materials*. 38 (11), 915–936.

Song Bo, Lu Wei-Yang, Syn CJ and Chen Weinong (2008) The effects of strain rate, density, and temperature on the mechanical properties of polymethylene diisocyanate (PMDI)-based rigid polyurethane foams during compression. *Journal of Materials Science*. 44 (2), 351–357.

Soni SM, Gibson RF and Ayorinde EO (2009) The influence of subzero temperatures on fatigue behavior of composite sandwich structures. *Composites Science and Technology*. 69 (6), 829–838.

Stewart R (2010) *Sandwich structures deliver core benefits*. [Online] Available at: http://www.reinforcedplastics.com/view/10178/sandwich-structures-deliver-core-benefits/ (accessed 22/06/11).

Subhash G, Liu Q and Gao X (2006) Quasistatic and high strain rate uniaxial compressive response of polymeric structural foams. *International Journal of Impact Engineering*. 32 (7), 1113–1126.

Szyniszewski S, Smith B, Arwade S, Hajjar J and Benjamin S (2012) Tensile and shear element erosion in metal foams. In: *12th International LS-DYNA Users Conference*. Michigan. 1–10.

Tagarielli V, Deshpande V and Fleck N (2008) The high strain rate response of PVC foams and end-grain balsa wood. *Composites Part B: Engineering*. 39 (1), 83–91.

Tan P, Reid S, Harrigan J, Zou Z and Li S (2005) Dynamic compressive strength properties of aluminium foams. Part I—experimental data and observations. *Journal of the Mechanics and Physics of Solids*. 53 (10), 2174–2205.

Thomas T, Mahfuz Hassan, Carlsson L a, Kanny K and Jeelani Shaik (2002) Dynamic compression of cellular cores: temperature and strain rate effects. *Composite Structures*. 58 (4), 505–512.

Thomas T, Mahfuz Hassan, Kanny K and Jeelani Shaik (2004) High Strain Rate Response of Cross-Linked and Linear PVC Cores. *Journal of Reinforced Plastics and Composites*. 23 (7), 739–749.

Toffsworld.com (2012) *A typical Turboprop engine*. [Online] Available at: http://toffsworld.com/outdoor-activities/airplanes-aircraft/turboprop-engines-used-in-commercial-aircraft/ (accessed 06/02/12).

Trautmann A, Siviour C. R., Walley SM and Field J. E. (2005) Lubrication of polycarbonate at cryogenic temperatures in the split Hopkinson pressure bar. *International Journal of Impact Engineering*. 31 (5), 523–544.

Walley SM and Field J. E. (1994) strain rate sensitivity of polymers in compression from low to high rates. *DYMAT*. 1 (3), 211–227.

Wang Z, Ma H, Zhao L and Yang G (2006) Studies on the dynamic compressive properties of open-cell aluminum alloy foams. *Scripta Materialia*. 54 (1), 83–87.

Ward IM and Sweeney J (2005) *An Introduction to the Mechanical Properties of Solid Polymers* (2nd edition). Wiley

Williams ML, Landel RF and Ferry JD (1955) The Temperature Dependence of Relaxation Mechanisms in Amorphous Polymers and Other Glass-forming Liquids. *Journal of American Chemical Society*. 77 (14), 3701–3707.

Williamson DM, Siviour C R, Proud W G, Palmer SJP, Govier R, Ellis K, Blackwell P and Leppard C (2008) Temperature–time response of a polymer bonded explosive in compression (EDC37). *Journal of Physics D: Applied Physics*. 41 (8), 085404.

www.aerospaceweb.org (2012) *GE and NASA's Unducted Fan design in the late 1980's*. [Online] Available at: http://www.aerospaceweb.org/question/propulsion/q0067.shtml (accessed 02/11/12).

www.gkn.com (2012) *Composite fan case system*. [Online] Available at: http://www.gkn.com/aerospace/products-and-capabilities/engine-casing-

and-fixed-structure/composite-fan-case/Pages/default.aspx (accessed 08/10/12).

Zenkert D and Burman M (2009) Tension, compression and shear fatigue of a closed cell polymer foam. *Composites Science and Technology*. 69 (6), 785–792.

Zhao H and Gary G (1996) On the use of SHPB techniques to determine the dynamic behavior of materials in the range of small strains. *International Journal of Solids and Structures*. 33 (23), 3363–3375.